ULTRAFAST CARRIER AND LATTICE DYNAMICS STUDIES IN GaAs WITH INTENSE OPTICAL EXCITATION

by

Amlan Kumar Basak

B.Sc. (Hons.), Physics, University of North Bengal, 1999

M.Sc., Physics, Indian Institute of Technology, Bombay, 2002

M.S., Physics, University of Pittsburgh, 2004

Submitted to the Graduate Faculty of

the School of Arts and Sciences in partial fulfillment

of the requirements for the degree of

Doctor of Philosophy

University of Pittsburgh

2010

UNIVERSITY OF PITTSBURGH

SCHOOL OF ARTS AND SCIENCES

This dissertation was presented

by

Amlan Kumar Basak

It was defended on

July 22, 2010

and approved by

Hrvoje Petek, Professor, Department of Physics and Astronomy

David W. Snoke, Professor, Department of Physics and Astronomy

Robert P. Devaty, Associate Professor, Department of Physics and Astronomy

W. Vincent Liu, Associate Professor, Department of Physics and Astronomy

Kevin P. Chen, Associate Professor, Department of Electrical and Computer Engineering

Dissertation Director: Hrvoje Petek, Professor, Department of Physics and Astronomy

ULTRAFAST CARRIER AND LATTICE DYNAMICS STUDIES IN GaAs WITH INTENSE OPTICAL EXCITATION

Amlan Kumar Basak, PhD

University of Pittsburgh, 2010

Detailed understanding of basic scattering mechanisms of high density and highly energetic carriers (electrons and holes) are important for future semiconductor device technology. During these scattering processes carriers interact among themselves and with the lattice. Most of the scattering events occur in few tens of femtoseconds to picosecond timescale. Ultrafast lasers, with improving performance, make it possible to observe these fundamental interactions as they happen and detailed study on them becomes possible.

Here we present ultrafast carrier and lattice dynamics studies in the technologically important III-V semiconductor GaAs. We performed ultrafast pump-probe spectroscopy in transient reflection and reflective electro optic sampling geometries on n-doped GaAs with 10^{18}-10^{20} cm^{-3} photoexcited electron-hole pair density. Coherent phonons and plasmons are generated in the semiconductor as a result of interaction between the photocarriers and the lattice; they modulate the dielectric properties of the sample, which can be detected by measuring transient reflectivity. By varying the excitation laser fluence, we varied the excited carrier density and measured the response of the semiconductor at different photoexcited carrier density levels. Detailed analysis of density dependent response sheds light on generation mechanism of coherent phonons and plasmons and subsequent dynamics and transport. Further analysis using a dielectric response model shows that the carrier density dependent coupled plasmon-phonon dynamics represents the hole plasma response.

We also performed symmetry selective generation and detection of coherent phonons and plasmons by exciting and probing the crystal along different crystallographic directions. These results tell us about the dominating processes responsible for the generation and detection of these modes. We further analyzed the changes in the frequency response with time and probed the plasmon-phonon response at various photon energies of the exciting and probing pulse. Time dependent frequency of the coupled plasmon-phonon mode indicates transient changes in the plasma density, most likely involving transport of the interacting carriers from the observed region on the sample.

TABLE OF CONTENTS

LIST OF TABLES

LIST OF FIGURES

LIST OF ABBREVIATIONS

BBO	β-Barium Borate (β-BaB_2O_4)
DECP	Displacive Excitation of Coherent Phonon
DFWM	Degenerate Four Wave Mixing
DP	Deformation Potential
EO	Electro Optic
F	Fröhlich
FK	Franz-Keldysh
fs	Femto-second (10^{-15} s)
FT	Fourier Transform
FWM	Four Wave Mixing
ISRS	Impulsive Stimulated Raman Scattering
LA	Longitudinal Acoustic
LO	Longitudinal Optical
NL	Non Linear
PBS	Polarizing Beam Splitter
PD	Photo Detector
PL	Photo Luminescence
ps	Pico-second (10^{-12} s)

REOS	Reflective Electro Optic Sampling
SHG	Second Harmonic Generation
SSHG	Surface Second Harmonic Generation
THz	Terahertz
TA	Transverse Acoustic
TO	Transverse Optical

“To my parents and my teachers”

PREFACE

I would not be writing this without the contribution of many people. First, I would like to thank my advisor Prof. Petek for his patience, guidance, support and encouragement during the course of this study. I learned a lot from him. His door was always open for a detailed discussion, to clear a doubt or to solve an experimental issue. I would also like to thank the professors who were in my thesis committee for their encouragement, support, suggestions and interest about this work. Thanks Prof. Snoke for teaching us formal and informal classes on condensed matter physics over the years. I would like to thank our collaborators; Dr. Kunie Ishioka, NIMS, Tsukuba, Japan and Prof. Christopher Stanton, University of Florida in helping us understand many aspects of this work with theoretical and experimental support.

I would also like to thank all the past and present members of the lab. From the early days in the lab till the very end, I learned a lot from all of you. I will take this opportunity to thank all the friends in the department over the years. From the days of coursework and qualifier exams till when I was writing the thesis, the help and support of friends in the department is gratefully acknowledged.

I would like to thank all the friends here in Pittsburgh and other parts of the world. Many thanks to Barun for making my initial days here comfortable by helping me adjust to a new country. Just thanks are not enough for Reeta and Amit. Pittsburgh would not have been same without you. I would like to thank friends at other parts of the US. Without your welcoming

attitude it would have been difficult for me during the early years here in US. Thank you, Satrajit, Ipsita Di, Sumi Di, Buri Di, Arup Kaku and Antara.

Special thanks to my family, my parents Ratna and Gobinda Basak and sister Soma. I would not have done it without your encouragement. Thank you Baba, Ma for not complaining even once during this five year long absence from home. Finally, I would like to thank my wife Sudeshna. You were always there for me through the high and low points of this journey. I will definitely not be here without your support, encouragement and sacrifice.

1.0 INTRODUCTION

Ultrafast optical spectroscopy is a powerful experimental technique in the study of fundamental electronic and optical properties of semiconductors. Semiconductors are the most important materials for electronic, photonic and opto-electronic devices. To understand the functionality of the semiconductor devices and for innovation of new devices, detailed understanding of physical processes in semiconductors is essential. Nowadays, with ever smaller device sizes quantum effects comes into picture and the time scale of these physical processes also becomes important [1]. Today's electronic device sizes are often <100 nanometers. The limiting time scale in which such a device operates can be approximated as the transit time of a charge carrier through it. Assuming high drift velocity, charge transport times are as small as picosecond (10^{-12} second) or sub picosecond time scales which translate to THz frequency. To understand the operational details of such a fast device we need to consider scattering events in femtosecond (10^{-15} second) timescales. Ultrafast spectroscopic techniques are the most direct tools, which can help us understand the operation of such a device. There is also a need to explore new semiconducting materials and novel structures of semiconductors to push the limits of technology and overcome the limitations in current semiconductor technology. One example is the use of novel semiconductor nanostructures to increase the efficiency of photovoltaic materials [2-4]. The understanding of the fundamental semiconductor properties as well as carrier generation,

relaxation and transport properties in these nano-structured materials are vital for future technologies.

Electrons and holes are generated in a semiconductor when excited by light with photons of energy equal to or larger than the band gap. Photoexcited carriers can be excited with excess energy with respect to the band minimum. Energetic carriers relax towards the band minimum by interacting with the lattice and generating lattice vibrations. In the band structure picture this interaction is represented as a process of phonon emission. The doped or excited carriers also have a characteristic plasma frequency, which depends on the carrier density, carrier mass, and the dielectric constant of the semiconductor. The coherent lattice vibration generated due to the carrier-lattice interaction is the coherent phonon and the coherent charge carrier oscillation is the coherent plasma oscillation. Carrier density dependent plasma frequency is very important for device operation as it can affect the carrier mobility for high density plasma. With higher carrier density the plasma frequency becomes higher. When comparable to or greater than the phonon frequency, the plasma interacts with the lattice via coulomb interaction and coupled plasmon-phonon modes are generated. The ultrafast decay of coupled plasmon-phonon mode affects the carrier transport property and the carrier mobility in the semiconductor [5].

1.1 OPTICAL SPECTROSCOPY OF SEMICONDUCTORS

Optical spectroscopy is the best way to determine the distribution functions of photo generated excitations in semiconductors and therefore to determine the dynamics and relaxation properties of the excitations. The relaxation of the photoexcited carriers (electrons and holes) happens through a series of scattering processes in which carriers interact among themselves and with the

lattice. These interaction processes occur on the sub-ps time scale, often in few 10's to 100's of fs. Ultrafast optical spectroscopy is particularly sensitive to these scattering processes when the light pulse duration used in exciting and probing the system is shorter than the time scale of these scattering processes. With sufficient time resolution it is possible to identify the carrier-carrier, carrier-lattice interactions [6], trace carrier transport [7] and observe quasiparticle generation [8]. It also helps us investigate nonlinear and highly nonequilibrium phenomena in semiconductors shedding light on many-body effects [9-11], coherent phenomena [12] and dephasing properties [13]. Using ultrashort sub ps laser pulses one can generate conditions that are unique. A very high carrier density can be generated on a time scale that is shorter than most scattering processes, producing instantaneously non-equilibrium carrier distributions.

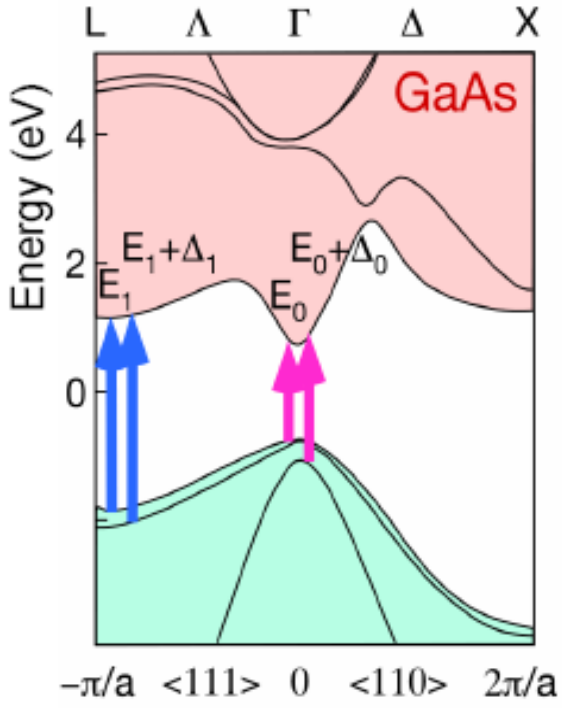

Figure 1.1 GaAs band structure; blue arrows indicate two resonant optical transitions near the L valley and pink arrows represent two resonant optical transitions at the fundamental band gap near Γ valley.

There has been much research activity on semiconductor spectroscopy in last half century. Since the invention of laser [14-16] and novel laser sources like pulsed lasers [17-21], one could explore the time domain phenomena in semiconductors. GaAs is a popular direct band gap semiconductor with important applications in photonic, photovoltaic and optoelectronic devices. The fundamental band gap of GaAs is at the center of its Brillouin zone with room temperature band gap energy of 1.43 eV [22] (Figure 1.1). There are low-energy side valleys, which form subsidiary local minima in the conduction band along the ΓL (L valley) and ΓX lines (X valley) of the reduced Brillouin zone. There is a critical point which arises due to singularity in the joint density of states along the ΓL [111] direction. Due to spin-orbit coupling it splits into two critical points and labeled as E_1 and $E_1+\Delta_1$ critical points and corresponds to 2.97 eV and 3.17 eV at room temperature [23]. Electron-hole pairs can be excited in the L-valley in a range of momenta near these critical points with appropriately chosen photon energy for the light in use.

So far, most of the research in optical spectroscopy of GaAs has been performed using photoexcitation near its fundamental band gap. Different experimental techniques like Raman Spectroscopy [24], Four Wave Mixing (FWM) spectroscopy [25], photoluminescence studies [26], etc. have been employed. Researchers have also performed surface second harmonic (SSHG) studies [27] and more recently terahertz (THz) spectroscopy [28]. Usually these different techniques give complementary information and studying the same sample using different experimental techniques can yield a near complete picture of carrier-lattice dynamics and transport. For example time-resolved photoluminescence studies provide a very good idea about the energy distribution of the carriers. FWM spectroscopy is particularly useful for studying electronic coherent phenomena and the loss of quantum coherence. By contrast, THz

spectroscopy provides information about ultrafast carrier transport. It can also yield information on phonon and plasma dynamics.

In this dissertation we discuss experimental studies on ultrafast carrier and phonon dynamics of the semiconductor GaAs. We generate carriers (electrons and holes) by photo excitation predominantly in the L-valley. The excited carriers interact with the lattice in part by coherent phonon generation and modify the dielectric properties of the material. We observe changes in optical properties created by electronic excitation by measuring the transient changes in reflectivity. The plasma oscillation also contributes to the changes in the dielectric properties. We observe changes in the time dependent reflectivity at various carrier densities that are defined by the intensity of the excitation light. We also perform pump and probe polarization dependent experiments to study symmetry properties of generation and detection processes of coherent phonon and plasma oscillation.

The unique characteristic of this work is the excitation of GaAs at 400 nm with a 10 fs laser pulse. 400 nm light excites carriers in the L-valley of GaAs at densities that are difficult to achieve with the excitation of the gamma valley at the fundamental band gap. The high carrier density and L-valley excitation create a highly nonequilibrium condition that enables us to explore the multivalley carrier evolution with a different starting point than the usual near gamma valley excitation in GaAs [29]. As mentioned earlier, carrier-carrier and carrier-lattice scattering processes as well as some of the intervalley carrier scattering processes occur in a very short (10-100 fs) timescale. To time resolve the effects of these scattering events a very short laser pulse is needed. Our near 10 fs laser pulse allows us to achieve this. High time resolution and ultrafast spectroscopy in a new regime of carrier excitation, both in terms of excitation

wavelength and excited carrier density, is the unique feature of the experiments described in this dissertation.

1.2 OUTLINE OF THE DISSERTATION

Our experimental study on semiconductor GaAs using ultrafast optical techniques is described in the following chapters. The chapters are organized as follows. Chapter 2 gives necessary theoretical background on coherent phonon and coherent plasmon generation and detection mechanisms in GaAs. It also describes the experimental set up in use. Chapter 3 discusses experimental results on the carrier density dependent measurements. We discuss plasmon-phonon coupling and corresponding theoretical model and compare the experimental results with the calculated results. In Chapter 4 we present results of pump and probe polarization dependent experiments. We discuss these results using symmetry properties of generation and detection of plasmon and phonon. Chapter 5 concerns time dependent response of GaAs after photoexcitation. We look into time dependent frequency change and the response in the time-frequency domain. We also present results on photon energy dependent measurements. Chapter 6, the final chapter, is devoted to overall discussion of the results and conclusions.

2.0 ULTRAFAST OPTICAL PROCESSES IN SEMICONDUCTORS

2.1 INTRODUCTION

Energetic photocarriers in a semiconductor relax through a hierarchy of scattering processes. During the relaxation, excited carriers interact with each other and with the lattice. In this chapter we will discuss the physical processes that are responsible for energy relaxation of carriers in GaAs. We will also discuss some experimental techniques in ultrafast optical spectroscopy. Then we will focus on generation and detection mechanisms of coherent phonons and plasmons in semiconductors and particularly in the case of GaAs. In the last section we will discuss the details of the experimental set up used to obtain the experimental results described in this thesis.

2.2 EXCITATION AND RELAXATION PROCESSES

In a semiconductor, light with photon energies equal to or greater than the band gap can excite electron-hole pairs across the band gap. The duration of the excitation process is defined by the pulse width of the incident light. The exciting energy is transferred to the carriers creating non-equilibrium carrier distributions according to the polarization of the excitation light and k-dependent transition probabilities. The nonequilibrium distribution will achieve an electronic temperature through electron-electron and intervalley scattering. The highly energetic electrons

relax either by emitting optical phonons, or if their energy is sufficiently high, they can scatter among the valleys that comprise the conduction band by intervalley scattering. Eventually the electrons scatter to the conduction band minimum to form a thermal distribution in equilibrium with the lattice. The process of relaxation of excited carriers can broadly be divided into four regimes, which represent different physical processes and time scales. The relaxation processes often overlap and the time boundary between the regimes is not well defined. In the following we first list the physical scattering processes in Table 2.1 and then we describe the time scales where they contribute to the relaxation dynamics [30].

Table 2.1 Relaxation processes after photoexcitation.

Microscopic processes	Characterization
Carrier-carrier scattering	Carrier thermalization
Intervalley scattering	Thermalization between valleys
Intravalley scattering	Thermalization within a valley
Carrier-optical phonon interaction	Equilibration between carriers and lattice
Optical-acoustic phonon interaction	Optical phonon relaxation
Auger recombination	Non radiative recombination of carriers
Radiative recombination	Recombination of carriers with photoemission.

2.2.1 Coherent Regime

First few 10's to ~100 femtoseconds after photoexcitation is the coherent regime of the photoexcited carriers. Carrier-carrier scattering involving both intervalley and intravalley (Figure

2.1) processes starts in this regime. The carriers with sufficient excess energy may scatter to side valleys. This scattering process involves large wave vector phonons. With a suitable experimental technique, coherent dynamics like quantum beats, Bloch oscillations, etc. can be observed. The scattering processes destroy the coherence.

2.2.2 Non-Thermal Regime

After the coherence is destroyed the excited carriers are still in a non-thermal distribution. In this regime a carrier distribution function cannot be characterized by a temperature. Various scattering processes like carrier-carrier and carrier-phonon scattering continue and intervalley scattering can occur in which scattered carriers from side valleys (L and X) are scattered into the center Γ-valley. In addition to intervalley scattering, intravalley scattering will also contribute to the relaxation of the carriers (Figure 2.1). Through all these processes the excited carriers attain a hot thermalized distribution.

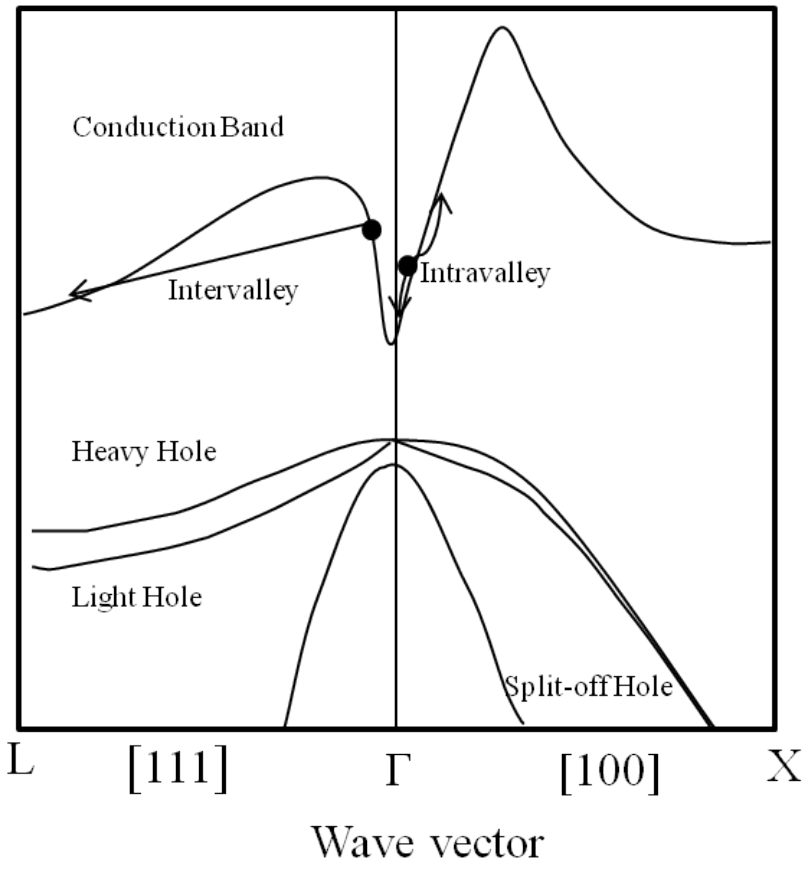

Figure 2.1 Schematic Band Structure of GaAs showing intervalley and intravalley scattering processes.

2.2.3 Thermalized or Hot Carrier Regime

Redistribution of energy among the carriers continues through carrier-carrier scattering that leads to a thermalized carrier regime. In the thermalized or hot carrier regime, the carrier distribution is defined by a carrier temperature. Carriers are still energetic and the carrier temperatures are higher than that of the lattice. Initially electrons and holes thermalize among themselves in hundreds of fs. PL studies have found both electrons and holes thermalize within 100 fs after photoexcitation in GaAs [31]. Time resolved transmission measurements have found hole relaxation times in the range of 120-170 fs depending on carrier density [32]. Within a few

picoseconds electrons and holes achieve a common temperature. Hot carriers and phonons interact and eventually phonons decay through a multiphonon process involving decay of optical into acoustic phonons. Phonon decay times vary depending on the lattice temperature and are around 2-4 ps for LO phonons at room temperature [33]. Through all these processes thermalized carriers and the lattice reach a common temperature in a few tens of ps.

2.2.4 Isothermal or Recombination Regime

At even longer time scales (nanosecond) the carriers and lattice are in equilibrium and can be described by a common temperature. But there are excess carriers present compared to a thermodynamic equilibrium. The excess electron-hole pairs recombine in this regime through radiative and non-radiative (e.g. Auger) recombination mechanisms. After the recombination process the semiconductor reaches the thermodynamic equilibrium again, until the next light pulse initiates another cycle of excitation and relaxation.

2.3 SOME EXPERIMENTAL TECHNIQUES

In ultrafast spectroscopy several experimental techniques are commonly used to study different aspects of carrier-lattice dynamics. Some of these techniques are discussed here [34].

2.3.1 Pump-probe spectroscopy

In a pump-probe spectroscopic technique the output pulse of an ultrafast laser source is divided into two pulses. One of the pulses is used to excite the sample (pump) and the other pulse (probe) is delayed with respect to the pump pulse and is used to interrogate the changes in optical properties induced in the sample. To record the transient material response, the reflected or transmitted probe can be detected as a function of the time delay between the pump and probe pulses. Figure 2.2 shows a schematic diagram for a generic pump probe setup. The time resolution is achieved by the time delay scanning between the pump

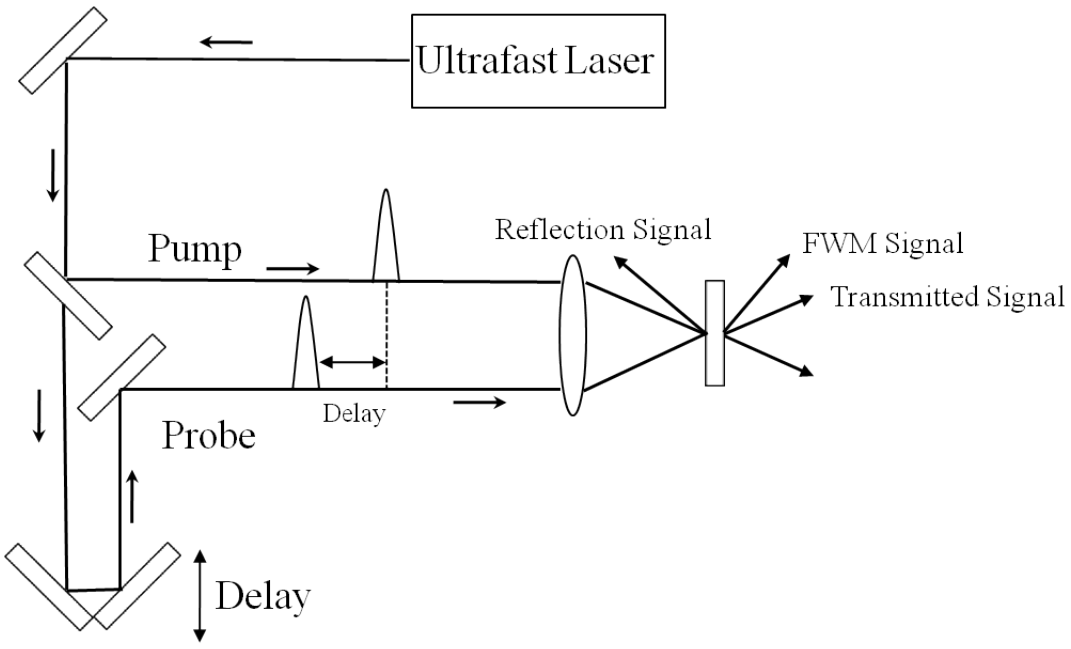

Figure 2.2 Schematic of a generic pump-probe spectroscopy setup.

and probe pulses. The transmitted (reflected) signal is typically represented as a normalized differential transmission (reflection) and is given by $\Delta T/T_0 = (T-T_0)/T_0$ ($\Delta R/R_0 = (R-R_0)/R_0$). Here T_0 (R_0) represent the transmission (reflection) in the absence of the pump and $\Delta T = T-T_0$

($\Delta R = R\text{-}R_0$) is the change in transmission (reflection) induced by the pump. Different variations of pump probe spectroscopy are possible. For example, the reflected or transmitted probe signal can be spectrally resolved to obtain photon energy resolved information. The reflected or transmitted probe signal can also be resolved in two orthogonal polarization directions and the difference of these two signal components can be detected to measure the anisotropy of the material response [35]. Our experiments are a variant of the transient reflectivity technique.

Other than reflection or transmission spectroscopy, time resolved Raman spectroscopy can also be performed using a setup similar to that in Figure 2.2. The changes induced by the pump in the sample are measured by changes in Raman scattering signal generated by the probe. Time integrated Raman signal as a function of the delay between the pump and probe can give information on the non-equilibrium phonon population [36] and carrier relaxation [37]. The polarizations of the pump and probe beams can be chosen to distinguish the Raman scattering from pump and probe beam and also to probe excitations with different symmetry properties. In transient Raman spectroscopy one has to make the choice of the pump and probe pulse duration and the spectrometer resolution, which can compromise what kind of information can be obtained.

2.3.2 FWM Spectroscopy

The simplest implementation of Four-wave Mixing (FWM) spectroscopy is the two beam degenerate four-wave mixing (DFWM) spectroscopy. Two beams as described in a pump-probe spectroscopy (Figure 2.2) are used in this process. Pump photons with wave vector $\mathbf{q_1}$ generate a coherent polarization in the sample. A time delayed probe pulse with wave vector $\mathbf{q_2}$ is incident on the sample after time delay τ. If τ is sufficiently small so that the coherence in the sample is

not destroyed, or in other words if the probe reaches the sample before the dephasing time of the polarization, a polarization grating is produced through interference between the pump and probe induced polarizations in the sample, from which the probe can be diffracted in a third direction ($\mathbf{q_d}$) determined by the phase matching condition $\mathbf{q_d} = 2\mathbf{q_2} - \mathbf{q_1}$. The time integrated FWM signal measures the diffracted energy. In a three beam DFWM experiment two time delays can be controlled between the beams 1 and 2 (τ_{12}) and beams 2 and 3 (τ_{23}). For τ_{12} =0, time dependent FWM signal as a function of τ_{23} gives information on the population decay time (T_1) of the system. Several variations of three beam DFWM experiments can be performed by controlling beam parameters like polarization, time delays between beams etc. Information about dephasing times and details of the dephasing process can also be obtained using three beam DFWM spectroscopy [38, 39].

2.3.3 Photoluminescence Spectroscopy

Photoluminescence (PL) is a process by which the photoexcited carriers in a semiconductor recombine to emit photons. This process is particularly important for direct band gap semiconductors like GaAs. Spectrally and temporally resolving the PL signal can give direct information on the carrier population. The detection of the PL signal can be performed in various ways. The PL signal can be directly detected on a picosecond time scale using a fast photodiode or a streak camera.

For better time resolution correlation spectroscopy or upconversion spectroscopy is performed. In correlation spectroscopy [40] two laser pulses are incident on the sample with a time delay between them. Both the pulses produce luminescence. The correlation between the two luminescence signals is measured using a lock-in detection technique. To perform a

correlation measurement, the two beams are chopped at different frequencies and the correlation signal is detected using a lock-in amplifier at the sum frequency.

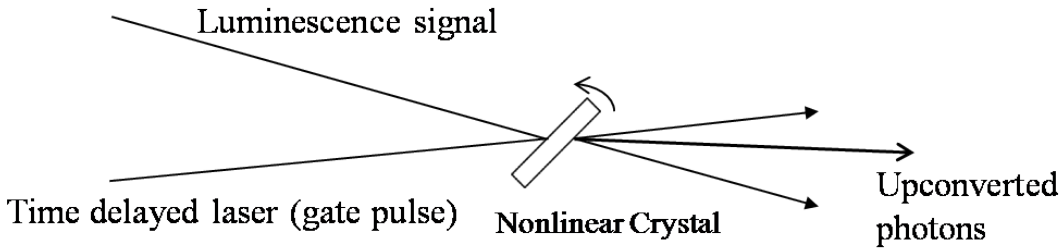

Figure 2.3 Upconversion Geometry

For the femtosecond PL measurements, the PL signal is gated with an ultrafast laser pulse in an upconversion scheme. In the upconversion geometry, the pump beam generates the PL signal and the probe beam detects it by mixing in a nonlinear (NL) sum frequency mixing in an NL optical crystal (e.g. $LiIO_3$) (Figure 2.3). The PL signal collected by a focusing optics from the semiconductor sample and the delayed probe beam are both focused to a common focus on the NL crystal. The angle between the two beams and NL crystal orientation are adjusted for phase matching condition for a sum-frequency generation or upconversion process. The upconversion signal is only produced when the gate pulse is present. Time resolution is limited by the pulse width of the gate pulse, provided that the NL crystal is sufficiently thin, and is obtained by scanning the delay between the PL signal and the gate pulse. The light is spectrally resolved and photon counting electronics are used to obtain time dependent PL spectra for a particular photon energy. The pump-probe delay can also be scanned to measure the time evolution of photoluminescence. With sufficiently short excitation and gate laser pulses, time resolved PL spectra can give information on carrier dynamics [26].

2.3.4 Terahertz Spectroscopy

THz spectroscopy is a powerful experimental technique to obtain information on carrier dynamics and transport. A THz signal is generated by accelerated carriers, so it is particularly useful to explore carrier transport properties. THz spectroscopy can be performed by a variety of techniques. For example, the THz response of a material in response to optical or THz radiation can be probed with a delayed THz probe pulse. A THz field pulse can be generated by different processes like excitation of a photoconductive antenna structure, carrier excitation near semiconductor surfaces with built in electric fields [41], or semiconductor structures with external bias [42], etc. The emitted transient THz fields can also be generated by optical rectification in a non-centrosymmetric electro-optic crystal.

THz fields are usually detected using an electro-optic crystal (e.g. ZnTe or GaP) using a near-infrared laser pulse as the optical gate in an upconversion process (similar to PL upconversion technique). In such a scheme, the time delay between the THz transient and the appropriately shorter gate pulse is used to measure the transient THz field. The time resolution is again limited by only the pulse width of the gate pulse. With a sufficiently short pulse it is possible to detect carrier-lattice interaction processes, which occur on 10 fs to few ps time scale.

Lattice dynamics is detected by various other detection processes, e.g. surface second harmonic generation and THz emission. THz emission is a common method for detecting coherent phonon and plasmon oscillations. Coherent phonons and plasmons are oscillations of charges in a material without inversion symmetry, and accelerating charges emit radiation at their oscillation frequencies (THz range for GaAs). In a suitably constructed nanostructure sample the carriers can be subject to an external electric field and the THz emission properties can be studied [43, 44]. Nanostructure samples are used to control the generation and transport of

carriers with the help of an applied external electric field. With increasing electric field the energetic free carriers interact and exchange energy with the lattice with emission of LO phonon. The THz signal then also contains information on phonon dynamics. In the case of externally biased nanostructures [45], nonequilibrium transport and dynamics can also be studied as a function of the bias field.

2.4 COHERENT PHONON AND PLASMON GENERATION

In the remaining part of this chapter, we present the key theoretical concepts regarding coherent phonons and plasmons, the nonlinear optical response of semiconductor surfaces, and the experimental approach to studying the coupled coherent phonon-plasmon dynamics.

Coherent phonons are the coherent collective oscillations of the lattice as a result of the interaction of the lattice directly with external optical fields or indirectly with the photoexcited carriers. Here coherence refers to macroscopic population of a single mode (q=0) phonon [46].

Coherent optical phonons are oscillations with THz frequency. Corresponding time scales are in 100's of fs. As a result only laser pulses with sufficiently short pulse width can excite lattice vibrations collectively in a single mode and with constant phase relation. Several excitation mechanisms for coherent phonons are possible and will be discussed in detail in the following sections. The doped and excited carriers in a semiconductor also oscillate with a characteristic plasma frequency. The origin of the plasma oscillation in case of GaAs will also be discussed here.

2.4.1 Phenomenological model

Coherent phonon oscillation of amplitude Q can be described phenomenologically as a damped driven harmonic oscillator (Eq. 2.1) [47]. Here the driving term is given by the action of the excitation pulse on the lattice ions of the crystal. The time scale of the force is important, because if it rises faster than the phonon period, the phonons will be excited coherently.

$$\mu\left(\frac{\partial^2 Q_j(t)}{\partial t^2}+2\gamma_{Phonon}\frac{\partial Q_j(t)}{\partial t}+\omega_{Phonon}^2 Q_j(t)\right)=F_j^Q \qquad \text{(Eq. 2.1)}$$

In Eq. 2.1, μ is the reduced lattice mass and γ_{Phonon} is the damping constant related to the dephasing time T_2 of the coherent phonon by $\gamma_{Phonon}=1/T_2$, where the dephasing time $2/T_2=1/T_1+1/T_p$ is a combination of true population decay (T_1) and phase destroying processes (T_p) [48, 49]. ω_{Phonon} is the q=0, i.e., zone center, phonon frequency and F_j^Q is the driving force. Depending on the nature and source of the driving force, the coherent phonon generation can be broadly divided into impulsive and displacive excitation mechanisms.

In the absence of significant interband transitions, e.g. in the case of transparent materials, coherent phonons are generated dominantly by an impulsive process. The driving force F_j^Q is then associated with Raman type processes according to

$$F_j^Q = R_{jkl}E_k E_l\,. \qquad \text{(Eq. 2.2)}$$

Here, R_{jkl} is the Raman tensor and E_k and E_l are the electric field components associated with a broadband laser pulse with electric field polarized in *k* and *l* directions. This kind of generation process has to satisfy energy and momentum conservation given by $\omega_l-\omega_k=\omega_{Phonon}$ and

$k_l - k_k = q_{Phonon}$, where ω_k (k_k) and ω_l (k_l) are the frequencies (wave vectors) associated with the electric field components E_k and E_l and ω_{Phonon} and k_{Phonon} are the phonon frequency and wave vector.

As the phonon generation occurs through a stimulated Raman process and is impulsive in nature, it is called Impulsive Stimulated Raman Scattering (ISRS) mechanism [50, 51]. The force is impulsive, i.e. δ-function like, as it lasts only as long as the duration of the excitation pulse; the resulting phonon amplitude oscillates as $\sin(\omega_{Phonon} t)$. The initial phase of the oscillation is defined by the sinusoidal function.

In another generation process, coherent phonons can be excited by a sudden shift of the equilibrium position of the lattice through interband excitation of carriers. The generation of electrons and holes in the conduction and valence bands causes a sudden shift in the equilibrium position of lattice ions. The lattice ions experience a force associated with this displacement, which starts the lattice oscillation from the displaced position. The force associated with this generation process is created by interband e-h pair excitation, and therefore, it persists on a time scale of carrier scattering and recombination. Therefore, the force term associated with this process can be described as a step function in time. The phonon amplitude and initial phase thus follow $\cos(\omega_{Phonon} t)$ behavior. This mechanism of coherent phonon generation is called Displacive Excitation of Coherent Phonon (DECP)[52]. The generation of fully symmetric A_{1g} phonons of Bi and Sb were explained using this mechanism [53].

In addition to Raman type generation processes, nonlinear polarization effects also have significant contributions to the generation or the force term. The driving force of Eq. 2.1 in this case can be described by

$$F_j^Q = R_{jkl}E_kE_l - \frac{e^*}{\varepsilon_\infty \varepsilon_0} P_j^{NL} \quad . \qquad \text{(Eq. 2.3)}$$

Here P_j^{NL} is the nonlinear longitudinal polarization term, e^* is the effective lattice charge and ε_∞ is the high frequency dielectric constant. The nonlinear polarization can also have several contributions from different physical processes in the material given by,

$$P_j^{NL} = \chi^2_{jkl}E_kE_l + \chi^3_{jklm}E_kE_lE_m + \int_{-\infty}^{t} dt' J_j(t') \quad . \qquad \text{(Eq. 2.4)}$$

The first two terms of Eq. 2.4 are the second and third order nonlinear optical contributions to the nonlinear polarization. The third term describes the polarization contributed by the current density associated with ultrafast charge separation in the probing region. The charge separation occurs on the fs time scale because of a strong electric field within the depletion layer, and through different velocities of drift and diffusion of electrons and holes (photo Dember effect) on relatively longer ps time scale [54]. The ultrafast charge separation near the surface and resultant screening of the depletion layer electric field is the dominant mechanism for coherent phonon generation in III-V semiconductors like GaAs. The details of this generation process will be discussed in the next subsection.

The different terms in the P^{NL} have different symmetry properties with respect to the external field. For GaAs the second order susceptibility χ^2 has the same Γ_{15} symmetry as the Raman tensor R_{jkl} for longitudinal optical lattice oscillation. By contrast, χ^3 has Γ_1 symmetry property i.e. it is isotropic [55]. The third term of Eq. 2.4 is proportional to the photoexcited carrier density, i.e. E^2, and the differential drift velocity between electrons and holes. Studying the incident light polarization dependence of coherent phonon generation can help us identify

different mechanisms through the symmetry properties of the P^{NL}. Symmetry selective excitation of a material can be achieved by exciting it with light having specific polarization of electric field with respect to the crystalline axes.

2.4.2 Screening model

In GaAs, the generation of coherent phonons and plasmons through excitation within the Γ-valley (fundamental band gap) has been attributed to sudden screening of the surface electric field within the surface depletion layer [56]. A surface depletion layer and the associated electric field arise when surface states on GaAs surface trap carriers (electrons or holes) at the surface [57]. Near the surface, the occupation of surface states by charged particles pins the Fermi level within the band gap of GaAs. In the bulk, the Fermi level is near the valance band maximum or conduction band minimum, for p- and n-doped GaAs, respectively. As a result, the conduction and valence bands in n-doped GaAs (used in our experiments) are bent near the surface (Fig. 2.4).

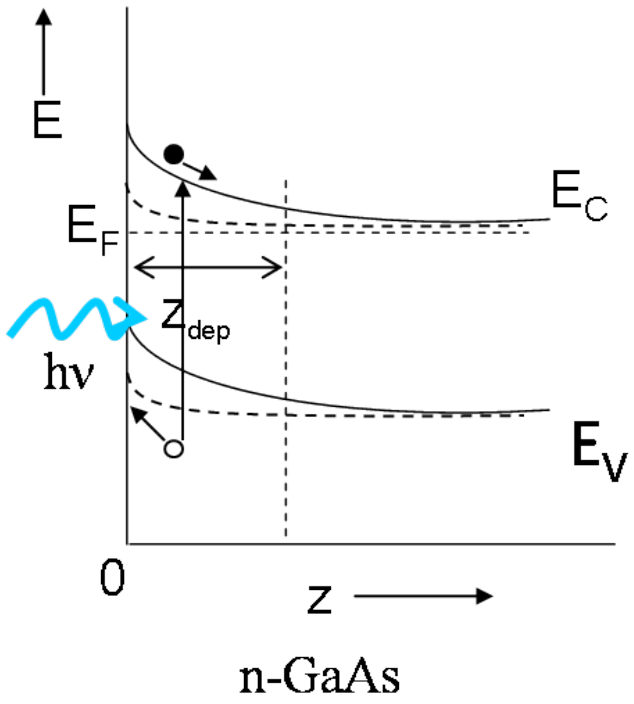

Figure 2.4 Band bending and depletion layer near the surface of n-doped GaAs. The screening process is shown by flattening of the band (dashed line) after photoexcitation.

The band bending results in a depletion or an accumulation layer of majority carriers near the surface, depending on type and extent of doping and a concomitant built-in electric field. The depletion layer depth and the surface electric field, which linearly decreases to zero within the depletion layer, is a function of doping density (N_D) and the built in potential (V_{bi}) generated by the band bending and is given by a Schottky barrier model as [58]

$$E_S = \sqrt{\frac{2qN_D V_{bi}}{\varepsilon_0 \varepsilon_S}} \quad \text{and} \quad Z_{dep} = \sqrt{\frac{2\varepsilon_0 \varepsilon_S V_{bi}}{qN_D}} \qquad \text{(Eq. 2.5)}$$

where E_S is the surface electric field Z_{dep} is the depth of the depletion layer, and ε_S is the static dielectric constant. The depletion layer field (E_{Dep}) displaces the polar Ga and As atoms near the

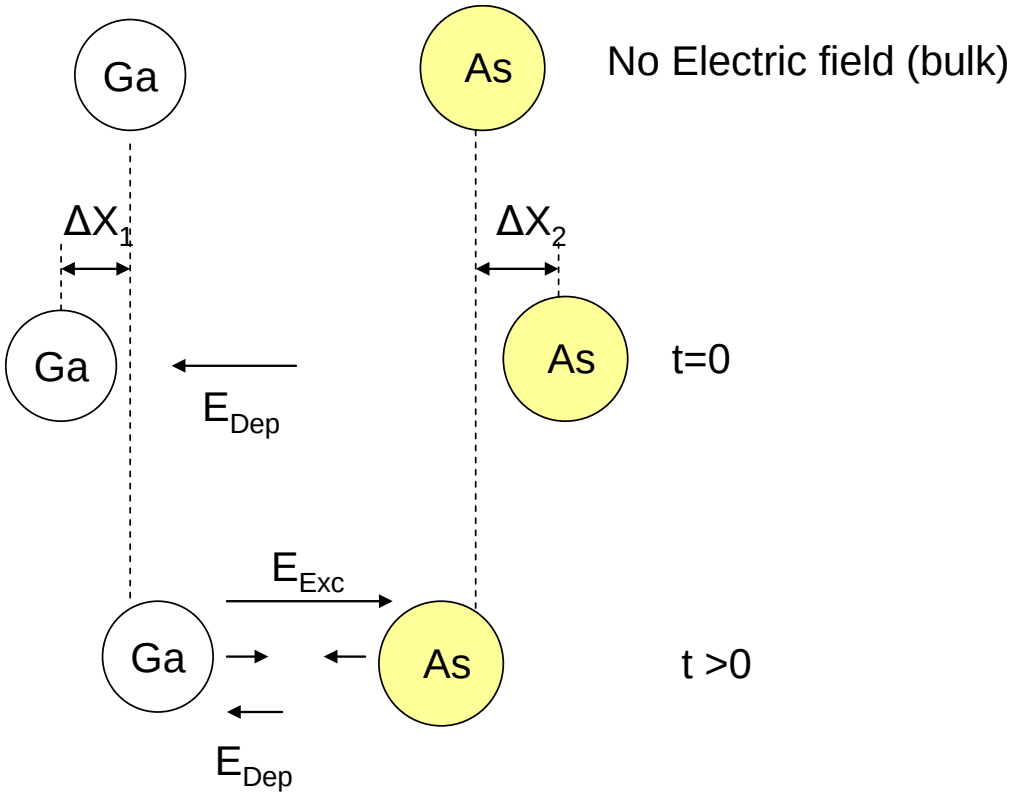

Figure 2.5 Screening of depletion layer electric field results in coherent phonon excitation of polar GaAs.

surface in a GaAs crystal along the longitudinal direction, given by ΔX_1 and ΔX_2 respectively, (Figure 2.5) even before any photoexcitation happens (time t=0). The Ga and As atoms are thus under an in-built tension, which can be visualized as a stretched spring connecting them, with the spring signifying the mutually attractive force [56].

When a large number of carriers, both electrons and holes, (estimated to be 10^{18}-10^{20} cm^{-3} in our case), are generated within the depletion layer by the incident photons at time t>0, the photogenerated carriers get instantaneously polarized due to presence of the depletion electric field (E_{Dep}), an electric field of polarized photocarriers E_{Exc} is generated, screening the built-in field. Due to this sudden screening, the force responsible for the tension between Ga and As atoms is released. The screening of the depletion layer electric field happens on the same time

scale as the photoexcitation of the carriers. It acts like a step-function force suddenly on Ga and As atoms; as a result the GaAs lattice starts vibrating in the longitudinal direction with the longitudinal optical (LO) phonon frequency. Because the force is generated suddenly on the time scale of phonon oscillation, the phonons oscillate with the same phase, i.e., coherently. The extent of screening of the depletion electric field depends on the photoexcited carrier density. The screening is responsible for the sudden generation of force and is symmetry independent. With increasing photoexcitation density the force increases linearly and the phonon amplitude shows a linear increase. When the screening of the depletion layer electric field is complete, the phonon amplitude saturates. The generation of coherent phonon in this process does not depend on the polarization of the excitation pulse. The experimental results, which will be discussed in further detail in chapters 3 and 4, clearly demonstrate that the screening mechanism is the dominant generation mechanism of coherent phonons in GaAs.

The plasma oscillation in GaAs also results from the instantaneous polarization of photoexcited electrons and holes within the depletion layer due to the electric field within the depletion layer [43]. The polarization of the carriers and associated restoring force starts the plasma oscillation, the frequency of which is given by

$$\omega_{e,h} = \sqrt{\frac{ne^2}{m^* \varepsilon_0 \varepsilon_\infty}} \qquad \text{(Eq. 2.6)}$$

Where m^* is the effective mass of the carrier and n is the excitation density and ε_∞ is the high-frequency dielectric constant. Electrons and holes have different effective masses resulting in different plasma frequency even at same carrier density. Electrons also can occupy different valleys in the conduction band characterized by different effective masses with corresponding difference in the plasma frequencies.

2.4.3 Plasmon-Phonon coupling

The plasma frequency increases with increasing carrier density. With significant density the plasma frequency may be comparable to or higher than the phonon frequency. When it interacts with phonons through Coulomb interaction, the plasmon and phonon modes are renormalized and form the coupled plasmon-phonon modes. In polar semiconductors, for longitudinal phonons the coupling of the phonon amplitude Q and the carrier plasma polarization P is given by the coupled equations [59]

$$\frac{\partial^2}{\partial t^2}P_j + \gamma_{Plasma}\frac{\partial}{\partial t}P_j + \omega_{el}^2 P_j = \frac{ne^2}{\mu\varepsilon_\infty}\left(E_j^{ext} - 4\pi\gamma_{12}Q_j\right) \qquad \text{(Eq. 2.7)}$$

$$\frac{\partial^2}{\partial t^2}Q_j + \gamma_{phonon}\frac{\partial}{\partial t}Q_j + \omega_{el}^2 Q_j = \frac{\gamma_{12}}{\varepsilon_\infty}\left(E_j^{ext} - 4\pi P_j\right). \qquad \text{(Eq. 2.8)}$$

Here, E_j^{ext} is the macroscopic electric field, and γ_{12} is a coupling constant given by $\gamma_{12} = \omega_{TO}\sqrt{(\varepsilon_0 - \varepsilon_\infty)/(4\pi)}$. The damping constants of the plasma and phonon oscillations are given by γ_{plasma} and γ_{phonon}, respectively, and n is the density of the plasma.

Eq. 2.7 and 2.8 describe the macroscopic coupled plasma-phonon dynamics. For homogeneous density and negligible damping, the common solutions of these two equations reproduce the coupled plasmon-phonon frequencies given by

$$\omega_\pm = \frac{1}{2}\left(\omega_{LO}^2 + \omega_P^2 \pm \sqrt{(\omega_P^2 + \omega_{LO}^2)^2 - 4\omega_P^2\omega_{TO}^2}\right). \qquad \text{(Eq. 2.9)}$$

Here ω_P is the plasma frequency as stated in Eq. 2.6 for an electron (ω_e) or hole plasma (ω_h). Coupled plasmon-phonon modes are the hybrid oscillation modes in the material with two renormalized frequencies that are referred to as the L+ and L- modes. The frequency change of

the bare LO phonon from its characteristic frequency due to the coupling with the plasma oscillation can be considered as dressing of the phonon by plasma. These dressed phonons are the new quasiparticles generated in the process, which oscillate at the renormalized frequencies.

2.5 COHERENT PHONON AND PLASMON DETECTION

Coherent phonon and plasmon oscillations directly modulate the dielectric properties of a material. Phonon and plasmon oscillations can be detected by recording the change in the dielectric constant by measuring the reflectivity of a material. In our experiment, the reflectivity is measured in pump-probe geometry as a function of pump-probe delay time. The change in reflectivity can be written as [60]

$$\Delta R = \frac{\partial R}{\partial n}\Delta n \sim \frac{\partial R}{\partial \chi}\left\{\left(\frac{\partial \chi}{\partial Q}\right)_F + \left(\frac{\partial \chi}{\partial F}\right)_Q \left(\frac{\partial F}{\partial Q}\right)\right\}\Delta Q \qquad \text{(Eq. 2.10)}$$

where the first term in the brackets is given by the change in the susceptibility through the displacement of the phonon coordinate Q, i.e., it is the Deformation Potential (DP) term, and the second term is the change in the susceptibility through the applied field F, i.e., it is the electro-optic term. There can be another contribution to the reflectivity change due to polar electron-phonon interaction (Fröhlich interaction [61]). GaAs falls in cubic symmetry class $\bar{4}3m$. For this symmetry class, the DP Raman tensor belongs to the Γ_{15} irreducible representations of the crystal point group, and phonon modes of the corresponding symmetry can be detected by probing with the appropriately polarized light [62].

The electro-optic contribution to the change in reflectivity (second term in Eq. 2.10) can have linear and nonlinear contributions. In terms of the nonlinear optical susceptibilities the change in reflectivity due to the electric field can be expressed with a general expression [63]

$$\frac{\Delta R}{R} = \mathrm{Re}[C n_i n_j \Delta\varepsilon_{ij}] = \mathrm{Re}\left\{C\left[n_i n_j E_k \chi^{(2)}_{ijk} + n_i n_j E_k E_l \chi^{(3)}_{ijkl}\right]\right\}, \quad \text{(Eq. 2.11)}$$

where C is a constant that varies with the energy of the probing light. The n_i and n_j 's are the i^{th} and j^{th} component of the polarization vector $\hat{n}$ of the incident light. E_k and E_l are the components of the electric fields and $\chi^{(2)}$ and $\chi^{(3)}$ are second and third order nonlinear optical susceptibilities. The terms of the Eq. 2.11 are summed over the three Cartesian coordinates x, y and z and measured with respect to the crystal symmetry.

The first term on the right hand side of Eq. 2.11 describes the linear electro-optic effect, which is also called the Pockels effect. In crystals exhibiting a linear EO effect, coherent phonons can be detected via the associated THz longitudinal electric field. Considering only the linear contribution, the Eq. 2.11 represents contributions to the change in reflectivity due to second-order optical nonlinearity $\chi^{(2)}$. The linear eletro-optic effect and the DP contribution thus have the Γ_{15} symmetry $\chi^{(2)}$ tensor and can be studied by detecting the coherent phonon with linearly polarized light with electric field polarized along different crystalline axes. For optical phonon polarized along longitudinal direction ([100] or x direction for our case; we consider [010] as y and [001] as z) the DP Raman tensor has only two nonzero components and has the form

$$R_{DP} = \begin{pmatrix} 0 & 0 & 0 \\ 0 & 0 & a_{DP} \\ 0 & a_{DP} & 0 \end{pmatrix}. \quad \text{(Eq. 2.12)}$$

The second order NL optical susceptibility $\chi^{(2)}$ has only two equal nonzero off diagonal elements in the susceptibility tensor [64], which include the deformation and electro-optic contributions. For longitudinal direction the $\chi^{(2)}$ tensor takes the form

$$\chi^{(2)} = \begin{pmatrix} 0 & 0 & 0 \\ 0 & 0 & a_{NL}^{(2)} \\ 0 & a_{NL}^{(2)} & 0 \end{pmatrix} . \qquad \text{(Eq. 2.13)}$$

The electro-optic contribution to the phonon detection can also be excited by third-order optical nonlinearity, which is associated with the Franz-Keldysh effect. The Franz-Keldysh effect is resonantly enhanced near critical points of interband transitions. This resonant contribution can be studied by tuning the photon energy of the pump and probe pulses through electronic resonances of the sample [60]. The third-order optical nonlinearity $\chi^{(3)}$ has only diagonal non-zero terms for cubic $\bar{4}3m$ symmetry [64]. The form of the tensor is

$$\chi^{(3)} = \begin{pmatrix} a_{NL}^{(3)} & 0 & 0 \\ 0 & a_{NL}^{(3)} & 0 \\ 0 & 0 & a_{NL}^{(3)} \end{pmatrix} . \qquad \text{(Eq. 2.14)}$$

In Eq's. 2.13 and 2.14 $a_{NL}^{(2)}$ and $a_{NL}^{(3)}$ are the non-vanishing 2nd and 3rd order NL optical tensor elements.

The Fröhlich interaction contribution to the reflectivity change has Γ_1 symmetry and corresponding Raman tensor has the form [65].

$$R_F = \begin{pmatrix} a_F & 0 & 0 \\ 0 & a_F & 0 \\ 0 & 0 & a_F \end{pmatrix} \qquad \text{(Eq. 2.15)}$$

The third-order Fröhlich contribution, i.e. the Franz-Keldysh effect, thus contributes to the $\chi^{(3)}$ changes in reflectivity.

The change in reflectivity due to non-linear susceptibilities (Eq. 2.11) can be reduced considering symmetry properties of the susceptibility tensors as described by Eq. 2.13 and 2.14. For a longitudinal electric field (along [100] or x direction), the second-order susceptibility contribution to the change in reflectivity of Eq. 2.11 will be proportional to $a_{NL}^{(2)} \sin 2\theta$, where θ is the angle between the [001] or z direction and the polarization direction of the probe pulse . By contrast, the third order susceptibility contribution will be angle independent ($a_{NL}^{(3)}$) [63].

2.5.1 Electro Optic Symmetry

The electro-optic impermeability tensor is defined as $\eta = \frac{\varepsilon_0}{\varepsilon}$, where ε is the dielectric constant.

The change in the impermeability tensor due to applied electric field is given by [66]

$$\Delta\eta_{ij} \equiv \Delta\left(\frac{1}{n^2}\right)_{ij} \equiv r_{ijk} E_k \qquad \text{(Eq. 2.16)}$$

Here, n is the refractive index, E_k is the k component of the electric field (k=x,y,z) and r_{ijk} are the linear EO coefficients which can be expressed as a (6x3) tensor. For GaAs, the electro-optic tensor has the form

$$\begin{bmatrix} 0 & 0 & 0 \\ 0 & 0 & 0 \\ 0 & 0 & 0 \\ r_{41} & 0 & 0 \\ 0 & r_{41} & 0 \\ 0 & 0 & r_{41} \end{bmatrix} . \qquad \text{(Eq. 2.17)}$$

For an electric field along the longitudinal ([100] or x) direction the direction dependent dielectric constants are given by

$$n_y = n_0 + \frac{1}{2} n_0^3 r_{41} E_{[100]} \sin 2\theta \qquad \text{(Eq. 2.18)}$$

Here θ is defined in the previous section.

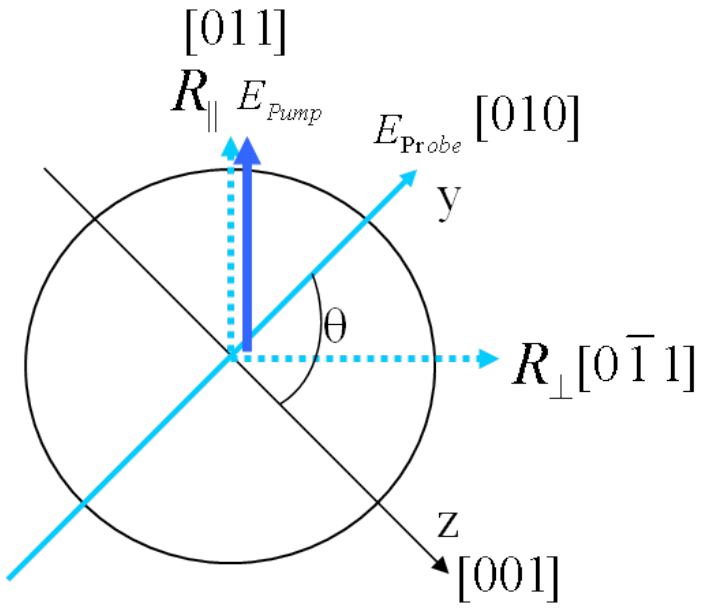

Figure 2.6 Geometry of pump-probe spectroscopy. The incident pump and probe beams are shown by solid arrows and reflected polarization resolved probes are shown as dotted arrow. The x-axis is going into the plane, the longitudinal direction.

A typical pump-probe geometry in electro-optic sampling measurement is shown in Figure 2.6. The sample is GaAs oriented in the (100) direction. The pump electric field vector is along the [011] direction. The longitudinal polarization induced by the pump pulse is perpendicular to the sample surface, along the [100] direction; it causes the dielectric properties to be modulated with the opposite phase along the [011] and $[0\bar{1}1]$ directions. This induced birefringence is detected by subtracting the polarization components of the reflected probe beam along the parallel ([011])

and perpendicular ($[0\bar{1}1]$) directions to the pump electric field vector. The corresponding anisotropic reflectivity change is given by [56]

$$\frac{\Delta R}{R_0} = \frac{\Delta R_{[011]}(t) - \Delta R_{[0\bar{1}1]}(t)}{R_0} = \frac{4 r_{41} n_0^3}{n_0^2 - 1} \Delta E_{[100]}(t) \ . \qquad \text{(Eq. 2.19)}$$

Here, r_{41} is the electro-optic coefficient, n_0 is the refractive index of the unexcited system, and $\Delta E_{[100]}(t)$ is the time dependent change in the longitudinal electric field associated with the coherent phonon and plasmon oscillations.

In our experiments coherent plasma oscillations modulate the dielectric function of the material and are detected by detecting the change in reflectivity. The time dependent reflectivity signal contains information from both coherent phonon dynamics and coherent plasma dynamics. Our experiment, therefore, measures the coupled coherent dynamics of the free charge carriers and the crystal lattice.

2.6 EXPERIMENTAL SET UP

We perform pump-probe spectroscopic experiments in reflective electro-optic sampling (REOS) geometry or in transient reflectivity geometry. The schematic experimental setup is shown in Figure 2.7. We use mode-locked Ti:Sapphire laser pulses with ~10 fs pulse duration and wavelength centered around 800 nm. The repetition rate of the laser is 65 MHz. The 800 nm output is used to produce the second harmonic light at 400 nm using a 50 micron thick BBO crystal. By changing the phase matching angle, the wavelength of the second harmonic can be tuned in a range of 390-410 nm. The 400 nm light is used to perform pump-probe experiments.

3.1 eV photons excite electron-hole pairs near-resonantly in the L valley of GaAs band structure near E_1 and $E_1+\Delta_1$ critical points as described in Section 1.1. The blue light is divided into two parts using a beam splitter. The more intense pump beam is reflected by a retro-reflector placed on an oscillating delay line. The sinusoidal oscillation frequency of the delay is typically set at 20 Hz. Both the pump and probe beams pass through a half-wave plate and polarizer combination. This lets us control the linear polarization and the intensity of the polarized light passing through it, and balances the dispersion in the two paths. The oscillating delay line allows us to average our signal over many cycles of pump probe delay.

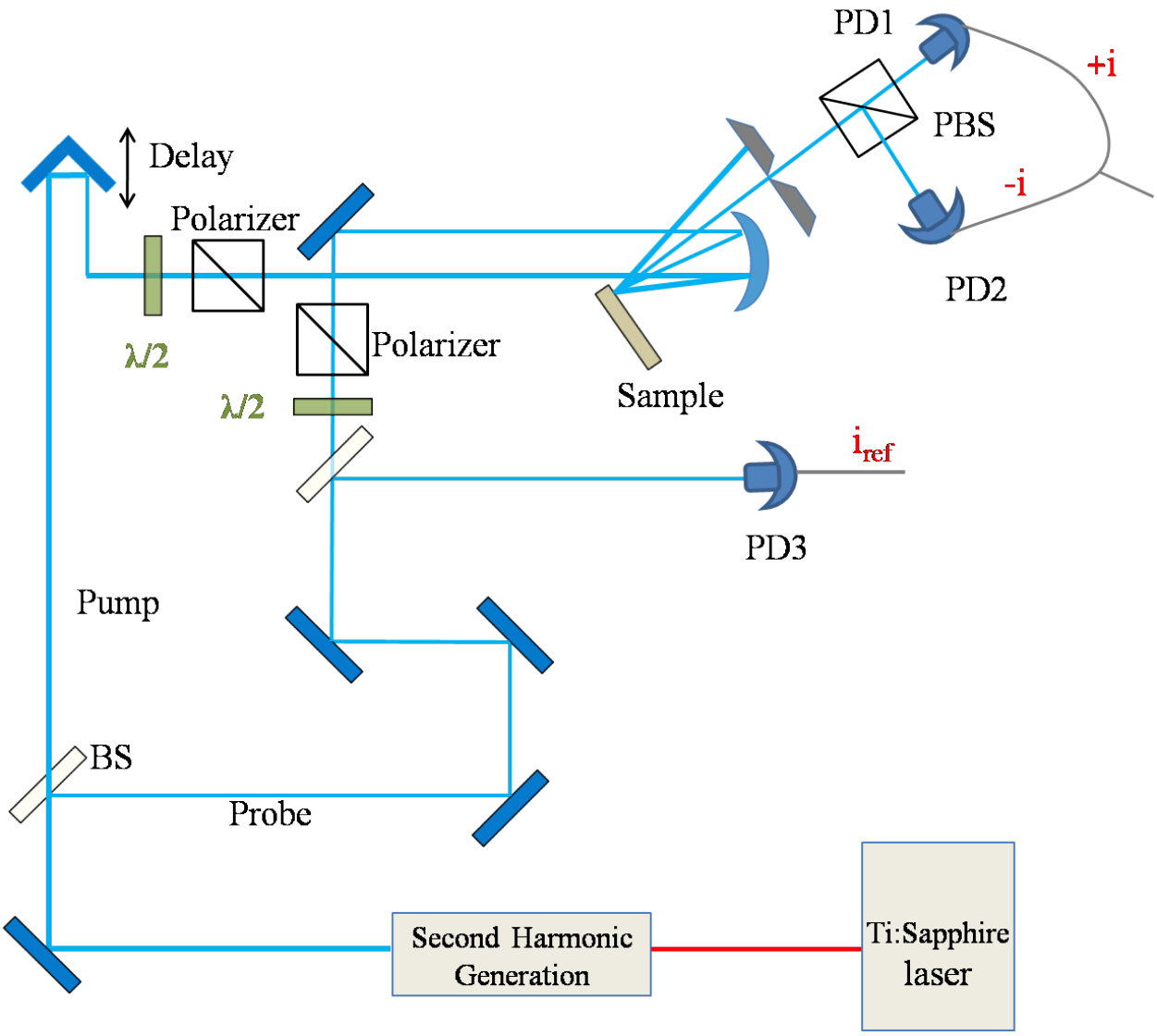

Figure 2.7 Schematic experimental setup in pump-probe reflective electro-optic sampling geometry.

The pump and probe beams are then focused onto the sample surface with a common concave mirror at 15° and 5° angle to the surface normal. When the two beams are parallel, the mirror focuses them to a common spot on the sample. Mirrors of 5, 10, and 15 cm focal length can be employed to vary the fluence range. For the 10 cm focal length mirror, the pump probe spot size on the sample surface is measured to be 40 micron in diameter. From the published absorption coefficient [67], the measured average power, the repetition rate of the laser pulses, and the laser spot diameter on the sample, we can estimate the excited carrier density in the sample. By

changing the pump intensity either with the polarization rotator or by selecting the focal length of the focusing mirror we can vary the excited carrier density. The polarization of the pump is kept at 90° to the optical plane and that of the probe is kept at 45° with respect to the pump (Figure 2.6)

The sample is placed on a 6-axis movable stage with control over both the orientation and position of the sample. The optical paths of the pump and probe beams are adjusted by a mechanical stage so that the path length of the pump beam is scanned by the oscillating delay through the zero delay between them. The reflected pump beam from the sample surface is blocked and the reflected probe is transmitted through an iris. A polarizing beam-splitter (PBS) resolves the probe beam into two orthogonal polarization components, one of which is transmitted through the polarizer and the other one is reflected in the perpendicular direction. In this way two orthogonal components of the reflectivity ($R_{\parallel}$ and $R_{\perp}$ with respect to the pump) are detected by two balanced photodiodes (PD1 and PD2). The signals are subtracted to record the anisotropic component of the reflectivity as a function of the pump-probe delay, the isotropic component being subtracted. The signal is amplified by a gain factor of 10^5-10^6 in a two stage voltage pre-amplifier and passed through a band pass filter of bandwidth 300kHz. The first amplifier is a DHPCA-100 manufactured by FEMTO Masstechnik GmbH. The second one is a low noise voltage amplifier SR560 made by Stanford Research Systems. Finally the signal is viewed and recorded with a digital oscilloscope, LeCroy Wavepro 7000. The oscillation of the delay is driven by a sinusoidal function from a function generator, which is also used to trigger the oscilloscope. Care is taken to record the signal in the linear portion of the displacement of the delay stage so that the signal has a minimal distortion. The signal is also normalized with respect to the reflectivity without the pump. This setup of detection is the Reflective Electro Optic

Sampling (REOS) geometry; it can detect small ($<10^{-6}$) anisotropic changes in reflectivity. The experimental results described in Chapter 3 are obtained using this experimental method.

We can also detect the transient reflectivity by removing the PBS from the path of the reflected probe beam and measuring the signal by PD1 as a function of the pump-probe delay. In this setup we detect a portion of the probe beam by a third photodiode (PD3) before it is focused onto the sample, and subtract this signal from the transient reflectivity signal to improve the signal to noise ratio. This signal is also amplified using the voltage pre-amplifier and recorded in the digital oscilloscope. The signal includes both isotropic and anisotropic changes in the reflectivity. Moreover this signal includes information on the reflectivity change in a particular crystalline direction of the sample defined by the polarization of the probe beam and orientation of the sample. By changing the probe polarization and keeping the sample orientation fixed, the transient reflectivity along different crystalline directions can be measured. The results presented in Chapter 4 are obtained using this experimental procedure.

In both experimental set ups the oscillating delay allows us to collect and average data over several thousand cycles of pump-probe delay. In this way we can improve the signal-to-noise ratio. The voltage pre-amplifier allows us to select a suitable gain bandwidth and gain factor for best signal-to-noise ratio.

2.6.1 Calibration of the Delay

The pump-probe delay scanning is intrinsically nonlinear and needs to be calibrated to obtain calibrated and linearized delay information. This is accomplished with a Mach-Zehnder interferometric setup using a separate He-Ne laser as the calibration source. The laser output is

divided into two parts using a beam splitter. One of the beams is reflected by the retro-reflector on the delay line and the other part of the beam travels in

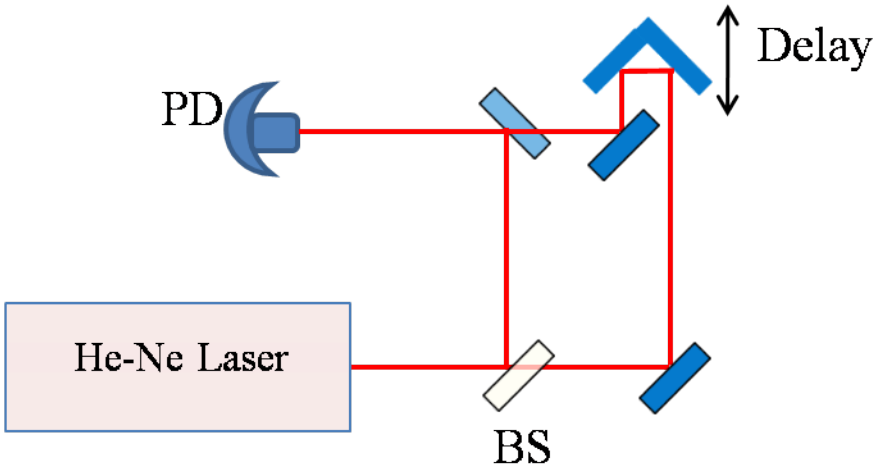

Figure 2.8 Schematic set up for pump-probe delay calibration.

a different but fixed optical path. The two beams are then overlapped on a photodetector (PD) to detect the interference fringes generated by the optical path difference between the two beams. The interferogram is recorded in the digital oscilloscope and is analyzed using a calibration program to determine the time delay corresponding to the different positions of the oscillating delay line. In our experiments, the displacement of the delay stage can introduce up to 8 ps delay between the pump and probe beams.

3.0 CARRIER DENSITY DEPENDENT PLASMON-PHONON RESPONSE

3.1 INTRODUCTION

The generation of coherent phonons in GaAs can have a contribution from the screening of the depletion layer electric field, which acts as an ultrafast displacive force on the lattice and starts the process of coherent oscillations of the Ga and As atoms [56] (Section 2.4.2). The screening depends on the carrier densities of the excited photocarriers [68]. With increasing carrier density the excited electric field will saturate the depletion layer electric field completely. So the screening mediated generation force will saturate with increasing carrier density. For Raman scattering mediated coherent phonon generation (discussed in Chapter 2 as ISRS), the amplitude of the phonon increases with the excitation fluence, and is not expected to saturate unless the optical transition also becomes saturated. Thus studying carrier density dependent response of GaAs due to coherent phonon oscillations can reveal which mechanism is dominant in the coherent phonon generation in GaAs. Plasmon oscillation is also generated due to excited electron-hole plasma, the strength and frequency of which also depend on the plasma density. The LO phonon and plasmon couple with each other via Coulomb interaction and the coupled plasmon phonon modes are formed. The frequencies of the coupled modes change with the carrier density. Studying frequency behavior of the coupled plasmon-phonon modes with carrier density can reveal which type of carrier dominates the dynamics at different regimes of carrier

density. By using 400 nm light we are only exciting and probing up to a very small (15 nm) depth near the surface defined by the absorption depth of the light. Thus, transport of various kinds of carriers that are generated, towards bulk can play a vital role in the dynamical changes of the optical properties of the sample.

In this chapter, we discuss the carrier density dependent plasmon and phonon properties. We discuss the response of GaAs in the time and frequency domains. We also discuss phonon and plasmon intensity and dephasing time dependence on the photocarrier density. We also analyze the coupled mode frequency change with carrier density and compare the experimental results with calculated results using a model for the coupled plasmon-phonon response.

3.2 EXPERIMENTAL DETAILS

The transient response of n-doped GaAs is generated and detected at an excited e-h pair density n_{exc}~10^{18}-10^{20} cm^{-3} with 10 fs laser pump and probe pulses centered at 400 nm. The sample is a [100] oriented Si doped GaAs (doping concentration, n_d= $2x10^{18}$ cm^{-3}) wafer. The measurements are performed at room temperature under ambient conditions, by measuring transient changes in the reflected light intensity employing the reflective electro-optic sampling geometry [35, 56]. Linearly polarized pump and probe beams are focused with concave mirrors of different focal length to roughly 10 - 40 μm size spot onto the sample surface to create a nonequilibrium electron-hole plasma in the density range of $2x10^{18}$ – $3x10^{20}$ e-h pairs/cm^3 within an optical penetration depth of ~15 nm. The optical penetration depth is determined by the published absorption coefficient of the material, which depends on the photon energy [67]. For 400 nm light the optical penetration depth in GaAs is ~15 nm. The depletion layer depth near the surface

of our sample, which is created due to surface band bending as described in Section 2.4.2, is roughly of the same order (22 nm for $n_d = 2x10^{18}cm^{-3}$). The pump pulse, polarized along the [011] crystallographic direction, creates an anisotropic (real and k-space) photoinduced electron-hole plasma, which transiently changes the optical properties of the crystal. The delayed probe pulse has its polarization along the [001] direction, i.e. it is rotated by 45^0 with respect to the pump. After reflection, the probe light is analyzed into parallel [011] and perpendicular $[0\bar{1}1]$ components (Figure 2.6) with respect to the pump and detected by balanced photodiodes. Each polarization component of the reflected light measures the changes in the isotropic and anisotropic optical properties of the crystal along the respective crystal axes. The difference between the two signals $\Delta R_{eo} = \Delta R_{\parallel} - \Delta R_{\perp}$, which subtracts the isotropic from the anisotropic response, is recorded as a function of the pump-probe delay.

3.3 EXPERIMENTAL RESULTS

In Figure 3.1, the anisotropic reflectivity signal is shown with respect to time delay for various photoexcited carrier densities. Photoexcited carrier densities near the surface are estimated from the measured average powers of the pump using the method described in section 2.6. It consists of three main components: (i) a near instantaneous transient electronic response; (ii) followed by a fast decaying oscillatory coupled plasmon-phonon response; and (iii) a long-lived (decay time τ=2-4 ps) oscillatory bare LO phonon response. With increasing carrier density the amplitude of the fast decaying signal increases, but the bare LO phonon oscillation amplitude remains unchanged. Fourier analysis (Figure 3.2) of the time domain signals shows features attributed to the bare LO phonon and the lower branch of the LO phonon-plasmon coupled mode (L-). The

upper branch (L_+) is most likely not observed because it is overdamped, i.e. its damping rate is faster than the LO phonon oscillation period. With increasing photocarrier density, the LO phonon frequency (8.7 THz) and amplitude are essentially unaffected, whereas the L- peak frequency red shifts towards the TO phonon (8.0 THz) limit and its amplitude increases. With increasing carrier density the L- peak grows stronger and becomes the dominant feature of the spectra. The decay time of the coupled plasmon-phonon (L-) mode changes from near 1 ps at the lowest carrier density ($1.6x10^{18}$ cm^{-3}) to near 0.5 ps at higher ($2x10^{19}$ cm^{-3}) carrier densities. At 3.2 ps, the decay time constant of the LO mode is considerably longer than the L- mode, and is independent of the carrier density.

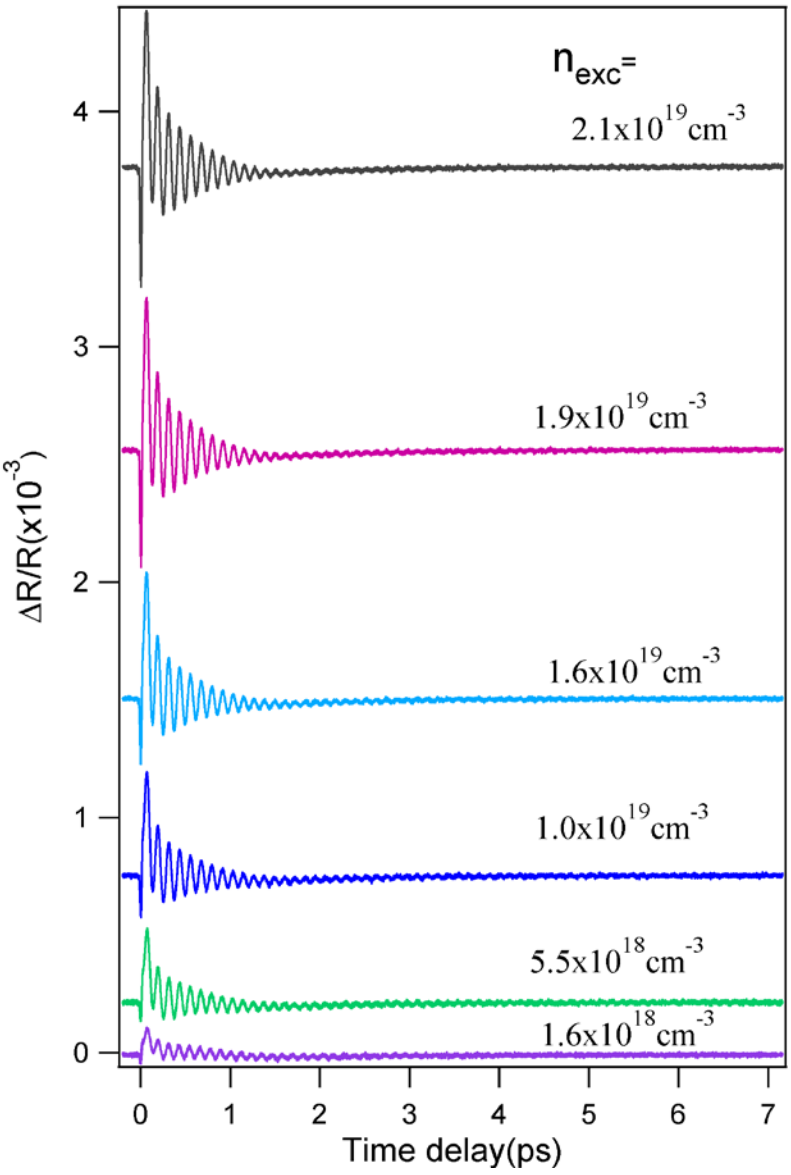

Figure 3.1 Anisotropic reflectivity as a function of time delay at different photoexcitation levels. Individual scans are displaced in the vertical direction for clarity

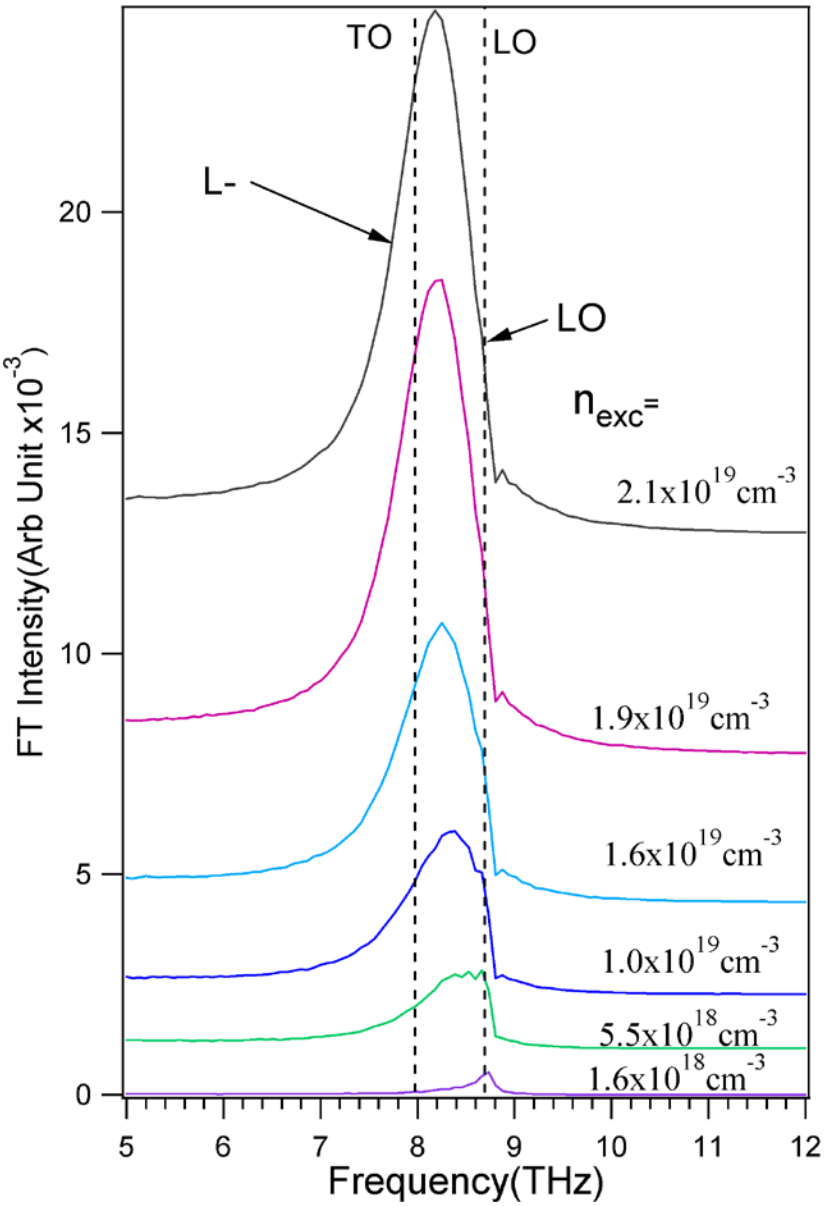

Figure 3.2 FT's of the time dependent reflectivity signals showing bare LO phonon response and lower branch of the plasmon-phonon coupled mode (L-). The dotted lines are the bare TO and LO phonon frequencies. Individual spectra are displaced in vertical direction.

3.4 CARRIER DENSITY DEPENDENCE OF COHERENT PHONON AND PLASMON RESPONSE

We extract the peak intensities of the bare LO phonon and coupled L- modes amplitudes and study their behavior with changing photo-excited carrier density. We determine the peak intensities by fitting the spectra with a fit function consisting of two Lorentzian peaks, one corresponding to the L- peak and another corresponding to the LO peak. Because of the asymmetry of the peak and the difference between the widths of the two peaks, the FT peak corresponding to LO phonon frequency appears as a sharp edge on top of the broad L- peak. This makes the peak fitting difficult. By fixing some of the known parameters (e.g. location of peak value, width) of the Lorentzian peak function corresponding to LO phonon we get a reasonable fit.

Figure 3.3 shows the extracted peak height with estimated average carrier density between (a) $1.6\text{x}10^{18}$ cm^{-3} to $2.1\text{x}10^{19}$ cm^{-3} and (b) $3.1\text{x}10^{19}$ cm^{-3} to $2.7\text{x}10^{20}$ cm^{-3}. For lower ($1.6\text{x}10^{18}$ cm^{-3} to $2.1\text{x}10^{19}$ cm^{-3}) density regime (Figure 3.3(a)), the LO phonon intensity is linear indicating the linear increase of the driving force with increasing carrier density. This suggests that the screening of the depletion layer electric field, which determines the driving force, is not complete in this density regime. The L- peak amplitude increases superlinearly, which may be caused by a limitation of the fitting model in obtaining reliable peak amplitudes at low carrier densities; under these circumstances, as can be seen in Figure 3.2, the FT spectra do not show a distinct Lorentzian lineshape for the L- peak.

In the higher density regime (Figure 3.3 (b)) the LO phonon intensity does not change with carrier density showing saturation of the driving force. Because this behavior occurs at much lower excitation densities than required for saturation of the optical transition, it indicates

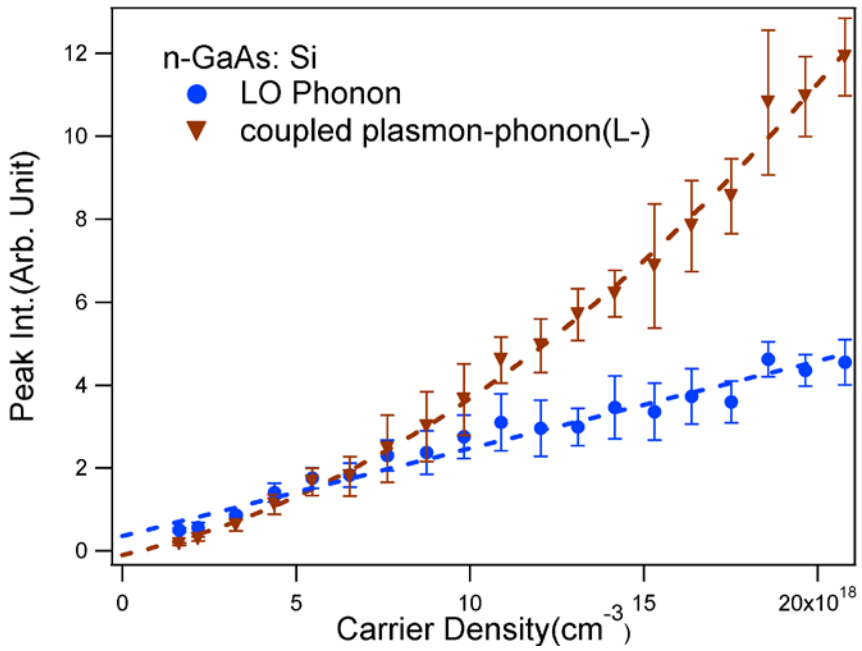

(a)

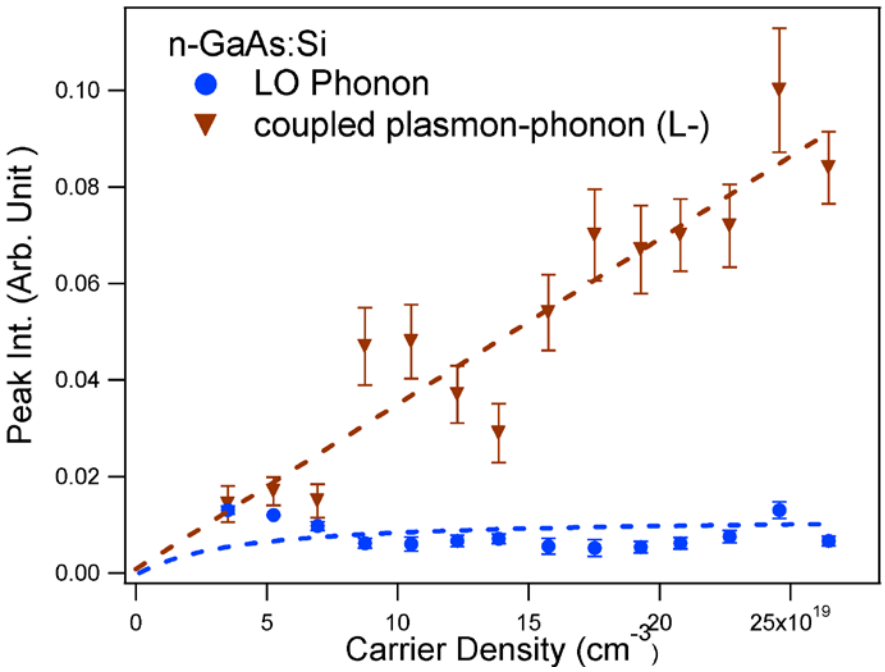

(b)

Figure 3.3 Amplitudes of the LO phonon and L- contribution to the FT spectra with changing carrier densities at two carrier density regimes

that the screening of the depletion layer electric field is the more likely explanation. Above the critical density of >3x10^{19} cm^{-3}, increasing the photocarrier density even further does not increase the driving force for excitation of coherent phonons. This behavior is quite similar to what has been observed for doped GaAs with pump and probe near the fundamental band gap, [69] although the critical density is somewhat higher than what has been reported for a similarly doped sample with photoexcitation near the fundamental band gap [56]. In the higher density regime the L- amplitude increases linearly with carrier density indicating the dominance of the plasmon oscillation to the coupled mode.

We also extract decay times of the fast decaying plasmon-phonon coupled oscillation (L-) by fitting exponentially damped harmonic oscillators to the fast decaying oscillatory signal and observe how it changes with increasing carrier density. Figure 3.4 shows the behavior of this decay time with carrier density. At lower densities (between 1.6x10^{18} cm^{-3} to 2.1x10^{19} cm^{-3}) the decay time decreases from 0.93 ps to 0.48 ps. (Figure 3.4(a)) The decay of the plasmon-phonon

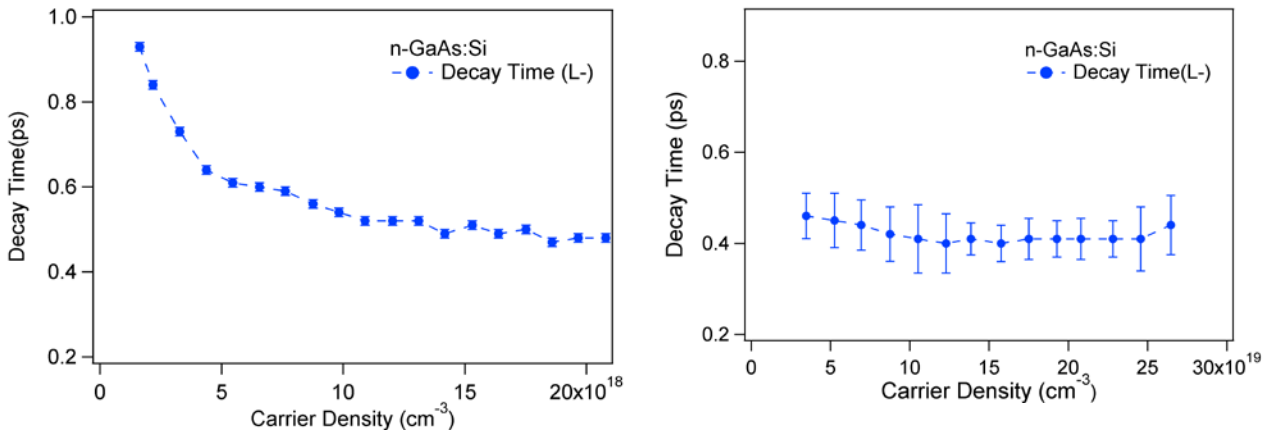

Figure 3.4 Coupled mode (L-) decay times with increasing carrier density for two regimes of carrier density.

coupled mode is dominated by the plasmon damping. It has contributions from the dephasing and population decay of the plasmon and also from bare LO phonon decay [70]. Dephasing of the coupled plasmon-phonon mode (L-) oscillation has a major contribution due to carrier-carrier (electron-electron and electron-hole) scattering. In Raman scattering experiments it was observed that the decay rate of the coupled-plasmon phonon mode increases linearly with electron density [13]. Moreover within the observed depth due to slow drift and diffusion of heavier holes compared to the light electrons, there are more holes present near surface even after 100 fs [68]. A high density hole plasma has a higher scattering rate than a comparable density electron plasma [71], which is a major contribution to the plasmon decay in the case of our measurements with 400 nm pump and probe light. With higher excited carrier density, higher energy loss rate has been calculated [72]. Faster decay of the plasmon coupled mode has been observed when more photocarriers are present even when the total carrier density (photoexcited and majority carriers) remains same. This has been attributed to higher hole-phonon scattering in case of an n-doped sample [73]. Similar behavior of the decay time of the coupled mode was observed in surface second harmonic experiments at a carrier density range similar to our experiment [74]. In that study the claim was that the fast decay of the hole-phonon coupled mode was due to higher momentum scattering rate of a hole plasma compared to an equivalent density electron plasma. Thus, we conclude in our case also the carrier-carrier scattering, particularly scattering processes involving heavy particles e.g. holes plays a major role in fast decay of the plasmon-phonon coupled mode. At even higher carrier densities the coupled plasmon-phonon (L-) mode decay time constant saturates at around 0.45 ps. Higher carrier density most likely screens the Coulomb interaction between carriers resulting in saturation of the hole-hole scattering contribution to decay times of the coupled plasmon-phonon mode [75].

The bare LO phonon mode has a longer decay time constant than the coupled mode, which is extracted by fitting another exponentially damped harmonic oscillator to the oscillatory signal for time delays τ>2 ps. Like the bare LO phonon frequency, the decay time of this mode seems to be independent of the carrier density (Figure 3.5). This decay time of bare LO oscillation is in the range of LO phonon decay times reported by various experimental studies for different GaAs samples [33, 70]. The independence of the bare LO phonon decay time on carrier density indicates that the phonon decay occurs primarily through a phonon-phonon anharmonic scattering process involving the acoustic phonons [33].

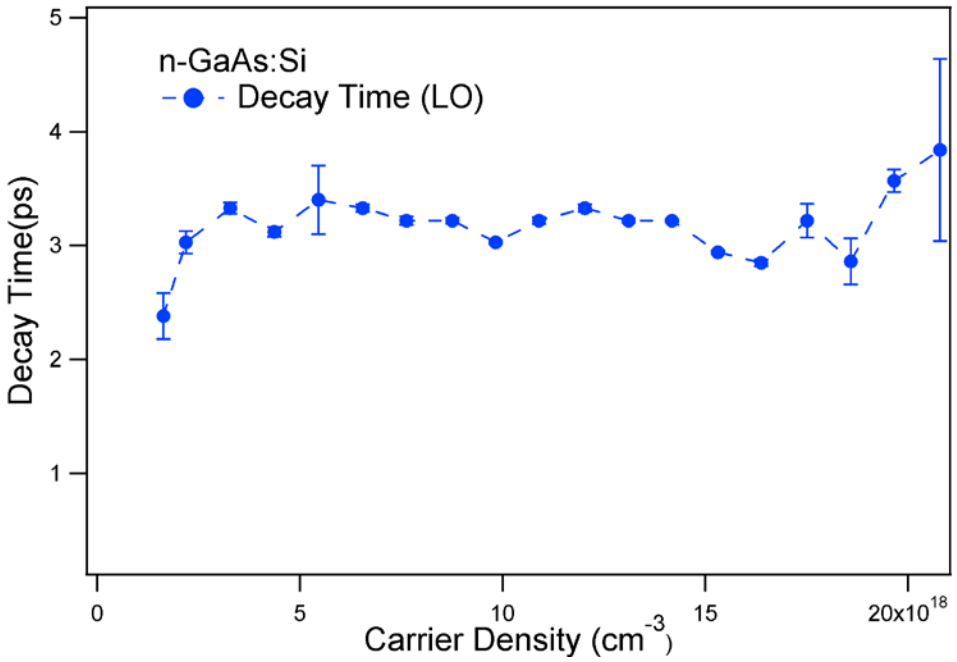

Figure 3.5 LO phonon decay time with increasing carrier density.

3.5 FREQUENCY RESPONSE: PLASMON-PHONON COUPLED MODE

In this section we look at the frequency response of the plasmon-phonon coupled mode and the LO phonon mode determined by FT analysis of the reflectivity signal at various carrier density

levels and compare that with calculated frequencies. The FT analysis is performed for the entire time record, so any time dependent frequency shifts of the oscillatory components are obscured. As described in Section 3.3, there are two major frequency components in the carrier density dependent reflectivity. The LO phonon frequency does not change with carrier density, but the L- frequency changes (Figure 3.2).

The bare LO phonon oscillation is only observable after the fast decay of the plasmon-phonon coupled mode (L-) on a time scale of ~2 ps (Figure 3.1). The peak attributed to L- red shifts towards the TO phonon limit with increasing carrier density (Figure 3.2). The frequency change of the L- mode with increasing carrier density is described with a dielectric response function for the coupled plasmon-phonon mode (Eq. 3.1) as detailed below.

The frequency dependent dielectric response function in the presence of plasma has contributions from both the lattice and plasma, in addition to the electronic excitations as represented by the high-frequency dielectric constant ε_∞ [61, 76, 77]:

$$\varepsilon(\omega) = \varepsilon_\infty \left[1 - \frac{\omega_{e,h}^2}{\omega^2 + i\gamma_{e,h}\omega} + \frac{\omega_{LO}^2 - \omega_{TO}^2}{\omega_{TO}^2 - i\gamma_{ph}\omega - \omega^2} \right]. \qquad (3.1)$$

Here, the parameters $\gamma_{e,h}$ and γ_{Ph} are the damping constants due to plasma and phonon damping respectively. ω_{LO} and ω_{TO} are the LO and TO phonon frequencies, respectively. The Plasma frequency is $\omega_{e,h} = \sqrt{ne^2 / m^* \varepsilon_0 \varepsilon_\infty}$. For the longitudinal response, the roots of this equation yield normal modes of oscillation at two hybrid frequencies, the so-called upper (L+) and lower (L-) coupled modes.

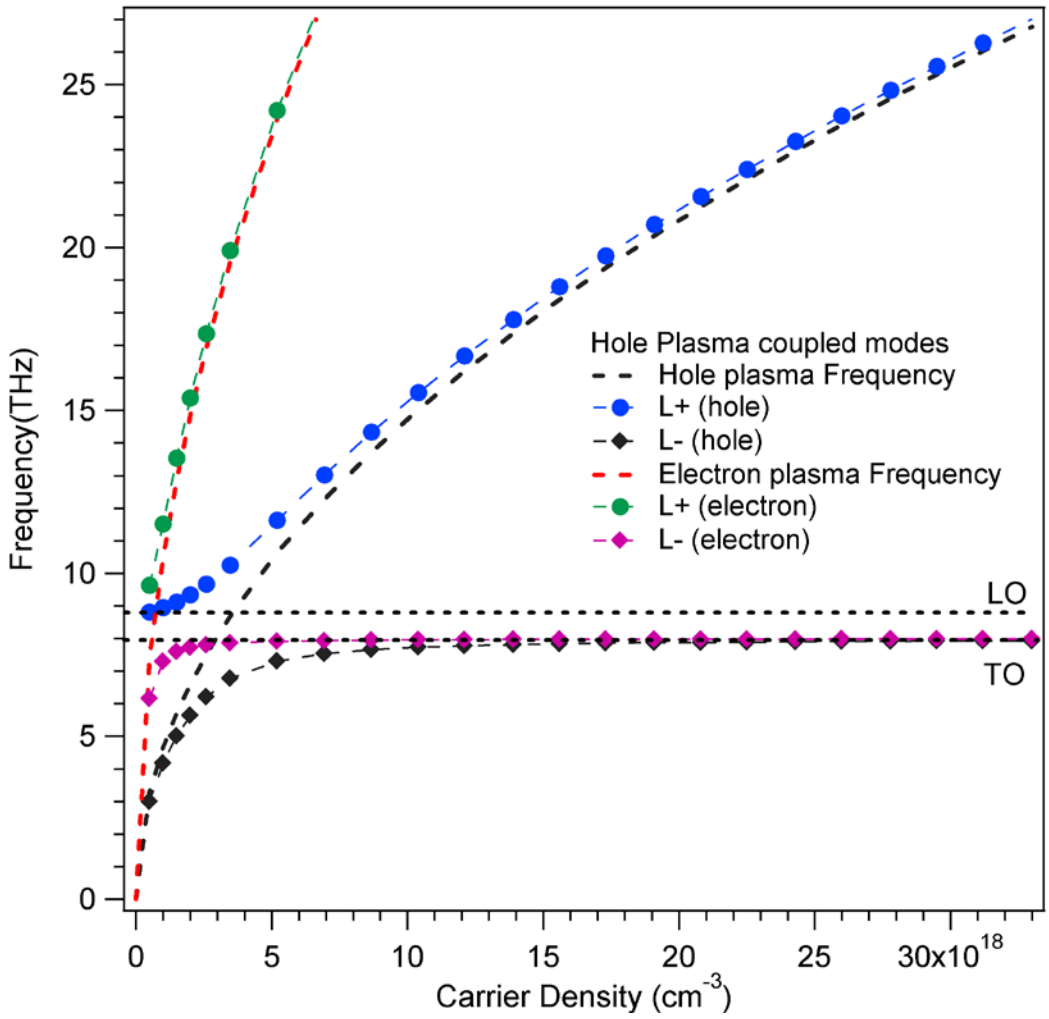

Figure 3.6 Calculated plasmon-phonon coupled modes without damping for Γ-valley electron plasma and hole plasma. Two horizontal dotted lines indicate the bare LO (8.7 THz) and TO (8.0 THz) phonon frequencies.

3.5.1 Undamped plasmon response

We consider two kinds of excited carriers contributing to the plasma, holes and Γ-valley electrons. We first calculate the plasmon-phonon coupled mode frequencies without damping. We set the damping constants to zero and solve Eq. 3.1 for the Γ-valley electron plasma and hole

plasma contributions to the dielectric constant separately. Figure 3.6 shows the calculated results for the plasmon-phonon coupled mode frequencies at different carrier densities for the Γ-valley electron plasma ($m_e^* = 0.067m_e$) and hole plasma (average hole mass $m_h^* = 0.34m_e$) [78]. The bare plasma frequencies are plotted with red (electron) and black (hole) dashed lines. We consider electron and hole carrier densities in the same range as we estimated to be present in our experiments. We observe that for undamped plasma there are clearly two distinct plasmon-phonon coupled modes. In both cases, the higher coupled mode (L+) appears just above the LO phonon frequency for low carrier density, and at higher densities it approaches the bare plasma frequency. This shows that the characteristics of L+ change from phonon like at low densities to plasmon like at high densities. The lower plasmon-phonon coupled mode (L-) frequency starts from near the bare plasma frequency at lower carrier density, and it asymptotically approaches the TO phonon frequency at higher carrier densities. The L- characteristics thus changes from plasmon like at low density to phonon like at high density [79]. The two branches of the coupled modes in the absence of damping are always above the LO phonon frequency or below TO phonon frequency. There are no modes with frequencies between the LO and TO phonon frequencies, as observed in our experiment, for undamped plasma. Due to difference in their carrier mass, the electron and hole plasma frequencies vary over different ranges. The masses determine the initial slope of the plasmon curves, and therefore the intersections between the noninteracting phonon and plasmon curves or the anticrossing region between the two coupled mode curves. For the same density the L+ frequency of the light carrier plasma is at a higher frequency than the heavy carrier plasma.

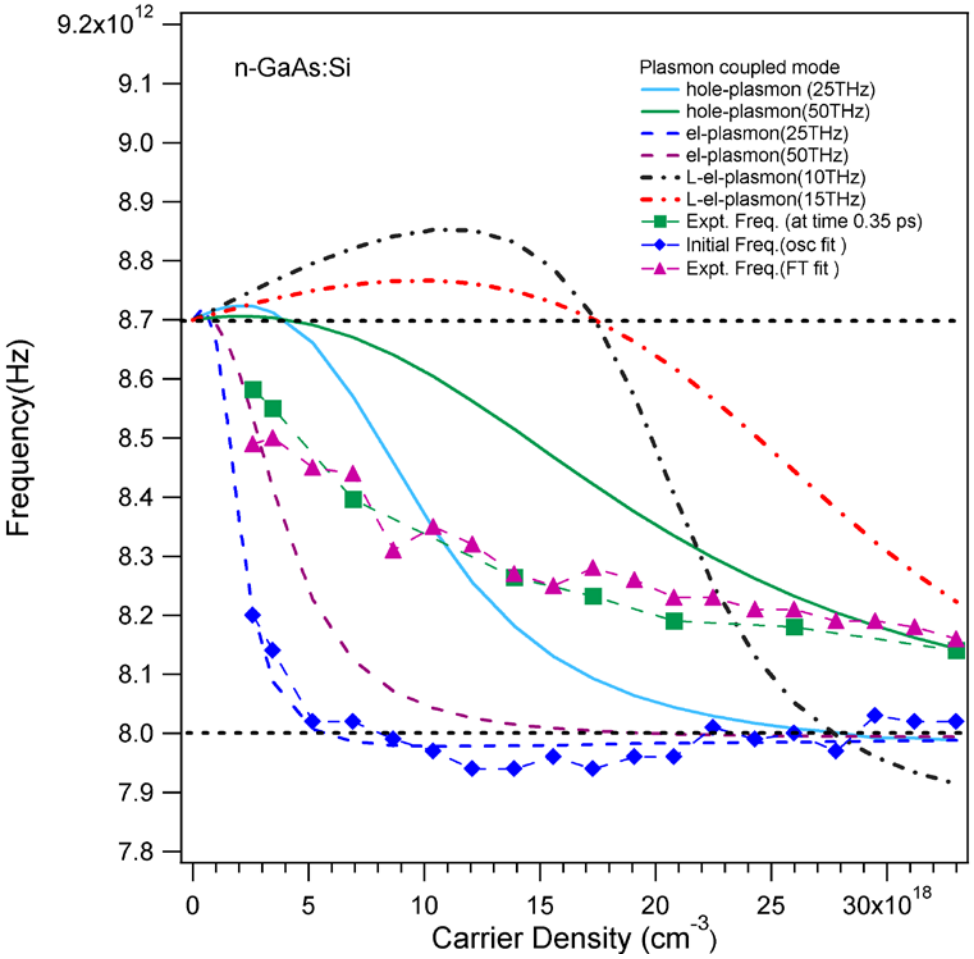

Figure 3.7 The calculated (lines) and experimental (lines and markers) for plasmon-phonon coupled mode frequencies at different photoexcitation densities.

3.5.2 Overdamped Plasmon Regime

To obtain the coupled mode frequencies in the high damping regime we solve Eq. 3.1 considering several, fixed plasmon damping parameters ($\gamma_{e,h}$), indicated for each plot (Figure 3.7) as a function of the excitation level, and a constant phonon damping (γ_{ph}) of 0.2 THz. For

the L- mode to tend from the LO to TO limit the plasmon has to be overdamped, as suggested by previous Raman scattering measurements on p-GaAs [80]. Because the damping rate is not known, we perform the calculations for several choices of $\gamma_{e,h}$. As in the undamped case, we consider either the electron plasma or the hole plasma and calculate the plasmon coupled mode frequencies due to only one kind of carrier. Theoretical values of the L- frequencies are plotted (lines in Figure 3.7) as a function of the carrier density for several damping parameters. We see very different responses of the electron and hole plasma coupled modes, which is not a surprise as their effective masses are quite different [$m_e^* = 0.067m_e$ (Γ valley), $m_{e,L}^* = 1.47m_e$ (L valley) [81] and $m_h^* = 0.45m_e$ for HH [82]].

The experimental values of frequency of the L- peak are obtained by fitting the FT spectra using the same method as described earlier in Section 3.4. This frequency is an average value of the L- frequency over the whole time delay. But the main contribution comes from the time window 0.2-2 ps. Beyond ~2 ps the L- mode has mostly decayed. To obtain information on the time dependence of the L- mode frequency, the time domain fitting is performed on the oscillatory component of the reflectivity data (Figure 3.1) with an exponentially damped chirped harmonic oscillator. This makes it possible to determine the initial frequency of the oscillatory component. The L- frequency changes with time by an amount that is given by the value of the chirp. The time windowed FT analysis yields the frequency of the oscillation at particular time delays. The method of this analysis is described later in detail in Chapter 5 where we discuss time dependent frequency change. Here we obtain the frequency at 0.35 ps time delay and plot it in Figure 3.7 for various carrier densities.

In Figure 3.7 the markers show the experimental values of the frequency of the plasmon-phonon coupled mode (L-) obtained by different analysis techniques as described above. We

observe only one plasmon-phonon coupled mode in the experiments. The experimental frequencies corresponding to the coupled mode are always between LO (8.7 THz) and TO (8.0 THz) phonon frequency limits. This is contrary to the calculated coupled mode frequencies for the zero damping case (Section 3.5.1) and experimental observation of coupled mode frequencies above the LO and below TO phonon frequency limit with 800 nm excitation and probe [70, 83], which will be discussed in Chapter 4. Similar doped carrier concentration dependence of the L-frequency has been observed in Raman measurements of p-doped GaAs [78, 82, 84]. These studies concluded that the single mode behavior and the mode frequency between the LO and TO phonon frequencies is due to overdamping of the hole-phonon coupled mode. Similar frequency change of the coupled mode was also observed in surface second harmonic generation experiments in GaAs [74]. The conclusion in that case was similar, due to highly damped hole-phonon coupling the frequency changes between the LO and TO frequencies. Experimental values obtained from time domain fitting, which yields the frequencies near time zero, behave somewhat differently. This behavior will be explained later in this section.

Our experimental points over the relevant density range due to FT fitting and the frequency at 0.35 ps, do not match with any single theoretical plot corresponding to any one particular carrier type with a constant damping parameter. The experimental plot also does not match with any one theoretical curve with a constant damping. The experimental frequency change with carrier density shows a trend from a relatively lower damped hole-plasmon curve to a relatively higher damped hole-plasma curve with increasing carrier density. This clearly indicates that the plasmon damping is not constant and depends on the plasma density, but there is no independent way to determine the density dependence of the plasma damping. The calculated frequency of the Γ-valley electron plasma and L-valley electron plasma in Figure 3.7

is far from the observed trend of the average experimental values. Thus, we conclude that the L- mode frequency as a function of carrier density reflects mainly the hole plasma response with a damping rate that depends on the carrier density.

In Figure 3.7, the blue diamond markers represent the frequencies near time zero as extracted from time domain fitting of the oscillatory component of the signal. At small time delays, more photoexcited carriers are present within the observed depth. The density of plasma is high, which results in stronger dressing of phonons and lower L- frequency. This trend has also been observed in our time dependent frequency analysis as will be discussed in Chapter 5. At longer time delay, photocarriers drift and diffuse towards the bulk, but at different rates for electrons and holes. This results in a time dependent carrier density change and more holes present near the surface than electrons. At later times the phonon dressing becomes weaker and the coupled mode frequencies are higher.

3.6 DISCUSSION

We analyzed the carrier density dependent properties of the transient reflectivity in this chapter. We discussed the main characteristics of the transient anisotropic reflectivity and the corresponding FT spectra at various carrier density levels. The main feature of the time domain signal was a highly damped oscillation within 0.2-2 ps time delay followed by a weaker but long-lived oscillation at bare LO phonon frequency. The FT spectra contained two main features attributed to L- and LO phonon modes. The LO mode frequency does not change, but the L- frequency changes from near LO to near TO with increasing carrier density. Generally the L- frequency shift is from below TO (8.0 THz) to the TO limit with increasing carrier density [73].

In case of p-doped GaAs in Raman experiments [78, 82] and hole-coupled mode behavior in SSHG experiments [74] this ‘anomalous’ trend was observed. In our case, the frequency change of the L- mode was analyzed considering highly damped plasmon-phonon coupling with contribution from the hole plasma or electron plasma. It was concluded that the frequency change behavior of the L- mode is dominated by hole-phonon coupling with dynamic high damping.

The FT intensities were analyzed with carrier density at different carrier density regimes. The L- intensity increases with carrier density at two density regimes showing plasmon oscillation dominating the coupled mode behavior. The phonon peak intensity behavior was explained using a screening model of coherent phonon generation. It was observed that with increasing carrier density the screening of the depletion layer electric field first increases linearly showing linear peak intensity with carrier density. But it saturates with further increasing the carrier density showing that the screening of the depletion electric field is complete. As a result the coherent phonon generation is also saturated and the peak intensity does not increase with increasing carrier density. Linear increase of amplitude of the reflectivity signal was also observed in the case of GaAs with 800 nm excitation [56]. But both L- mode and LO mode amplitudes were sublinear in another similar study with 800 nm excitation though at lower carrier densities [69]. Here we distinctly observe two regimes of carrier density showing increasing screening effects with carrier density increase.

The decay times of the coupled mode and the bare LO phonon mode were also studied with changing carrier density. The coupled mode decay time behavior with carrier density was explained using carrier-carrier scattering. It was concluded that the carrier scattering processes involving holes makes the decay of the mode faster with increasing carrier density. At higher

carrier densities there might be a screening of the carrier-carrier interaction resulting in saturation of the decay time. The decay time of the L- mode and the saturation of the decay with increasing carrier density are in accordance with the observed trend in earlier experiments at lower carrier densities [70]. The LO phonon decay time is comparable to values reported by Raman scattering experiments [33] and did not show any systematic carrier density dependence. This was due to the anharmonic decay of the phonon through an acoustic multiphonon process which does not depend on carrier density.

4.0 SYMMETRY STUDIES OF COHERENT PHONON AND PLASMON DYNAMICS

4.1 INTRODUCTION

The physical processes which might contribute to the generation and detection of coherent phonons have specific symmetry properties. Similarly plasmon generation and detection processes can also depend on crystalline symmetry. In Chapter 2 several models were considered for coherent phonon generation in polar materials. In the phenomenological model, the coherent phonon generation process can have contributions from the Raman active processes and nonlinear polarization processes, in addition to contributions from screening due to instantaneous charge separation (Eq. 2.3 and 2.4) [48]. The non-linear polarization processes can have contributions from the second, third, and higher order non-linear optical processes (Eq. 2.4). Each of these processes has specific symmetry, which can be selected by exciting the sample along different crystalline directions using polarized pump light.

Likewise, the detection of coherent phonon and plasmon response of a material is performed by recording the change in transient reflectivity along a specific crystallographic direction. The change in dielectric properties has contributions from the Raman and electro-optic effects (Eq. 2.10) [54]. In terms of the nonlinear optical susceptibilities, the form of relative reflectivity change is shown in Eq. 2.11. Symmetry of these contributions can be explored by the choice of polarization of the probe light. Optical processes with different symmetry and the

interference between them were considered in order to understand Raman scattering by the LO phonon [65, 85] and coupled plasmon-phonon modes [55] near the fundamental band gap of GaAs. Symmetry of the Raman tensor components for Raman active generation process of coherent phonons was also considered in bulk GaN of wurtzite structure [86].

In this chapter we study these polarization selective generation and detection of coherent phonons and plasmons. Studying pump and probe polarization dependent properties of the transient reflectivity response can shed light on which of these processes are responsible for generation and detection of coherent optical phonons and plasmons, what is their magnitude, and how they might interfere with each other. We extract the amplitudes, frequencies and decay rates, and study their changes with the pump and probe polarization directions.

4.2 SYMMETRY DEPENDENCE OF GENERATION AND DETECTION OF COHERENT PHONON AND PLASMON

4.2.1 Symmetry of generation process

The symmetry of generation of coherent phonons will depend on the symmetry of the physical processes contributing to the generation term (Eq. 2.3 and 2.4). The scattering amplitude of a Raman process is proportional to the tensor product $\hat{e}_i \cdot \vec{\vec{R}} \cdot \hat{e}_s$, where $\hat{e}_i$ is the polarization vector of the incident light and $\hat{e}_s$ is that of the scattered light, and $\vec{\vec{R}}$ is the Raman tensor. For GaAs (Zinc Blende semiconductor) the zone center optical phonons have the Γ_{15} symmetry. For an optical phonon polarized along the longitudinal direction ([100] or x direction for our case; we

define [010] as y and [001] as z) the Deformation Potential (DP) Raman tensor has only two nonzero components (Eq. 2.12)[61]. The coherent phonon amplitude generated by a DP mediated process involving the Γ_{15} symmetry tensor should then be anisotropic with respect to the pump pulse polarization. There can also be a Fröhlich interaction mediated Γ_1 symmetry component to the Raman tensor (Eq. 2.15), which is isotropic [55]. Nonlinear (NL) polarizations which are determined by NL optical susceptibilities can also contribute to the generation process (Eq. 2.3 and 2.4) with specific symmetry selection rules as described by their tensor forms (Eq. 2.13 and Eq. 2.14).

The third term of Eq. (2.4) signifies transient screening of the depletion layer electric field. Immediately after the photoexcitation (fs timescale) there is a polarization of electrons and holes due to charge separation due to the electric field in the depletion layer. This generates a longitudinal polarization in the opposite direction of the depletion layer electric field. The carrier-induced polarization depends on the photoexcited carrier density only, and is independent of the pump polarization direction. The screening model of phonon generation is described in terms of these effects (Section 2.4.2). This screening mechanism is the dominant mechanism for the excitation of the coherent LO phonons and plasmons in GaAs. The screening of the static depletion field releases the built up stress and triggers the collective oscillations of ions in the depletion layer of GaAs crystal.

Coherent plasmons are generated by the instantaneous acceleration of photoexcited carriers due to the depletion layer electric field along the longitudinal direction and the subsequent interaction with the lattice ions [43, 87]. The frequency of the plasma is determined by the density and mass of the carrier, but not on the direction of the excitation. Pump

polarization dependent experiments can shed light on the details of the symmetry of the generation process of the coherent phonon and plasmon.

The generation of both coherent phonons and plasmons depend solely on the electric field along the longitudinal direction [54]. By contrast the generation of coherent phonons in Si depends strongly on the polarization of pump since it is due to deformation potential interaction. A symmetric or asymmetric force can be exerted on the crystal by exciting the crystal along all four Si-Si bonds or two out of four bonds respectively resulting in symmetric or asymmetric phonon modes [8].

4.2.2 Detection Symmetry

Probe polarization dependent experiments can tell us about the symmetry properties of the processes that modulate the optical properties of GaAs crystal, and therefore affect the detected signal. The optical processes responsible for detection of coherent phonon and plasmon oscillation can be broadly divided into the anisotropic and isotropic contributions. The general forms of the Raman tensor and their symmetry properties have been discussed in Section 2.5 (Eq. 2.12 and Eq. 2.15).

The detection of the coherent oscillations is performed by recording the change in reflectivity, which has contributions from these mechanisms and also from the photoinduced electric field dependent change in reflectivity due to electro-optic effect (Eq. 2.10). The electro-optic (EO) contribution to the change in reflectivity has linear and nonlinear contributions (Eq. 2.11). The linear electro-optic effect is called the Pockels effect, and in crystals exhibiting linear EO effect coherent phonons can be detected via the associated longitudinal electric field. The modulation of the reflected field by the photoinduced longitudinal field is a second-order

nonlinear optical process ($\chi^{(2)}$). The $\chi^{(2)}$ process is anisotropic (Eq. 2.13) [48]. The phonon detection can also occur though the nonlinear electro-optic contribution, which involves the third-order optical nonlinearity $\chi^{(3)}$. The $\chi^{(3)}$ process is isotropic (Eq. 2.14). The electro optic effect is predominant in case of plasmon detection as in this case interaction between oscillating charges and the lattice ions is the main contributing factor to the change in reflectivity [88].

Both the isotropic and anisotropic contributions can contribute to the observed changes in reflectivity simultaneously (Eq. 2.11). The overall observation thus will depend on the relative contribution of these processes along a certain crystallographic direction. Depending on the direction of the observation these contributions can interfere with each other constructively or destructively due to change in phase of the anisotropic contribution resulting in change in the overall response [65, 88]. The optical processes contributing to the phonon and plasmon detection are summarized in Table 4.1 according to their symmetry properties.

Table 4.1 Symmetry of optical processes contributing to the coherent phonon and plasmon detection.

Symmetry	**Isotropic**	**Anisotropic**
Phonon	Fröhlich, Non-linear electro-optic ($\chi^{(3)}$)	Deformation Potential, Linear electro-optic ($\chi^{(2)}$)
Plasmon	Fröhlich, Non-linear electro-optic ($\chi^{(3)}$)	Linear electro-optic ($\chi^{(2)}$)

4.3 EXPERIMENTAL PROCEDURE

Pump and probe polarization dependent experiments are performed using the same n-doped [100] oriented GaAs (n_d= $2x10^{18}$ cm^{-3}) sample with the transient reflectivity measurement set-up as described in section 2.6. Linearly polarized pump and probe beams are focused to roughly 40 μm size spot on the sample and reflected probe beam is detected by a photodiode as a function of pump probe time delay. In these experiments the reflected light is not resolved into orthogonal polarization components. The signal thus contains both isotropic and anisotropic components of the reflectivity. The polarizations of the pump and probe pulses are individually controlled (Figure 2.7). The intensities of the pump and probe pulses are also kept fixed to capture the changes induced only due to the pump or probe orientation changes. Figure 4.1 shows a particular configuration of the pump probe polarization dependent experiment. Figure 4.2 describes the pump-probe polarization on the sample surface. The angle between pump and probe polarization is denoted by θ.

For pump polarization dependent experiments, the polarization of the probe light is kept fixed and the pump polarization is rotated with respect to it. For each pump orientation a transient reflectivity signal is recorded. In this experiment we can excite the crystal along a particular crystallographic direction and detect changes in the optical properties along another particular crystallographic direction selected by the probe polarization. We change the excitation directions by changing the pump polarization and explore symmetry of the generation processes of coherent phonon and plasmon.

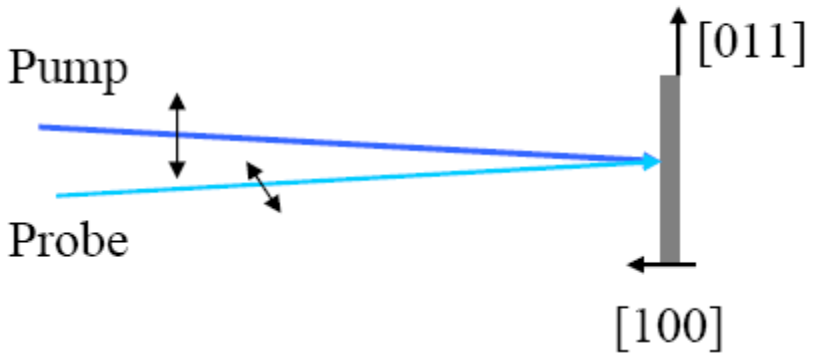

Figure 4.1 Experimental geometry for transient reflectivity measurement. Linearly polarized pump and probe pulses are incident on [100] oriented GaAs. The polarization of the pump or probe is rotated to perform polarization dependent experiments.

For probe polarization dependent experiments, the polarization of the pump light is kept fixed and the probe polarization is rotated with respect to that and a transient reflectivity signal is recorded for each of these probe orientations. We can thus excite along a particular crystallographic direction decided by the pump polarization and detect changes in optical properties at different crystallographic directions. We can observe the symmetry properties of the detection processes in this way.

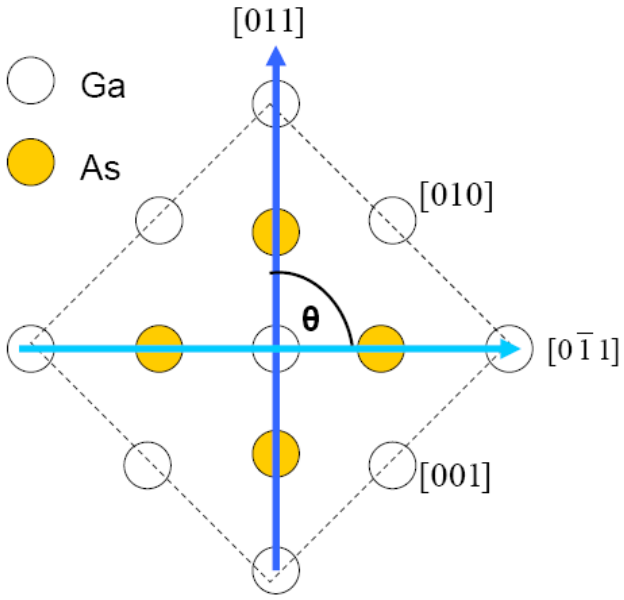

Figure 4.2 Pump (dark blue) and probe (light blue) polarization along specific crystallographic directions for [100] oriented GaAs; the angle θ between the pump and probe polarization is shown.

4.4 EXPERIMENTAL RESULTS

4.4.1 Pump polarization dependence

Pump polarization dependent experiments are performed to detect the symmetry properties of the generation of coherent phonon and plasmon. In these experiments the probe polarization is kept fixed along the [011] direction and the pump polarization is rotated with respect to it. For each orientation of the pump polarization, transient reflectivity is recorded as a function of pump-probe time delay. The oscillatory component of the pump polarization dependent reflectivity and corresponding FT spectra are shown in Figure 4.3. The angle between the pump polarization and the fixed probe polarization ([011] direction) is shown.

There are no substantial changes in the oscillatory components of the transient reflectivity and the FT spectra for different pump polarization directions. The reflectivity component consists of a large amplitude fast decaying oscillation, which decays on 1.5 ps timescale. Relatively low amplitude but long-lived oscillations are present beyond 1.5 ps time delay and still persist at the long delay limit of our time delay scan. The FT spectra also show no anisotropy. A broad L- peak at 8.4 THz and a sharp LO phonon peak at 8.7 THz are observed.

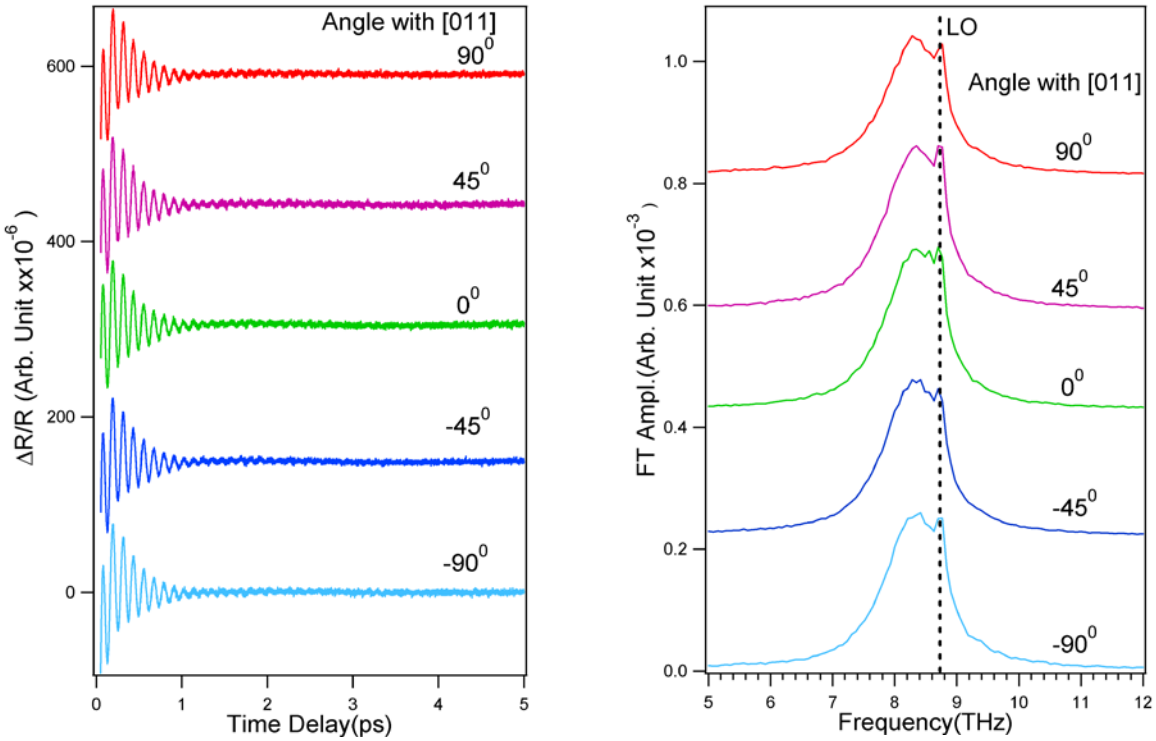

(a) (b)

Figure 4.3 Oscillatory components of reflectivity (a) and corresponding FT spectra (b) are shown for changing pump polarization and fixed probe polarization: the angle shown is between the pump polarization and the probe polarization ([011]) direction.

To obtain more precise information on the pump direction dependent amplitude, dephasing rates and frequency of the strong plasmon-phonon coupled modes (Time delay range, $\tau \sim$ 0-2 ps) and the bare LO phonon modes (Time delay range, $\tau >$ 2 ps) we performed time domain fitting of the oscillatory signals. Due to the complex nature of the signal a single or double exponentially damped harmonic oscillator functional form cannot be fitted to the oscillatory signal for the whole time delay range. The presence of the non-oscillatory component of the signal makes the time domain fitting even more difficult. We first extract the oscillatory components of the signal by subtracting the non-oscillatory part of the signal. In order to accomplish this, first the reflectivity signal is fitted with a polynomial function of degree 6, and the result is subtracted from the experimental data to remove the non-oscillatory background of the signal. The coherent electronic response, which is responsible for the sharp dip in the signal near time zero, is also excluded. Then a single damped harmonic oscillator is fitted to the fast decaying component (Time delay range, $\tau \sim$ 0-2 ps) of the signal, which yields decay rate, frequency and amplitude corresponding to the fast decaying L- mode. To extract information on the slowly decaying component of the signal at later time delays ($\tau >$2ps) a fitting function containing two damped harmonic oscillators, which includes already known parameters for the L- component is fitted to the whole signal. Amplitude, frequency and decay rate information for the LO mode are extracted in this fitting.

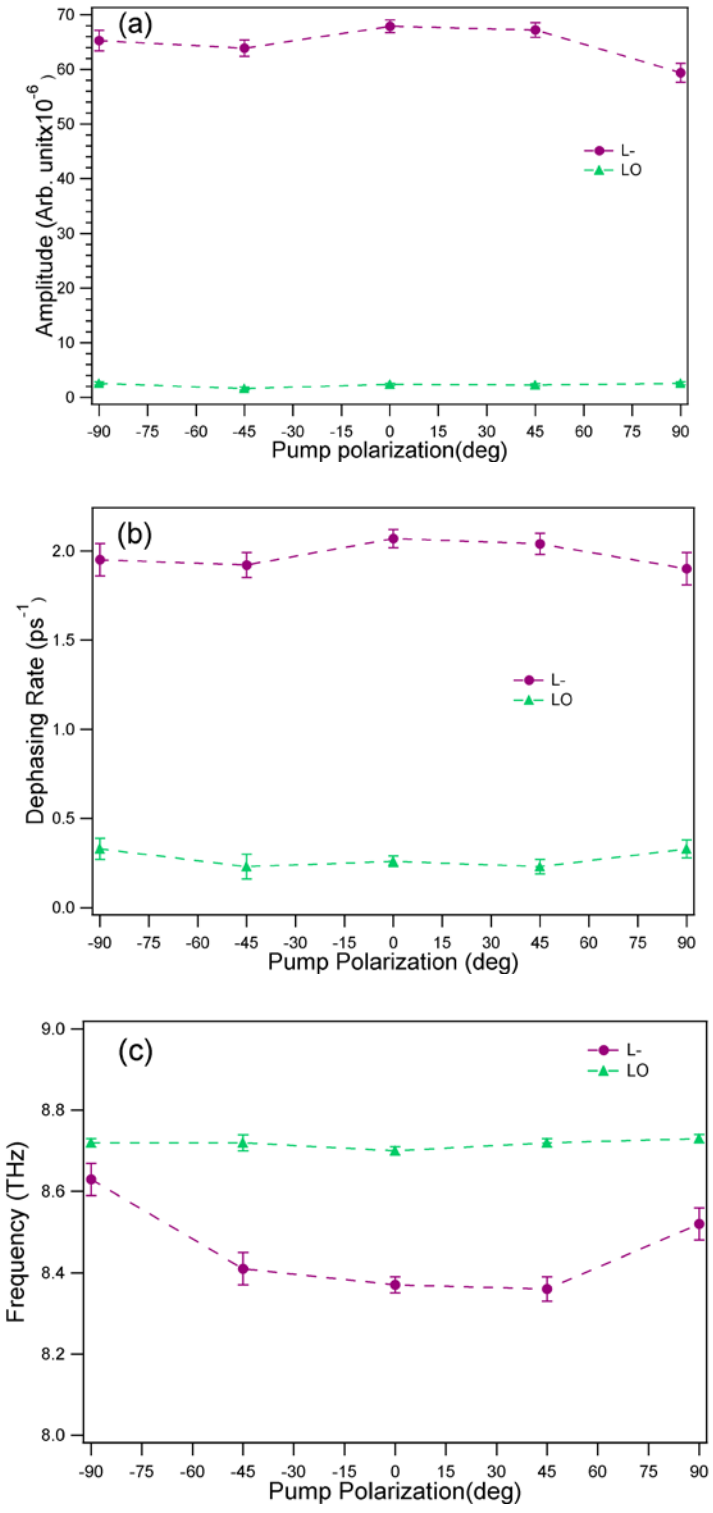

Figure 4.4 Pump polarization dependent (a) amplitude (b) dephasing rate and (c) Frequency of the coupled plasmon-phonon mode and the bare LO phonon are shown.

Figure 4.4 shows the amplitude, dephasing rate and frequency of the plasmon coupled L-mode and the bare LO phonon modes with change of the pump polarization relative to the [011] direction. With changing pump direction, the fit parameters for both L- and LO phonon component do not change substantially in a systematic manner. The small differences that can be observed are most likely introduced by very small changes in the pump-probe beam overlap (alignment) associated with rotation of the pump polarizer.

From the results in Figs. 4.3 and 4.4, we can conclude that the generation process of coherent phonons and plasmons is independent of the polarization of the pump pulse. This is consistent with the generation mechanism for the coupled coherent phonon and plasmon modes of GaAs due to screening of the depletion layer electric field as described in Section 2.4.2. The anisotropic Raman process does not have significant contribution to the coherent phonon and plasmon generation.

4.4.2 Probe polarization dependence

Probe polarization dependent experiments are performed to explore the symmetry of the detection of the coherent plasmon and phonon modes of GaAs. In this experiment, the pump polarization is fixed to be along the [011] axis, as shown in Figure 4.2. The probe polarization is rotated from the [011] direction, which is defined as $\theta=0°$, and transient reflectivity scans are recorded for several orientation of the probe light. In Figure 4.5 the reflectivity signals are shown with respect to time delay between the pump and probe pulses for different angles between the pump and probe polarizations in increments of 45°. Each of the measured scans consist of four main components: (i) a near-instantaneous transient electronic response; (ii) followed by a fast decaying oscillatory coupled plasmon-phonon response; (iii) a long-lived oscillatory bare LO

phonon response; and (iv) a slow, non-oscillatory component of the signal, which is not present when the pump and probe polarizations are parallel to each other ($\theta=0^{\circ}$).

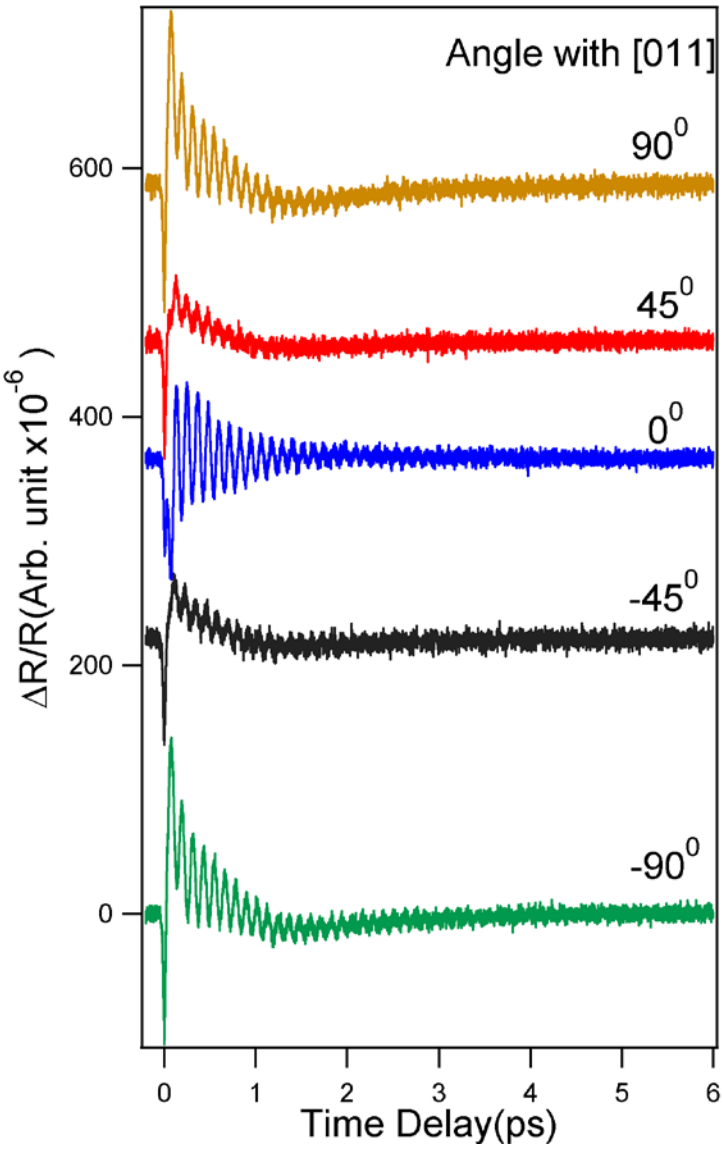

Figure 4.5 Time dependent reflectivity for changing probe polarization, for different angles between pump and probe polarizations. The pump polarization is along the [011] direction.

For $\theta=\pm45^{\circ}$ the oscillatory signal amplitude is the smallest, but it is not zero indicating the presence of an isotropic component in the transient reflectivity signal. For probe polarizations

along [011] ($\theta=0^{\circ}$) and [$0\bar{1}1$] ($\theta=\pm 90^{\circ}$) there is a fast decaying oscillatory component, which is the strong coupled plasmon-phonon mode. After this fast decay of the L- mode on a 1.5-2 ps timescale, there is a slowly decaying component of the signal. For probe polarization along ±45°, however, the fast and slow decay regimes are not clearly distinguishable.

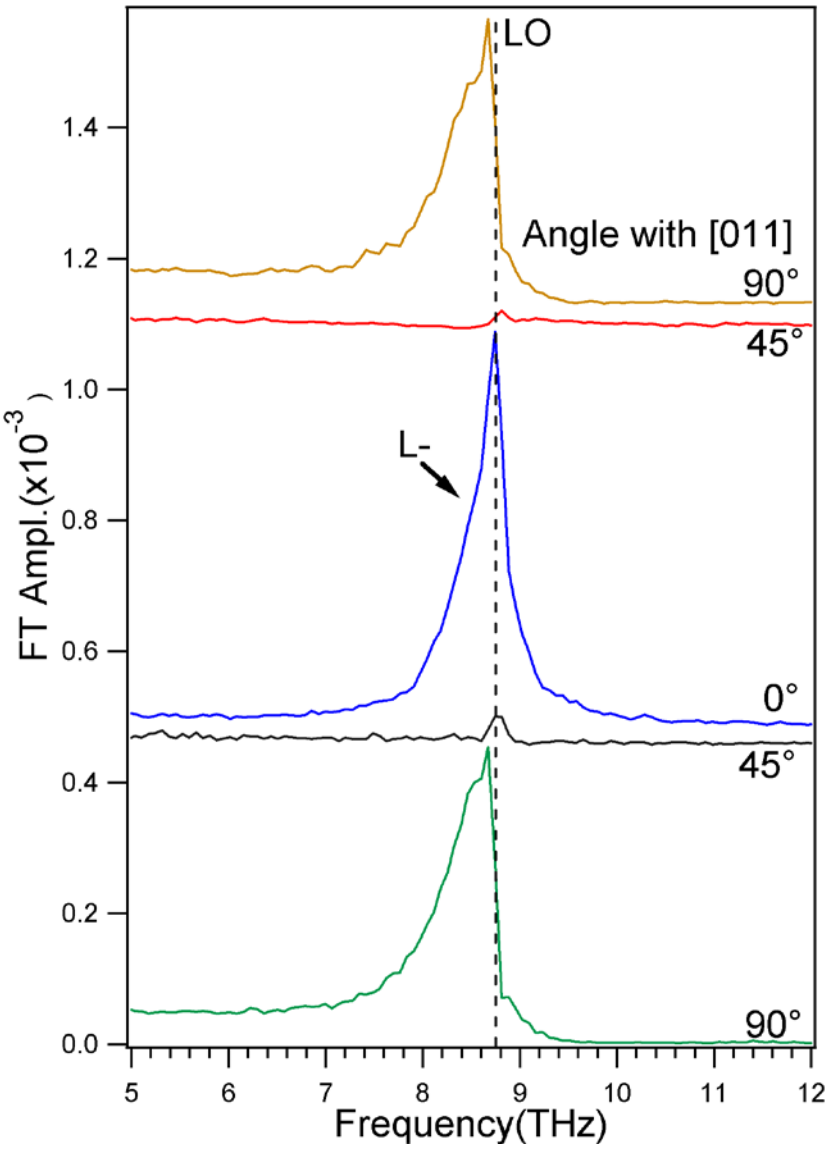

Figure 4.6 FT's of the time dependent reflectivity signals showing anisotropic optical response of both the bare phonon and plasmon-phonon coupled (L-) modes. Individual spectra are displaced in vertical direction for clarity.

Fourier Transform analysis of the reflectivity signals also reflects these differences, as shown in Figure 4.6. FT's of each time domain signal shows features attributed to the bare LO phonon and the L- modes. We detect the L- mode as evidenced by the broad peak between 8.0 THz (TO) and 8.75 THz (LO), for probe polarization along the [011] (θ=0°) and $[0\bar{1}1]$(θ=±90°) directions, whereas for probe polarization along [001] and [010] (θ=±45°) directions the L- like features are very weak. There is only a weak peak at the LO phonon frequency in these cases. The optical response is not even identical for the probe polarized along the [011] and $[0\bar{1}1]$ directions, which are ostensibly indistinguishable for a bulk crystal. For the probe along $[0\bar{1}1]$ (θ=±90°) there is a sharp cut-off in the FTs at the LO phonon frequency, but for the [011] (θ=0°) orientation, the cutoff is absent; rather we see a symmetric and very strong feature at the LO phonon frequency. This difference arises due to a difference in phase in plasmon oscillations along [011] and $[0\bar{1}1]$ direction, which can be discerned in Fig. 4.5.

In order to attain greater insight into the polarization direction dependence of the optical response (signal amplitudes, oscillation frequencies, and dephasing times), we fit the time domain signal using the same procedure as described in the preceding section on pump polarization dependent experiments. The fitting of the time domain data also allows us to extract information on the phase of different oscillation components. In Figure 4.7 the amplitudes of the L- and LO components of the signal are shown as a function of the angle between the pump and the probe polarizations. Both L- and LO amplitudes change with changing probe polarization in similar fashion but the L- amplitudes are almost an order of magnitude larger. The magnitude of the amplitude is higher for probe polarization along [011] (θ=0°) compared to $[0\bar{1}1]$ (θ=±90°), but the sign of the amplitude is opposite.

The amplitude of both the LO phonon and the plasmon coupled mode (L-) can be fitted with a fit function A+Bcos2θ, containing a constant term and an angle dependent term. The angle dependent term varies as ~cos2θ, where θ is the angle between the pump (along [011]) and probe polarization directions. In Figure 4.7 the two of the dashed lines are the fitted curves as indicated in the caption. The values of the isotropic and anisotropic amplitudes for L- are A= -1.1x10^{-5} and B= -6.5x10^{-5}. The corresponding values for LO phonon oscillation amplitudes are A= -2.85x10^{-6} and B= -7.43x10^{-6}. The anisotropic term for both L- and LO dominates over the isotropic term showing that the changes in the transient reflectivity are mainly anisotropic. Due to the small isotropic contributions, the amplitudes of the L- and LO components do not go to zero at ±45°, as would be expected for a purely anisotropic response, such as found in Si [8].

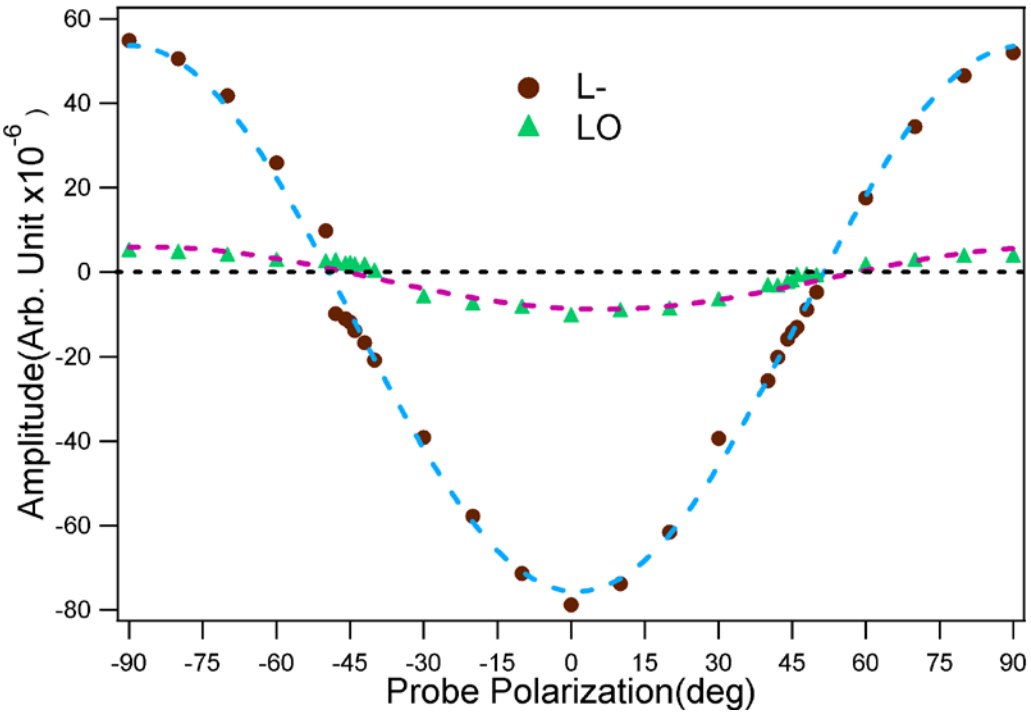

Figure 4.7 Amplitudes of LO and L- modes with changing probe polarization angle. Blue and red dashed curves are the best fittings.

Figure 4.8 shows the L- and LO mode frequencies as extracted from the fitting procedure. The L- frequency increases and tends towards the bare LO frequency when $\theta=\pm45^{\circ}$. Due to plasmon anisotropy, along $\theta=\pm45^{\circ}$ directions the L- response has the least contribution from the plasmon oscillation. So the observed frequency is near the bare LO frequency. Around $\theta=\pm90^{\circ}$ and 0° the plasmon amplitude is maximum resulting in maximum dressing of the phonon, and therefore, the minimum L- mode frequency. The bare LO frequency change is small ranging between 8.6-8.7 THz. Only at around $\pm45^{\circ}$, the frequency change is somewhat abrupt, which is probably due to relatively weak signal at that angle for time delays beyond 1.5 ps, and because the L- dephasing rate is decreased, making it difficult to separate the L- and LO contributions. The behavior of both L- and LO frequencies suggests that there is probably only one mode present for $\pm45^{\circ}$ probe polarization direction, i.e. plasmon contribution is the weakest and the response is dominated by the bare LO phonon.

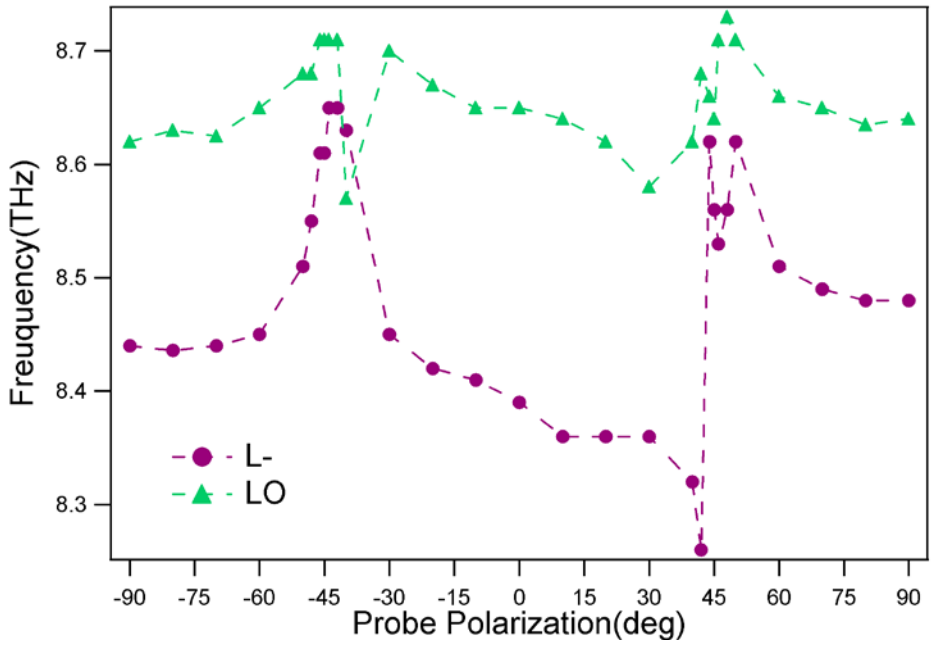

Figure 4.8 Frequencies of L- and bare LO modes with changing probe polarization angles.

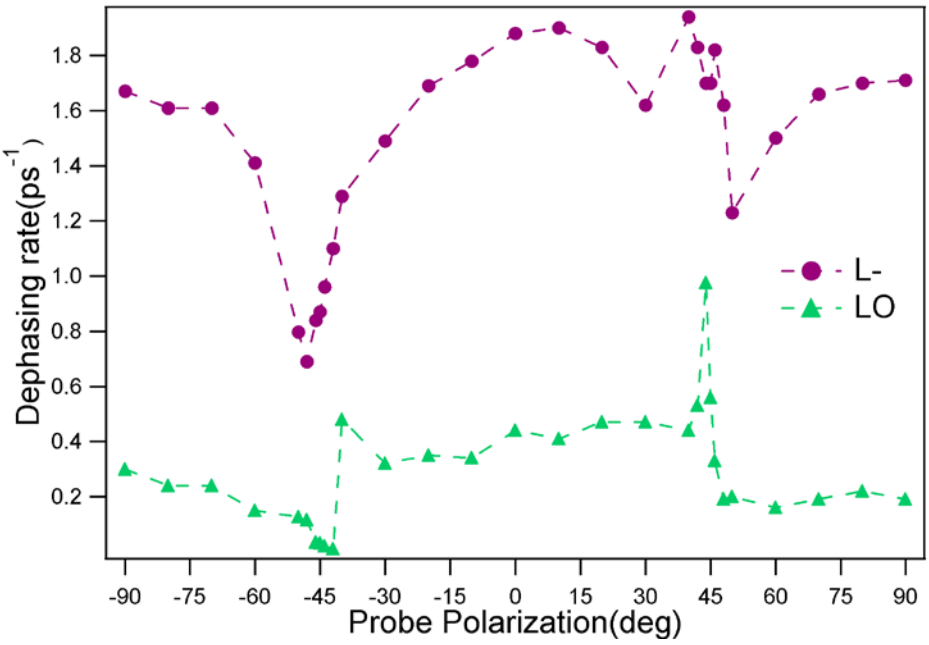

Figure 4.9 Dependence of dephasing rates of L- and bare LO modes on the probe polarization angle.

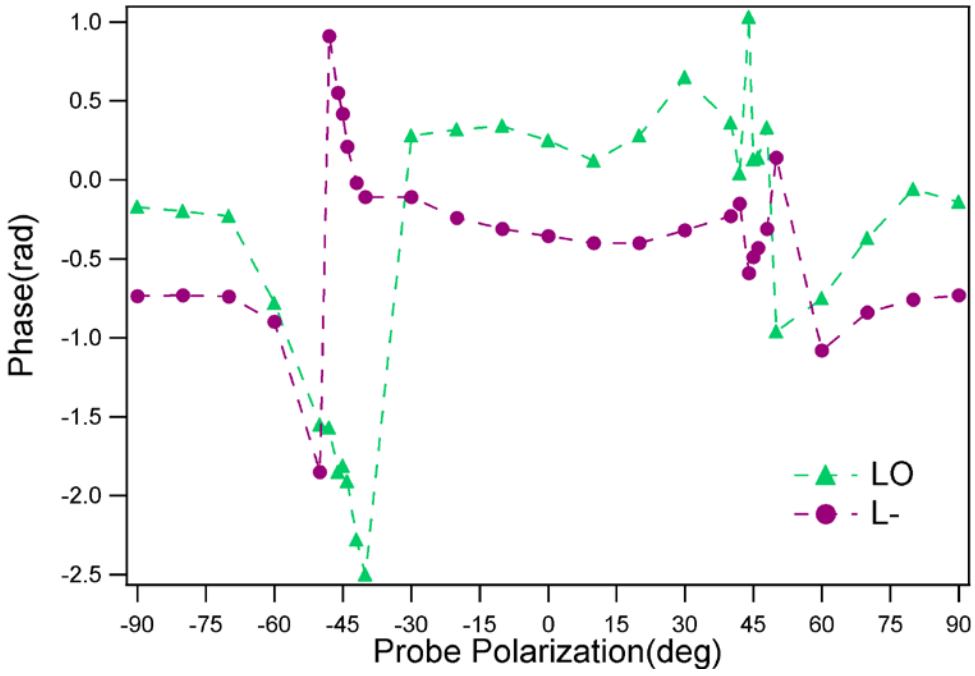

Figure 4.10 Dependence of the fitting extracted phase with changing probe polarization direction.

The relative strength of the L- and bare LO phonon components along different crystallographic directions can also be discerned in their respective decay rates (Figure 4.9). The L- mode decay is consistently faster than the bare LO phonon mode. For probe polarization of $\pm 90^{\circ}$ and 0°, the decay rate of L- is higher due to a strong plasmon contribution at those probe orientations. But near ±45° probe polarization directions the decay rates are lower and tend to the bare LO phonon decay rate. This behavior of L- is quite similar to the frequency change behavior at around $\pm 45^{\circ}$ probe orientation and indicates the tendency of dominant LO mode contribution as the L- amplitude tends to zero.

The anisotropy of the L- detection can be visualized as two oscillations with different isotropic and anisotropic components, where the phase of the oscillation depends on the angle of observation. Along ±90° and 0° the plasmon oscillation is strongest, but the phase of the anisotropic contribution is reversed. The anisotropic part of the response interfere constructively or destructively along 0° or 90° probe polarization angles with the angle independent contribution. The strong plasma components interact with the phonon oscillations and dress the phonons to generate the lower frequency L- mode with high dephasing rates. Due to the phase difference between the isotropic and anisotropic contributions this interaction is not identical along these two directions, resulting in small differences in the frequencies and dephasing rates at ±90° and 0°. Along ±45°, due to the absence of the anisotropic component of the plasma, the very weak isotropic plasma contribution dresses the phonon weakly and results in frequencies of L- and dephasing rates of L- near the bare LO values.

The bare LO phonon decay rates change by a modest amount between 0.2-0.4 ps^{-1}. The decay rates are slightly higher between probe angles ±45° than between -90° and -45° and 45° and 90°. The phase of the LO oscillation changes sign between these regions and most likely is

responsible for changes in the decay rates. The anisotropic component of the oscillating phonon signal interferes with the isotropic component in opposite phase in these two probe polarization regimes resulting in small change in decay rates. Figure 4.10 shows the phase values as extracted from the fitting procedure for L- and LO oscillations for various orientations of the probe. For both the LO and L- cases there is a difference in phase of the oscillation for the probe orientations between $\pm 45^{\circ}$ and -90° and -45° and 45° and 90°.

4.5 DISCUSSION

4.5.1 Comparison with Red (800 nm) pump-probe experimental results

We compare our probe polarization dependent results at 400 nm with the experimental results obtained by our collaborator Dr. Kunie Ishioka, NIMS, Tsukuba, Japan for 800 nm pump-probe light. The experiments are performed in a similar setup as a function of the probe polarization for the fixed pump polarization on an n-doped GaAs sample. The photoexcitation and detection with 800 nm light is dominated by carriers at the Γ valley near the fundamental band gap. In Figure 4.11 an example of a transient reflectivity scan is shown. Here the pump polarization is along [011] and probe is along $[0\bar{1}1]$. Corresponding FT spectrum is shown in the inset.

To understand the probe polarization dependent behavior of the optical response amplitude, dephasing rate and frequencies are extracted by fitting trial functions to the oscillatory components of the reflectivity signal for various probe polarization angles. The fit function consists of two exponentially damped harmonic oscillators. In Figure 4.12 the extracted values of amplitudes, dephasing rates and frequencies are plotted for different probe orientations. These

are plotted with respect to the relative angle between the pump (along [011]) and probe polarizations. The angle dependent amplitude is again fitted with a A+Bcos2θ form. The change in the LO phonon amplitude is similar to what we observed at 400 nm, i.e. the LO phonon amplitude is mainly anisotropic with a small isotropic contribution.

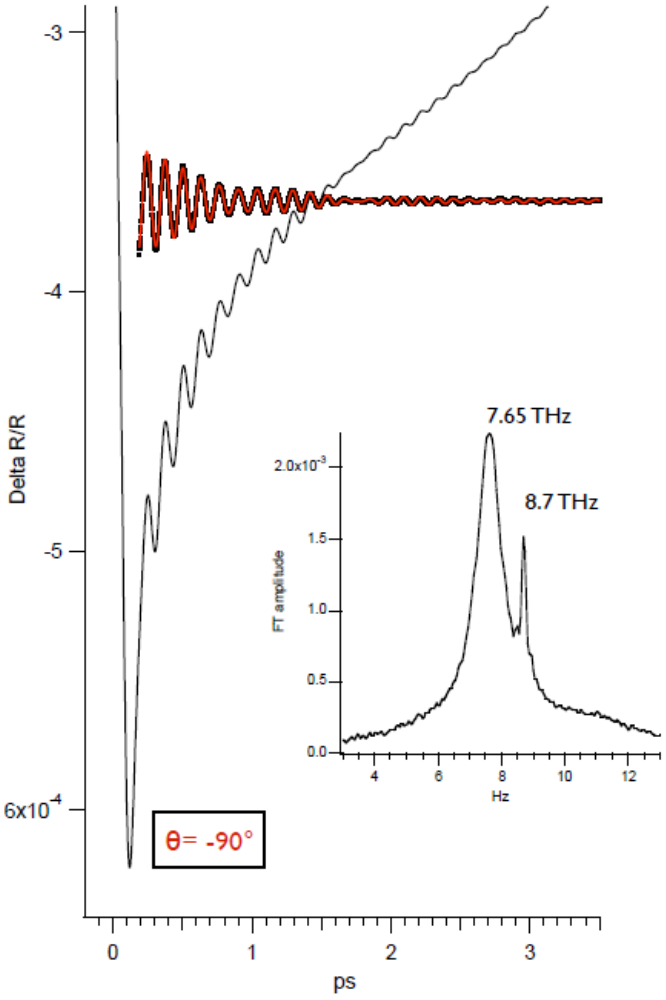

Figure 4.11 A transient reflectivity scan and corresponding oscillatory component of the reflectivity with the slowly varying background subtracted are shown. The inset shows the FT spectrum. (Courtesy Dr. Kunie Ishioka, NIMS, Tsukuba, Japan)

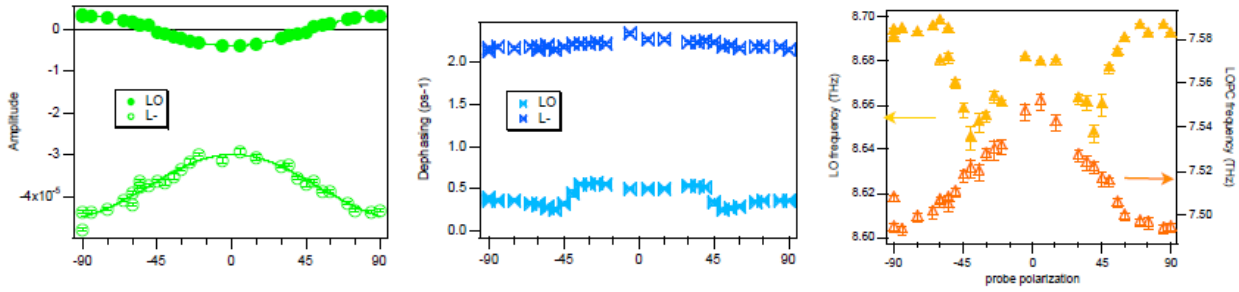

Figure 4.12 Probe polarization dependent response using 800 nm pump-probe light; (a) amplitude, (b) dephasing rate and (c) frequencies of the L- and LO components are shown. (Courtesy Dr. Kunie Ishioka, NIMS, Tsukuba, Japan)

By contrast, the L- amplitude shows a large isotropic term and a relatively smaller anisotropic term, resulting in mainly isotropic behavior. Due to the large isotropic component, the L- amplitude never becomes zero for any of the probe polarization angles. The extracted values of the fit parameters are summarized in Table 4.2. The isotropic L- response can be understood considering the fact that in case of GaAs the gradient of charge density is small. As the absorption coefficient is small the charge density profile is relatively flat in case of 800 nm light absorption compared to the case of 400 nm. Plasma density is almost constant in the region we are probing. Moreover, due to photoexcitation near Γ-valley, resonant character of Franz-Keldysh effect mediated $\chi^{(3)}$ response near fundamental band gap can play a role in making the L- response isotropic [60].

The dephasing rates of L- are constant for all the polarization directions at 2.2 ps^{-1}, which is consistent with the dominantly isotropic nature of the L- response. This is quite different than what we observe in the case of 400 nm experiments in which case the L- dephasing is predominantly anisotropic. The LO phonon dephasing rate changes by a small amount between 0.3 - 0.5 ps^{-1}, which has a similar value for the 400 nm experiment. The dephasing rate is slightly

higher between ±45° than between -90° and -45° and between 45° and 90° most likely due to a phase difference of LO phonon oscillation between these two regions.

Table 4.2 Fitting extracted values of the isotropic and anisotropic amplitudes for 800 nm and 400 nm experiments.

Pump/probe wavelength	Mode	A (isotropic)	B (anisotropic)
800 nm	LO	-5.1e-7	-3.49e-6
	L-	-3.41e-5	6.18e-6
400 nm	LO	-2.85e-6	-7.43e-6
	L-	-1.1e-5	-6.5e-5

The LO phonon frequency changes between 8.65-8.7 THz with values near 8.7 THz for polarization angles of θ=±90°and 0°. This behavior is similar to what we have observed in the case of the 400 nm experiment. The striking difference between the two experiments is in the frequency of the L- mode, which is around 7.5 THz and changes by a very small amount (0.04 THz). In comparison, the L- frequency is between 8.4-8.65 THz in the case of 400 nm experiment. The frequency of the coupled mode below the TO phonon limit (8.0 THz) is explained by the 'normal' phonon like behavior of the plasmon-coupled hybrid mode (L-) as discussed in Chapter [70, 79]. For our 400 nm experiments only one coupled mode can be detected, with a frequency which always appears between the TO (8.0 THz) and LO (8.7 THz) limits. This 'anomalous' behavior of the plasmon-phonon coupled mode frequency was

explained in terms of strong and highly damped hole-phonon coupling. The probe color, which determines the probe depth, is a determining factor in the frequency dynamics of the coupled mode. Smaller probe depth of 400 nm light (15 nm) detects dynamics mainly in the hole-phonon coupling regime. The 800 nm light excites the sample over a 50 times larger depth (750 nm) [67] and probes over a depth of ~55 nm within which the carrier density does not change much as the density decreases exponentially as $e^{-\alpha z}$, where α is the absorption coefficient of the light. Thereby for 800 nm light the coupled plasmon-phonon response has contributions from both electron-phonon and hole-phonon coupling processes.

The dependence of the coupled mode frequency on probe color was also observed for two color pump probe experiments. With red (800 nm) pump and blue (400 nm) probe, the plasmon coupled mode frequency as extracted from the time domain fitting to the oscillatory component of the signal is also around 8.4 THz. Even if the excitation pulse is 800 nm, the coupled mode frequency solely depends on the probe color again emphasizing the importance of probe depth and in determining the observed plasmon-phonon coupled mode behavior. 400 nm light only probes up to 15 nm and mainly detects hole-phonon dynamics as in the case of 400 nm pump/probe experiments.

In this Chapter, we discussed the coherent oscillation of the plasmon and phonon modes when excited and probed in symmetry selective generation and detection process using polarized pump and probe light. Pump polarization dependent excitation shows that the generation process is isotropic, i.e. the amplitude, frequency and dephasing rates are practically unchanged with changing of the pump polarization. Thus, we can conclude that the generation of coherent phonon and plasmon is dominated by screening of the depletion layer electric field due to ultrafast excitation of photocarriers, which is an isotropic process. It only depends on the carrier

density and not on the anisotropy of the excitation. By contrast, the generation process of coherent phonon in Si for a similar surface is direction dependent [8]. Depending on the polarization of the pump only two out of four tetrahedral Si-Si bonds can be excited, which translates to exciting 4 out of 8 equivalent L valleys, and accordingly the deformation potential mediated force on the crystal is anisotropic leading to symmetry selective phonon modes. In GaAs isotropic generation of coherent phonon thus shows that deformation potential mediated anisotropic generation is absent.

The probe polarization dependent measurements show anisotropy in how both the plasmon and phonon modulate the optical properties of GaAs. By analyzing the symmetry properties of the optical response as they relate to the phonon and plasmon oscillation along different crystal directions we can explain this anisotropy. The response of the GaAs, as manifested by change in reflectivity or change in the dielectric constant, can have contributions from their isotropic and anisotropic components (Eq. 2.10 and Eq. 2.11).

We probed the 2nd and 3rd order nonlinear optical contributions by measuring the transient reflectivity. The amplitudes of these interactions denoted by tensor elements $a_{NL}^{(2)}$ and $a_{NL}^{(3)}$ contribute to the amplitude of the whole signal and influence its behavior along different directions (Eq. 2.13 and 2.14). The anisotropic $\chi^{(2)}$ effect has the opposite phase along the 0° and 90° directions. Accordingly there is a constructive and destructive interference of $\chi^{(2)}$ with $\chi^{(3)}$ along [011] (θ=0°) and [0$\bar{1}$1] (θ=90°), respectively. The amplitudes for different crystallographic directions can then be estimated by considering the combined tensor of the form

$$\chi = \begin{pmatrix} a_{NL}^{(3)} & 0 & 0 \\ 0 & a_{NL}^{(3)} & a_{NL}^{(2)} \\ 0 & a_{NL}^{(2)} & a_{NL}^{(3)} \end{pmatrix} \tag{4.3}$$

and the polarization of the probe along different crystal directions as shown in Figure 4.2.

The proportionality factors of the amplitudes along different crystallographic directions are summarized in the Table 4.3. The measured isotropic and anisotropic amplitudes (Table 4.2) give an estimate of the values of the tensor elements $a_{NL}^{(2)}$ and $a_{NL}^{(3)}$.

Table 4.3 Proportionality factors of the amplitudes of the optical processes evaluated using the symmetry of χ tensors.

Probe Polarization along	Plasmon/Phonon
$[0\bar{1}1]$	$\left\|a_{NL}^{(3)} - a_{NL}^{(2)}\right\|^2$
[011]	$\left\|a_{NL}^{(3)} + a_{NL}^{(2)}\right\|^2$
[001]	$\left\|a_{NL}^{(3)}\right\|^2$
[010]	$\left\|a_{NL}^{(3)}\right\|^2$

The unique frequency and decay rate properties of L- can also be explained by considering strong plasmon anisotropy. The larger plasmon contribution along the [011] and $[0\bar{1}1]$ directions (θ=0°and ±90°) determines both the strong dephasing and lower frequencies of the L- mode in these directions. A higher plasmon contribution to the coupled plasmon-phonon response results in more dressing of the bare LO modes and makes these frequencies lower (near TO limit) and dephasing rates higher. Along ±45°, the absence of a strong plasmon contribution makes the properties of L- more like the bare LO mode. Therefore, the dephasing rate drops and the frequency tends towards the bare LO frequency.

In earlier experiments on GaAs with 2 eV photon energy and 50 fs pulse width [89] only the anisotropic component of the reflectivity was detected and was explained considering symmetry of only the linear electro-optic effect. The oscillations vanished along the [010] and

[001] directions where we observe relatively weak oscillations, mostly due to the phonon. The symmetry dependence of the LO phonon and plasmon coupled mode (L-) clearly indicates contributions from the isotropic and anisotropic optical processes with a higher anisotropic contribution for both LO phonon and plasmon coupled phonon response. Plasmon anisotropy is described in terms of symmetry properties of the electro-optic tensor. These contributions interfere in a constructive or destructive manner along different symmetry directions due to their changing phase which results in changes in the bare LO phonon and plasmon coupled mode (L-) amplitude.

5.0 TIME AND PHOTON ENERGY DEPENDENT PLASMON-PHONON RESPONSE

5.1 INTRODUCTION

Most of the scattering events of excited carriers in a semiconductor occur on an ultrafast timescale. Carrier-carrier scattering, carrier-phonon interaction and transport in the first few picoseconds after the optical excitation dominate the dynamics. To study these ultrafast optical processes, we need to detect these processes as they happen. With near 10 fs laser pulses we have the ability to time-resolve and detect these scattering processes by observing the resulting change in the optical properties of the sample with time.

In our experiments the phonon and plasmon oscillations are observed by detecting the change in reflectivity of GaAs wafers. We have already discussed carrier density dependent and symmetry dependent properties of the reflectivity in earlier chapters. The transient changes in the reflectivity signal are due to the combined plasmon and phonon responses and are dominated by the strong plasmon response in first the 2 ps after excitation. During this time interval, the frequency of the oscillation is changing. The frequency change is most likely dominated by the change in plasma density with time after excitation within the probing depth of the sample. By analyzing the time dependent frequency change we can understand the dynamical behavior of the carrier density within the probed region. The frequency of the oscillatory signal is nearly

constant after 2 ps time delay and is equal to the bare LO phonon frequency. We analyze the dynamics in time-frequency domain and observe changing amplitude even at later time delays when the dominant plasma-coupled mode has decayed. Another important spectroscopic property is the change in time dependent reflectivity with changing pump-probe photon energy. By tuning the wavelength of the laser pulse used in the experiments, we study this important property.

5.2 TIME DEPENDENT FREQUENCY RESPONSE

To determine time dependent frequencies, we analyze the reflectivity signal using time-windowed Fourier Transform. In this analysis we determine the time dependent frequency by multiplying the signal with a Gaussian time window with FWHM of 293 fs. Only a part of the time domain signal is extracted in this process centered at a particular time position defined by the peak position of the Gaussian time window. The FT analysis of this small part of the reflectivity signal shows the central oscillation frequency around this particular time point. By changing the position of the Gaussian time window and repeating the above process we determine the frequencies at various times. Because of the strong electronic component in the transient reflectivity response, the frequency of the initial oscillatory response is not well defined in the first ~200 fs after the photoexcitation. Beyond this time the time window captures more than two complete cycles of oscillations and the corresponding frequency shows a time dependence as the window position is scanned through time.

During the first 1.5 ps after excitation, the extracted frequencies of the oscillatory component of the signal change with increasing time delay in a way that depends on

photoexcitation carrier density. In Figure 5.1 the time delay dependent frequencies are plotted for different average photoinduced carrier densities, where averaging is done over the absorption depth. In the presence of free carriers or plasma, due to plasma oscillation, the lattice and plasma interact due to Coulomb interaction and coupled plasmon-phonon modes are formed (Chapter 2). Coupled plasmon-phonon modes are the hybrid oscillation modes in the material with two possible frequencies. These are the so called L+ and L- modes (Chapter 3). The frequency change of the bare LO phonon from its characteristic frequency due to the coupling with the plasma oscillation can be considered as dressing of the phonon with plasma. These dressed phonons oscillate at the hybrid frequencies.

For lower carrier densities, the frequency of the oscillation is near the bare LO phonon frequency. For smaller plasma densities the coupling of the phonon and plasma is not substantial, so the dressing of the coherent LO phonon gives rise to a small change in frequency. With increasing carrier density, the dressing of the phonon becomes stronger and as a result the coupled mode frequencies are reduced to near 8.0 THz. With time, the frequency evolves towards the bare LO phonon frequency for the first 1.5 ps and the frequency becomes LO phonon frequency at 1.5 ps time delay.

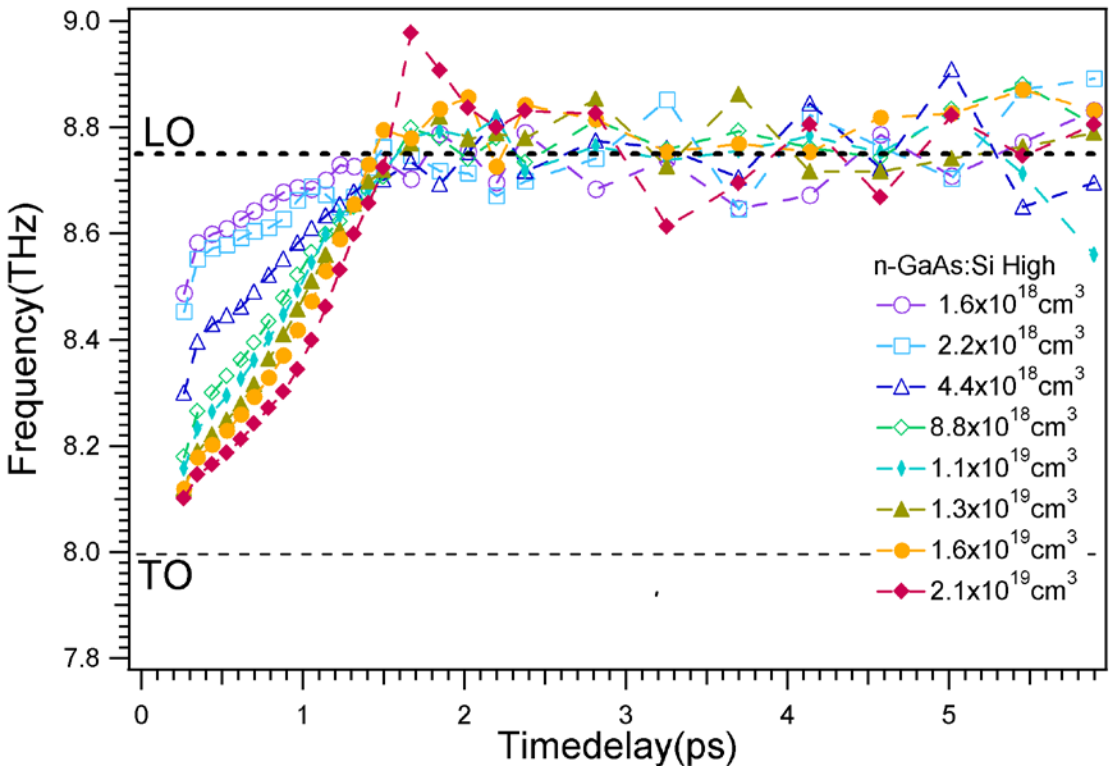

Figure 5.1 Time dependent frequency change at various carrier densities.

The bare LO phonons are dressed due to the presence of high-density plasma. Because of drift, diffusion, and dephasing of the plasma, the carrier density dependent plasma oscillation decays and the dressing of the LO phonon mode becomes ineffective. As we have seen earlier, the strong initial oscillation due to coupled plasmon-phonon mode decays within 1.5-2 ps with a decay time constant of 0.5-1 ps, the dressing of the phonon also becomes ineffective on the same time scale. Higher average photoexcitation density results in stronger phonon dressing and the corresponding coupled plasmon-phonon mode frequencies are significantly lowered to 8.2-8.5 THz range. This is in accordance with the change in frequency with increasing carrier density as discussed earlier (Figure 3.7). We have seen that with increasing carrier density the coupled mode frequency red-shifts from the LO phonon (8.7 THz) limit to the TO phonon (8.0 THz) limit. Here we observe that for small (<1 ps) time delay, increasing the photoexcitation density

shifts the coupled mode frequency to near the TO limit. With increasing delay time the frequency approaches LO frequency. This clearly indicates the decay in the number of photocarriers with time. The change in frequency with time and the dependence of the change on the carrier density clearly indicate that strong plasma oscillation dominates the dynamics. The frequencies indicate that the plasmon-phonon coupling is in the high damping regime as was described in Chapter 3. There we observed time integrated frequency change with increasing carrier density. In this Chapter we observe carrier density dependent frequency change of the plasmon coupled phonon mode with time.

After this frequency evolution in the first 1.5-2 ps time delay, the coherent oscillation frequency is equal to the bare LO phonon frequency at 8.7 THz. This asymptotic behavior of phonon frequency at time delays >1.5 ps is independent of the photoexcitation density. The convergence in the oscillation frequency after ~1.5 ps delay occurs at the transition of the time domain signal from being dominated by the L- mode to the longer lived LO phonon mode. The undressing of the plasmon-phonon coupled mode in the 1.5 ps time scale is governed by the decay of the plasma oscillation due to dephasing and also drift and diffusion related depopulation.

5.3 TIME-FREQUENCY DOMAIN PICTURE

Analyzing the reflectivity signal by looking at different frequency components at different times may reveal further information, which is not obvious in the time domain or time-windowed frequency analysis. In Figure 5.2 we have plotted the time windowed FT spectra in the time-frequency domain for the lowest and highest excitation densities. The height and the color code

of the three dimensional plot signify the strength of a particular frequency component at a particular time delay. The main peak corresponds to the coupled plasmon-phonon response which decays in a time scale of 1.5-2 ps. For lower excitation density (4 mw) the low frequency component gets significantly weak by 4 ps time delay. For higher excitation density this low frequency component does not decay even after a 6 ps time delay. The most striking feature is the beating like behavior at higher carrier density. After the initial decay of the strong plasmon-phonon coupled mode on a time scale of 1.5 -2 ps, a weak peak reappears and disappears several times at later time delays. These peak recurrences at 8.7 THz, the bare LO phonon frequency, get gradually weaker at later time delays. The long lived bare LO phonon oscillation shows this decay and revival.

Mode beating and associated amplitude collapse and revival is a common phenomenon in coupled plasmon-phonon dynamics as depicted in both theoretical [59] and experimental [70] studies with excitation near the fundamental band gap. Two classical oscillators with similar amplitudes and comparable but different frequencies can beat at their difference frequency. Here beating means the oscillation of the amplitude envelope which happens at the difference frequency of the oscillators. Collapse and revival is also associated with quantum beating, where a quantum process results in collapse and revival of the overall amplitude. For example a wavepacket might collapse and revive in an anharmonic potential. Quantum beating has been studied theoretically [90, 91] and experimentally [92]. However in our case there is a pump power dependence of the beating and it only appears at very high ($10^{20}cm^{-3}$) carrier densities. This suggests that it might be a beating between different spatial components of the coherent response within the excited volume representing different density regions of the plasma [59, 93].

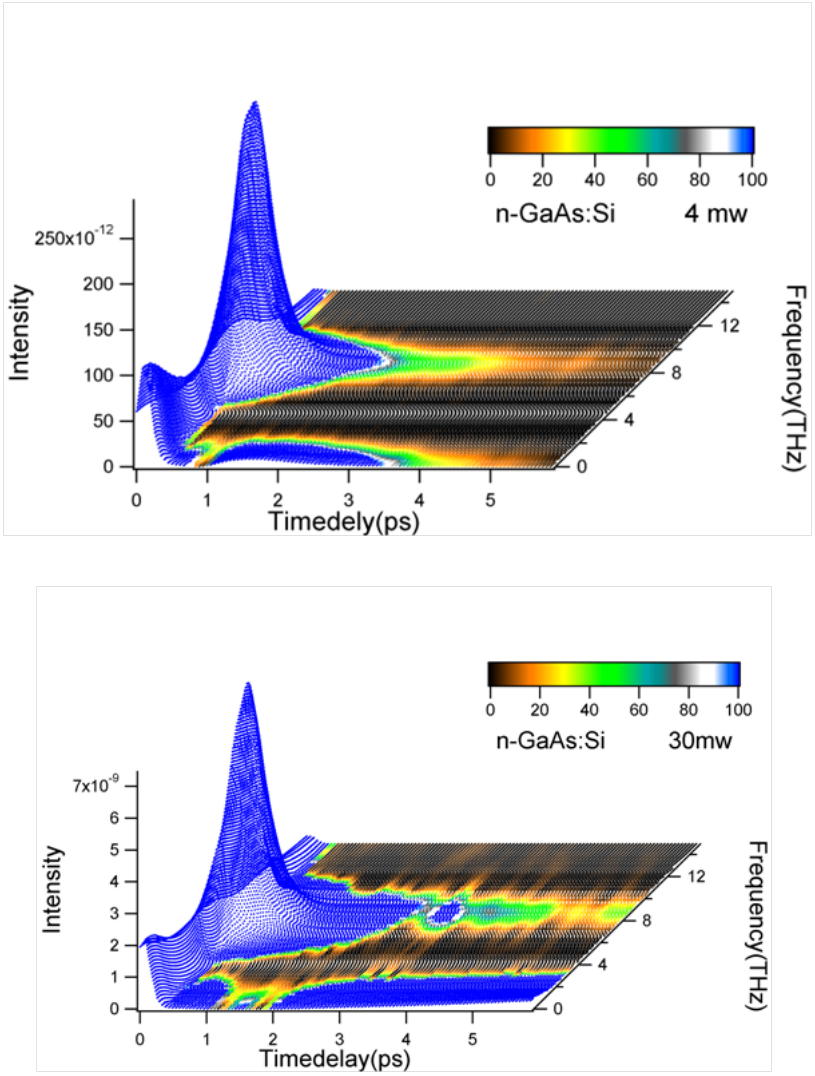

Figure 5.2 Time-Frequency dependent FT intensities at various pump intensities.

5.4 PHOTON ENERGY DEPENDENT RESPONSE

Application of an external electric field to a semiconductor leads to change in the absorption spectrum near the fundamental and subsidiary absorption edges (critical points). With sufficiently high electric field the real and imaginary parts of the dielectric constant show oscillatory behavior which can be detected in electro-reflectance [94] or electric field induced Raman scattering experiments [95].

The nonlinear effect of electric field on the dielectric property of a semiconductor is called the Franz-Keldysh (FK) effect [34, 61]. This effect may show resonance enhancement around the critical points, which has been observed at low temperature in electro-reflectance measurements [63]. Cho et al. [60] has observed enhancement of the amplitude of the isotropic component of the reflectivity in a transient reflectivity measurement near the fundamental band gap of GaAs at room temperature. They interpreted this observation as enhancement of the FK effect contribution to the transient reflectivity. The FK effect is the major contribution to the isotropic $\chi^{(3)}$ nonlinear optical response of the semiconductor.

In our experiments though the isotropic component of the response is relatively small (Chapter 4), it is still a significant contribution to the overall change in reflectivity. We can find out whether this isotropic reflectivity component has any resonant enhancement by changing the photon energy of the pump-probe light.

5.4.1 Experimental procedure

We explore the change in coherent phonon response with transient reflectivity measured along particular crystal directions with changing photon energy between the E_1 and $E_1+\Delta_1$ critical points (Figure 5.3). We use the same procedure as described in Chapter 2 to record the transient

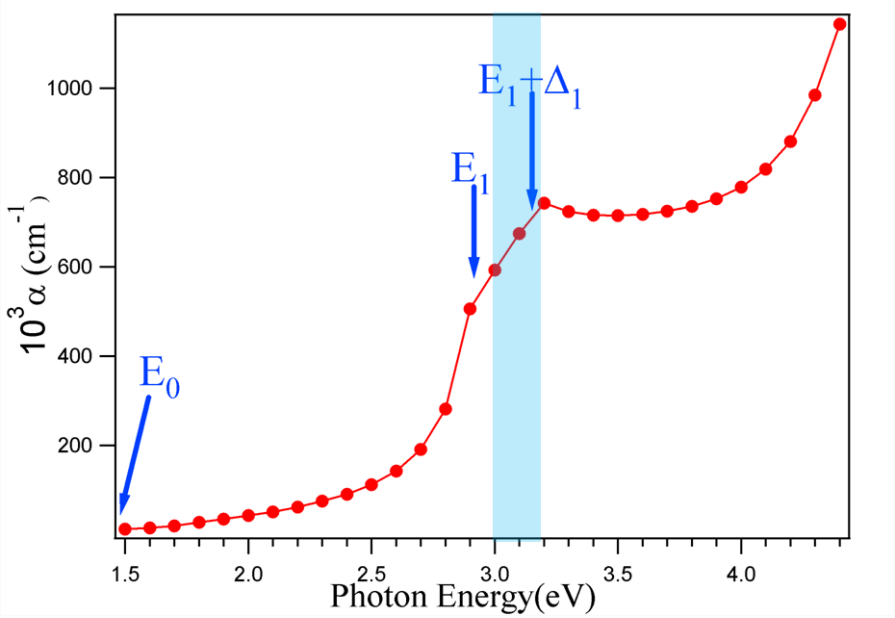

Figure 5.3 Absorption coefficient [67] of GaAs at various photon energies. The shaded area shows tunability of our laser.

reflectivity at different pump-probe wavelengths. We keep the average pump and probe powers unchanged at 15 mW and 2 mW for the experiment. To change the wavelength of the second harmonic of the Ti-Sapphire laser which we use to excite and probe, we change the phase matching angle of the BBO crystal by tilting the crystal (Section 2.6). Due to limitation in the tunability of the excitation laser source in this way, we are not able to go below or above the critical points. We can only tune in a small range (3.05 - 3.2 eV) of photon energies which starts above E_1 and increases up to the $E_1+\Delta_1$ critical point energies (Figure 5.3). We measure the

transient reflectivity corresponding to two orientations of the probe beam [011] and $[0\bar{1}1]$. The pump polarization is kept fixed along the [011] direction.

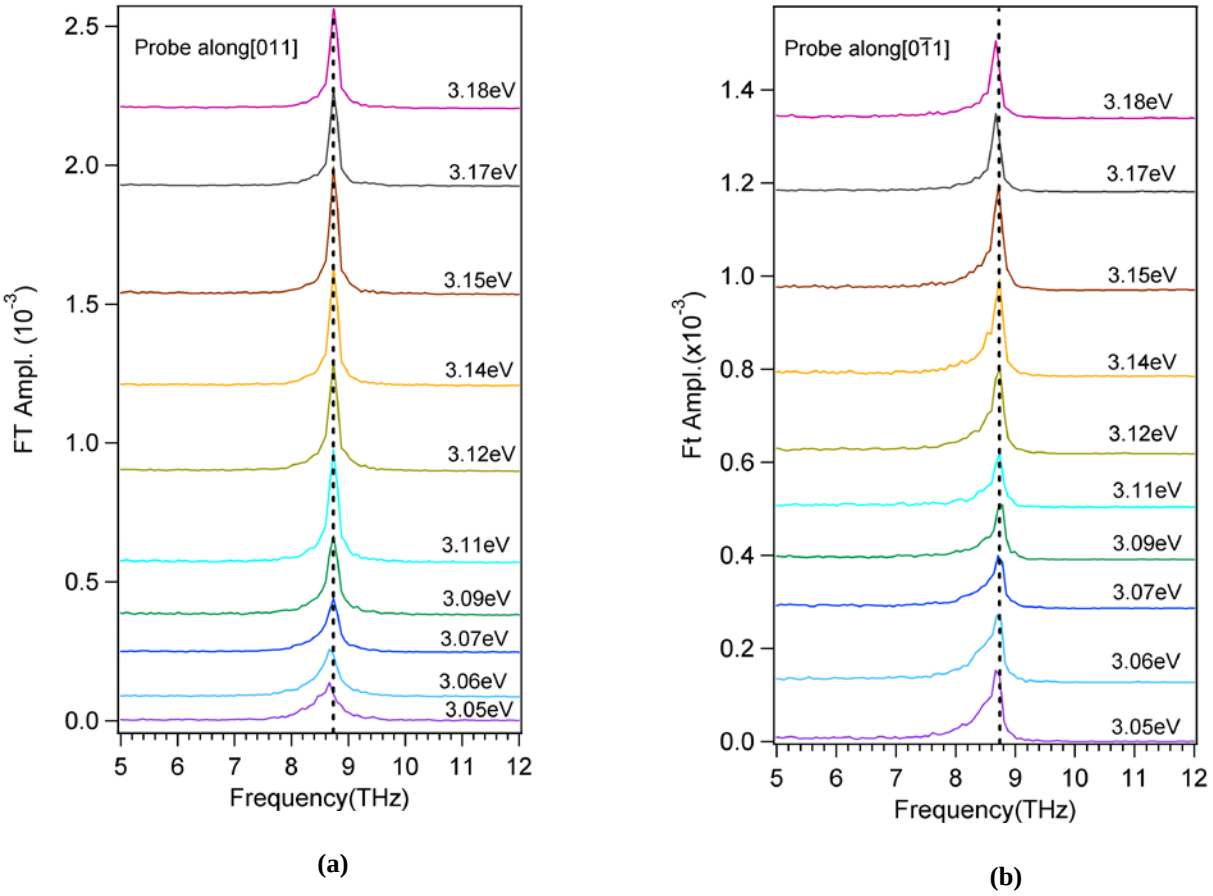

Figure 5.4 FT amplitude at various excitation photon energies when probe is along the (a) [011] and (b) $[0\bar{1}1]$ directions.

5.4.2 Experimental results

In Figure 5.4, FT's of the transient reflectivity measured along [011] and $[0\bar{1}1]$ crystal directions with changing photon energy are shown. The FT spectra are dominated by the LO phonon peak.

With increasing photon energy the peak gets narrower and the peak height increases. We subtract the transient reflectivity traces along the two directions as mentioned above for a particular excitation photon energy and extract the anisotropic component of the reflectivity. We perform FT analysis of the anisotropic reflectivity component. In Figure 5.5, the FT spectra of the anisotropic component of the reflectivity are shown with changing photon energy. The FT peak height corresponding to the LO phonon frequency changes with changing photon energy, but the frequency remains unchanged. At lower photon energies the peak is asymmetric due to the presence of a broader but weak plasmon coupled mode.

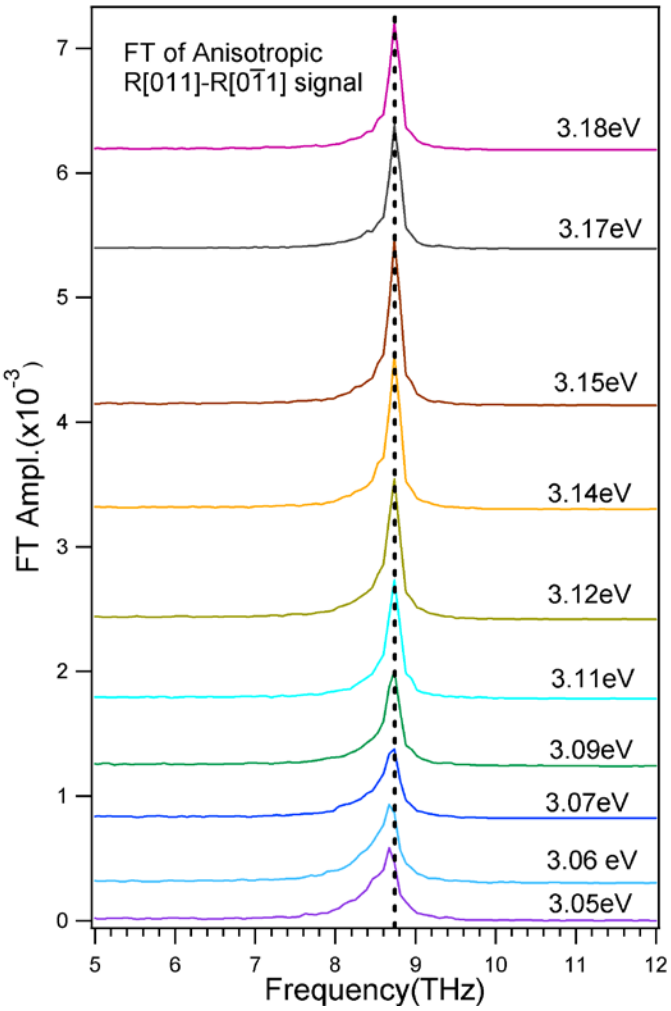

Figure 5.5 FT spectra corresponding to the anisotropic reflectivity at various excitation photon energies.

To understand the resonant property of the response along different crystallographic directions and the anisotropic component we fit the FT peaks using Lorentzian fitting functions. We plot the extracted FT heights for all three data sets as a function of photon energy in Figure 5.6. We observe the FT height corresponding to the response along [011] increases by a

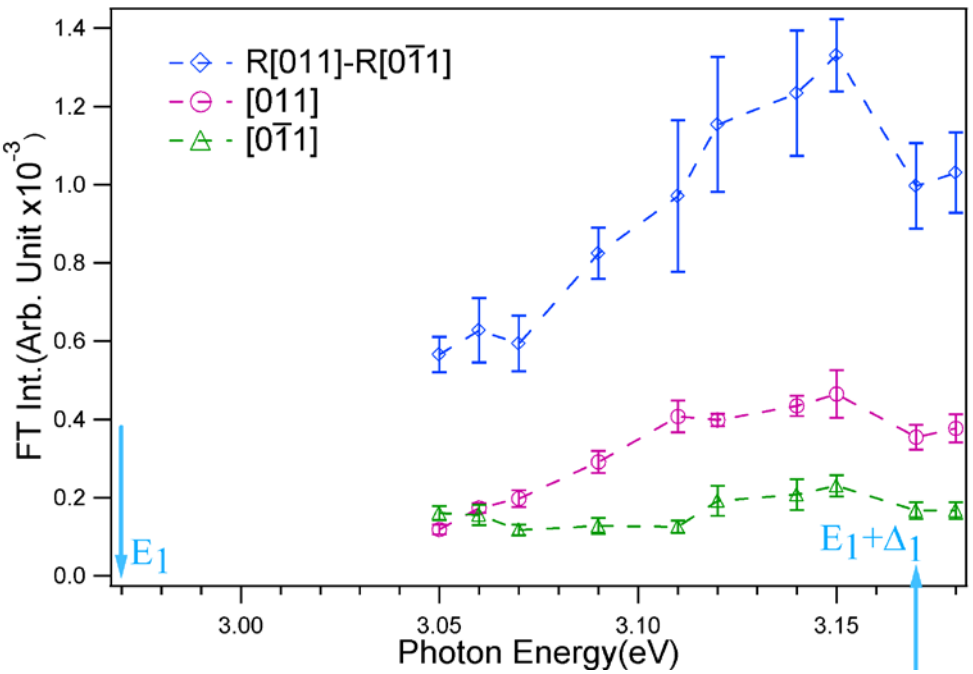

Figure 5.6 FT Intensities at various excitation photon energies: isotropic components along two crystal directions and the anisotropic component of the amplitude are shown. The blue arrows indicate the position of the critical points in the energy scale.

factor of 2 between 3.05 eV and 3.15 eV and is highest for 3.15 eV excitation photon energy. Between the same ranges of photon energy the response along [0$\bar{1}$1] does not change much. The anisotropic component of the response increases in peak intensity by a factor of 2.The response along a particular direction contains the isotropic part of the response ($\chi^{(3)}$ contribution) along with the anisotropic contribution due to $\chi^{(2)}$ response. The $\chi^{(3)}$ contribution might show resonance enhancement [60]. Here we observe FT intensity increase of transient reflectivity response along [011] with changing excitation photon energy. But that is most likely due to enhancement of the anisotropic part of the response at around 3.15 eV as shown by the FT amplitude response of the subtracted signal. The isotropic component thus does not show a strong resonant behavior for our range of photoexcitation energies.

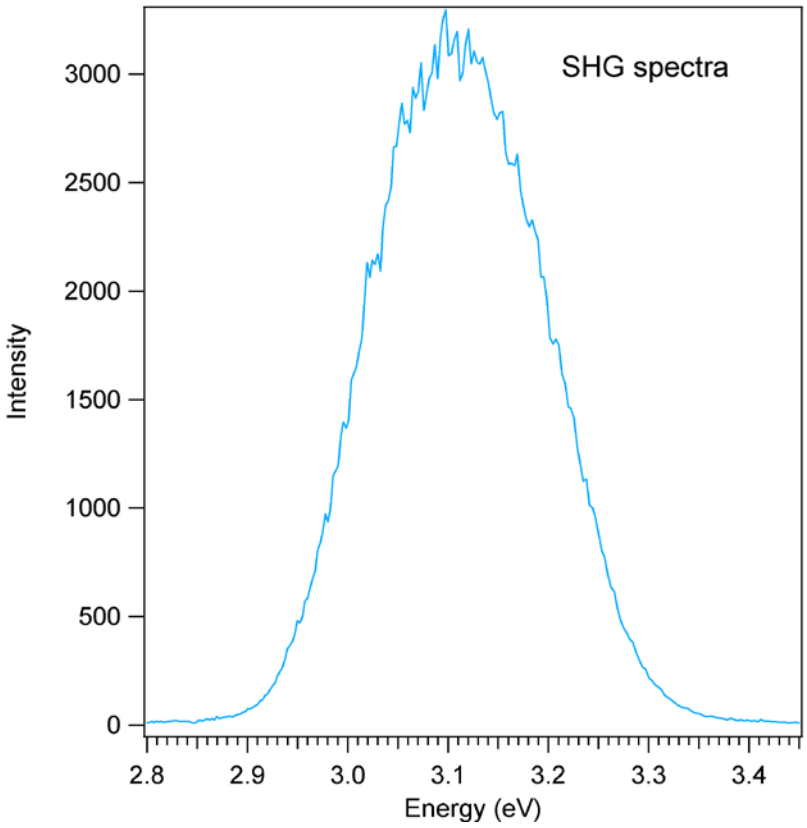

Figure 5.7 Spectrum of 400 nm laser light, which is used for the experiments.

Apart from the limitation in wavelength tunability, our optical pulse has a spectral bandwidth of 0.2 eV (Figure 5.7). Within the tunability range of our laser we are thus just changing the central wavelength position of our laser pulse. Due to the wide bandwidth of the exciting laser pulse we are not exciting the sample at different photon energies. Small second harmonic tunability between the critical point energies and wide bandwidth laser pulse are thus limiting factors in our case for performing experiments to explore resonant property of the response around the critical points. An experimental setup with more wavelength tuning capability and narrower spectral bandwidth will be suitable for the purpose of exploring the wavelength dependent or photon energy dependent response of GaAs.

6.0 SUMMARY AND CONCLUSIONS

Ultrafast spectroscopic techniques are used to study strongly nonequilibrium coherent phonon and plasmon dynamics in GaAs with photoexcited carrier densities in the range of ($10^{18}cm^{-3}$-$10^{20}cm^{-3}$). The importance of ultrafast spectroscopy is discussed in the context of probing different carrier relaxation processes. We considered various generation and detection processes of coherent phonon and plasmon modes and concluded depletion field screening mechanism as the dominating generation process of coherent phonons in GaAs. We also discussed different optical processes, which modulate the index of refraction in ultrafast spectroscopy, and can be identified through their different symmetry properties.

In Chapter 3 we discussed results of carrier density dependent experiments. These experiments were performed using the REOS technique. We analyzed the results by extracting the peak intensities from the FT spectra corresponding to the plasmon-phonon coupled L- mode and LO phonon mode. We also extracted decay times of the fast decaying coupled mode (L-) and the bare LO phonon oscillations. At lower ($2x10^{18}$ – $2x10^{19}$ cm^{-3}) photoexcited carrier density the LO phonon peak intensity is linearly increasing with carrier density consistent with carrier density dependent screening of the depletion layer electric field. The screening of the field results in a linear increase in the displacive force that excites the coherent phonon oscillation. But at relatively higher carrier densities ($3x10^{19}$ – $3x10^{20}$ cm^{-3}), the LO phonon peak intensity saturates, showing saturation of the screening. The carrier density dependent decay of the

coupled L- mode was also studied. The decay time decreases with increasing carrier density indicating carrier-carrier (specifically processes involving holes) scattering as the dominating decay process of plasma oscillation. There might be a population decay contribution to the overall decay as a result of transport of the photoexcited plasma to the bulk. With further increasing the carrier density the decay times saturate at a value of 0.4 ps. The decay time of the bare LO mode, which appears after decay of the plasmon coupled L- mode, is relatively longer and does not show any carrier density dependence. We also studied the change in frequency of the coupled plasmon-phonon mode with increasing carrier densities. The results are explained using a model of dielectric response with contributions from phonon and plasma oscillations with different types of carriers in the plasma. It was concluded that the dynamics is dominated by hole-phonon coupling as a result of faster drift and diffusion of lighter electrons into the bulk. This was further clarified by comparing the results of the 400 nm probe with 800 nm probe results. In case of 800 nm probe, both with 800 nm pump and 400 nm pump, we observe coupled mode frequencies in the range of 7.5-7.6 THz that is characteristic of phonon coupling with the Γ-valley electron plasma. The 800 nm light probes at a greater depth including contribution from hole-phonon coupling near surface as well as electron-phonon coupling at a larger depth. Therefore, the 800 nm probe experiments are mostly sensitive to the weakly damped plasma component, which exists at a larger depth of the sample.

In Chapter 4, we studied the symmetry dependent properties of generation and detection of coherent phonon and plasmon oscillations. We used linearly polarized light to pump the GaAs crystal with electric field aligned along different crystal directions. We observed changing pump polarization has negligible effect on the plasmon and phonon oscillation amplitudes, frequencies, phases, or the decay rates in the transient reflectivity signal. The absence of a pump polarization

dependence of the generation process shows again that the dominating mechanism for coherent phonon generation is the depletion layer electric field screening mechanism. Field screening depends only on the photoexcited carrier density, which only depends on the light intensity and not on its polarization.

The detection pulse polarization dependence was studied considering the symmetry properties of different non-linear optical processes contributing to the reflectivity signal. We observed strong anisotropic as well as weak isotropic contributions to the transient reflectivity signal. The variation of amplitudes of the oscillatory components along different crystal directions was explained considering the interference between these two reflectivity components. In addition to angle dependent amplitude variation, the oscillatory response also shows frequency and dephasing rate changes of the L- and bare LO phonon modes. These variations were also discussed considering the anisotropic coupling along different crystallographic directions. Symmetry dependent results obtained by using 400 nm pump/probe were compared with experimental results for 800 nm pump/probe and 800 nm pump/400 nm probe. It was concluded that the probe depth, determined by the probe color, is important in determining the frequency of the plasmon-phonon coupled mode (L-). The importance lies in the fact that 400 nm light probes only within a depth of 15 nm compared to ~55 nm for 800 nm light, though it excites the crystal up to a depth of 750 nm. In the initial few picoseconds due to differences in the carrier transport properties, 400 nm light probes high density hole plasma dynamics with high damping, whereas 800 nm probes a up to larger depth with a major contribution from low damped electron plasma as the carrier density does not change much within the observed depth.

Time dependent plasmon-phonon response was discussed in Chapter 5. The time dependent frequency evolution in first 2 ps is dominated by the changing plasma composition

and density. After 2 ps, the frequency approaches and remains at the bare LO phonon frequency of 8.7 THz. The coherent oscillation amplitude, when displayed in frequency-time space through time-windowed FT, shows dynamical features even after 2 ps for high density excitation. This was explained as a beating between two spatial components of coherent response representing different density regions of the plasma. Photon energy dependent reflectivity and FT intensity was also discussed. The FT peak heights do not show significant resonant behavior around E_1 and $E_1+\Delta_1$ critical points. The wide spectral bandwidth of the laser pulse used in the experiments and smaller wavelength tuning range are also limiting factors in resolving resonant effects in the coherent plasmon-phonon oscillations.

In conclusion, we have studied the coherent phonon and plasmon dynamics in GaAs at high carrier densities achieved through the L valley photoexcitation. We observed the carrier dynamics at various carrier densities and studied the symmetry properties of generation and detection of the coherent phonon and plasmon modes. Transient depletion field screening is the main generation process of coherent phonon. The detection symmetry shows contribution from optical processes, which are dominantly anisotropic, but also include a small isotropic contribution. The carrier-phonon dynamics are characteristic of the coupled plasmon-phonon mode dynamics representative of hole-phonon coupling in a high carrier density and high damping regimes.

In future this technique can be applied to study ultrafast optical processes in technologically important materials like carbon based materials (graphene, nano tubes etc [96]). Study on novel semiconductor structures also may reveal interesting properties with possible applications in new technologies [97]. The optical properties of semiconductor GaAs in highly non-equilibrium regime as described in this dissertation represent important fundamental

knowledge, which can be useful in designing new optical, photonic and opto-electronic devices and for new innovative technology for solving real world problems.

APPENDIX A

A.1 COHERENT PLASMON-PHONON RESPONSE IN VARIOUS OTHER SAMPLES

A.1.1 p-doped GaAs

The coherent phonon and plasmon response of the p-doped GaAs (n_d=1.2×$10^{18}$$cm^{-3}$) with increasing carrier density is shown in Figure A.1. The time dependent reflectivity response is quite similar to that of the n-doped result (Figure 3.1). The reflectivity response consists of three main features; (a) instantaneous electronic response near time zero, (b) strong coupled plasmon-phonon oscillation which decays in 1.5 ps time scale and (c) long lived LO phonon response at 8.75 THz. The corresponding FT spectra comprises of two main features. One is a peak at LO phonon frequency at around 8.75 THz for low photoexcitation density. A dip appears at higher carrier densities at the same frequency. The second one is a broad peak which appear between LO phonon frequency (8.75 THz) and the TO phonon frequency (8.0 THz). The broad peak red shifts with increasing carrier density and is attributed to the lower branch of the LO phonon-plasmon coupled mode (L-). This response is also similar to what has been observed for n-doped GaAs sample and has been discussed in detail in Chapter 3. The dip at LO phonon frequency which appears at high photoexcitation density is due to a Fano resonance

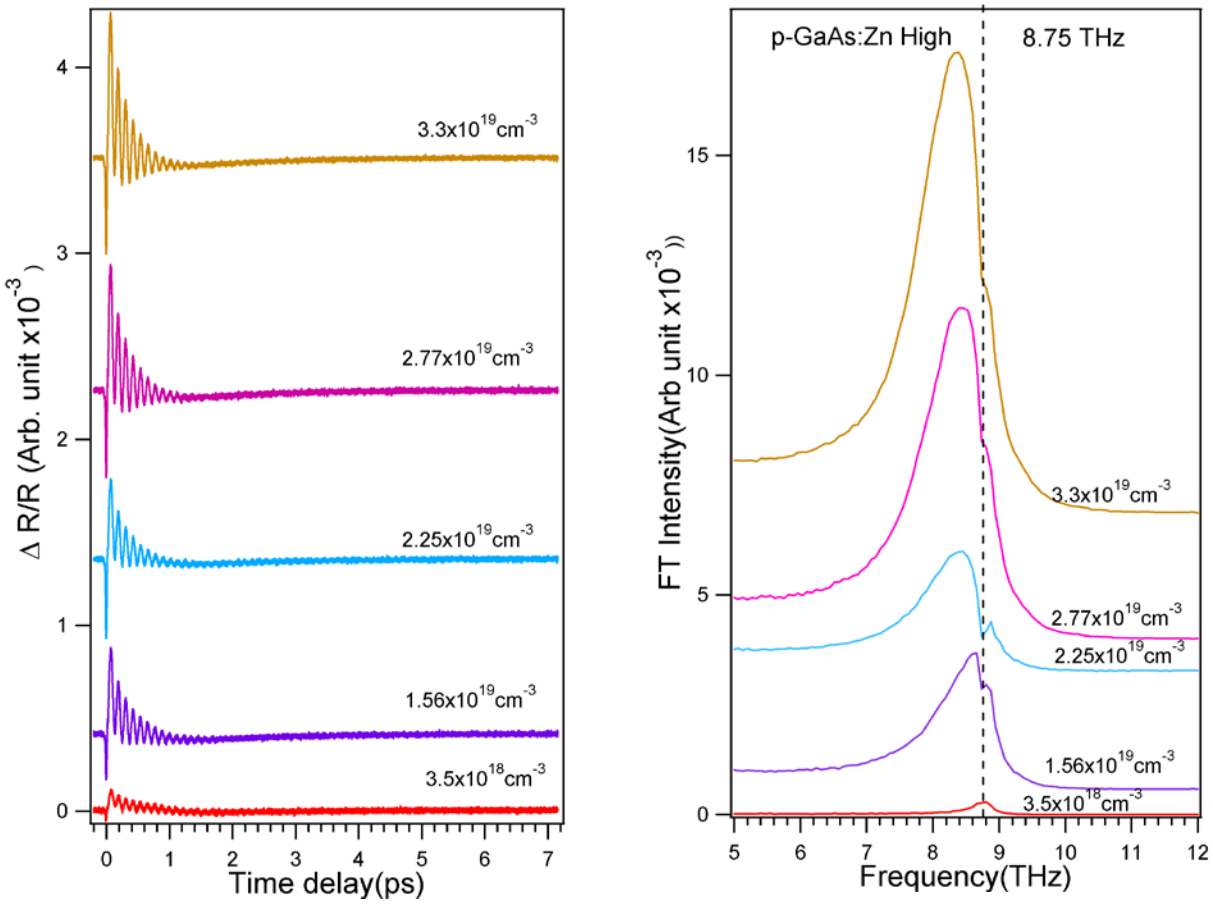

Figure A.1 Time dependent reflectivity and corresponding FT spectra are shown for p-doped GaAs with increasing photoexcited carried density. The estimated carrier density values are shown.

between the broad plasmon coupled (L-) response and a sharp LO phonon response. Even though the doping type is different, the similarities of the response of the p-doped and n-doped sample indicate that the high density photoexcited carriers dominate the dynamics.

A.1.2 Compensation doped GaAs

Carrier density dependent response of the compensation doped (undoped) GaAs sample is shown in figure A.2. The time dependent reflectivity shows a gradual decay of the oscillatory signal

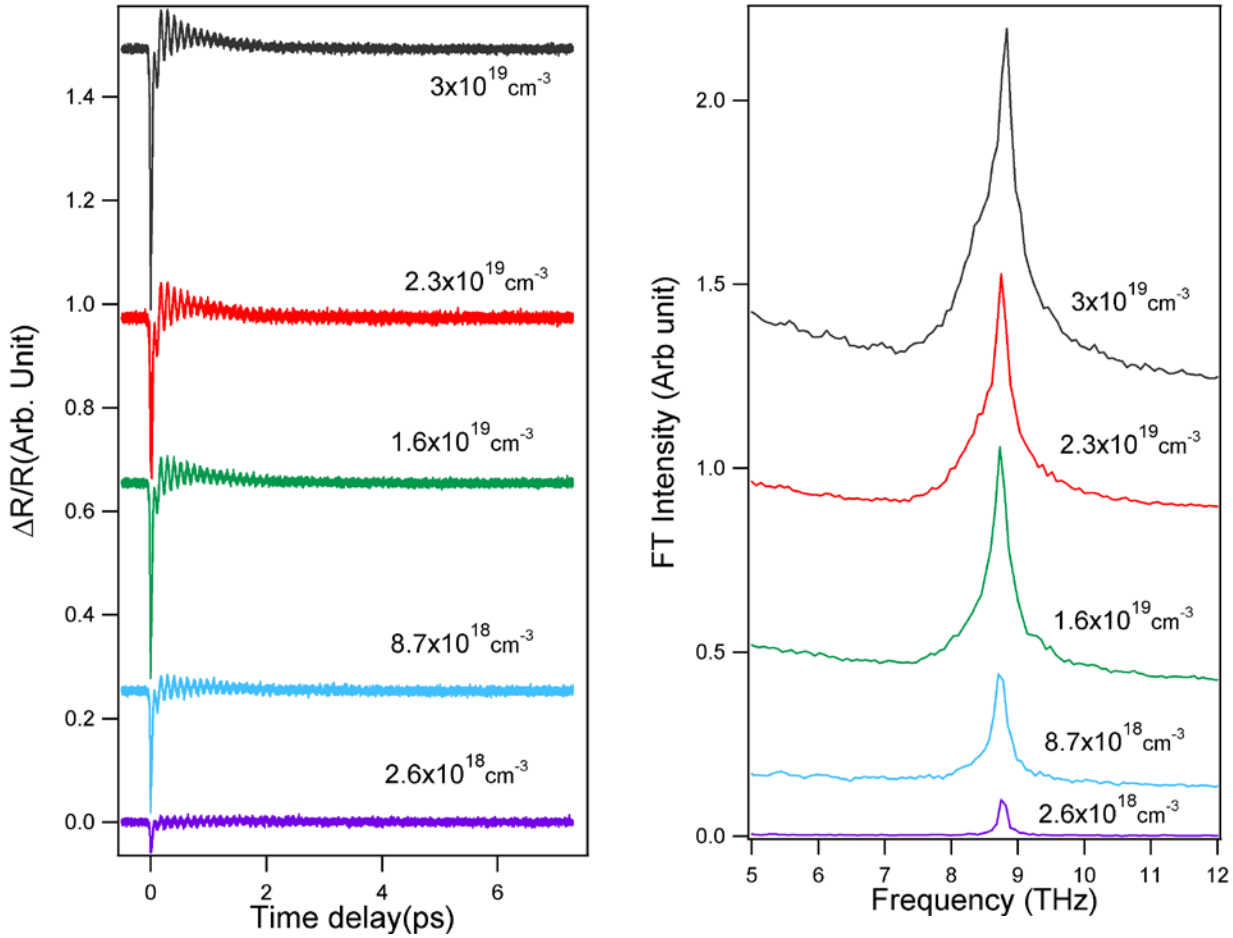

Figure A.2 Time dependent reflectivity and corresponding FT spectra are shown for undoped GaAs with increasing photoexcited carried density. The estimated carrier density values are shown.

over the whole time delay range after a strong electronic response near time zero. Only at high photoexcitation density the strong oscillatory component decays in a time delay of 1.5 ps and then there is a weak oscillatory component which slowly decays over longer time scales. This indicate the low density response is mainly a single mode behavior dominated by the LO phonon response. At high carrier density there is a small plasmon response which results in a weak plasmon-phonon coupled mode like behavior. This becomes further clear from the FT spectra. A single narrow peak at LO phonon frequency is the strongest feature of the spectra the height of which is linear with carrier density. At high density a very weak broad feature appears at frequencies between LO and TO phonon frequency limits which is attributed to the coupled plasmon-phonon mode. This is in contrary to the behavior that has been observed in n- and p-doped GaAs samples. This indicate doping dependent depletion layer formation near the surface of the sample and resultant instantaneous polarization of the photoexcited carriers in the depletion layer electric field is a major factor in the oscillation of photoexcited plasma.

BIBLIOGRAPHY

1. *International Technology Roadmap for Semiconductors*. 2009.

2. Nozik, A.J., *Quantum dot solar cells.* Physica E: Low-dimensional Systems and Nanostructures, 2002. **14**(1-2): p. 115-120.

3. Ellingson, R.J., et al., *Highly Efficient Multiple Exciton Generation in Colloidal PbSe and PbS Quantum Dots.* Nano Letters, 2005. **5**(5): p. 865-871.

4. Schaller, R.D., V.M. Agranovich, and V.I. Klimov, *High-efficiency carrier multiplication through direct photogeneration of multi-excitons via virtual single-exciton states.* Nat Phys, 2005. **1**(3): p. 189-194.

5. Hase, M., *Ultrafast dynamics of plasmon-phonon coupling: Estimation of electron mobility in GaAs.* physica status solidi (c), 2008. **5**(1): p. 364-366.

6. Hu, B.B., et al., *Identifying the Distinct Phases of Carrier Transport in Semiconductors with 10 fs Resolution.* Physical Review Letters, 1995. **74**(9): p. 1689.

7. Leitenstorfer, A., et al., *Ultrafast high-field transport in semiconductors.* Physica B: Condensed Matter, 1999. **272**(1-4): p. 348-352.

8. Hase, M., et al., *The birth of a quasiparticle in silicon observed in time-frequency space.* Nature, 2003. **426**(6962): p. 51-54.

9. Fürst, C., et al., *Quantum Kinetic Electron-Phonon Interaction in GaAs: Energy Nonconserving Scattering Events and Memory Effects.* Physical Review Letters, 1997. **78**: p. 3733–3736.

10. Chemla, D.S. and J. Shah, *Many-body and correlation effects in semiconductors.* Nature, 2001. **411**(6837): p. 549-557.

11. Huber, R., et al., *How many-particle interactions develop after ultrafast excitation of an electron-hole plasma.* Nature, 2001. **414**: p. 286-289.

12. Li, X., et al., *Many-Body Interactions in Semiconductors Probed by Optical Two-Dimensional Fourier Transform Spectroscopy.* Physical Review Letters, 2006. **96**(5): p. 057406.

13. Vallée, F., F. Ganikhanov, and F. Bogani, *Dephasing of LO-phonon-plasmon hybrid modes in n-type GaAs.* Physical Review B, 1997. **56**(20): p. 13141.

14. Schawlow, A.L. and C.H. Townes, *Infrared and Optical Masers.* Physical Review, 1958. **112**(6): p. 1940.

15. Maiman, T.H., *Stimulated Optical Radiation in Ruby.* Nature, 1960. **187**(4736): p. 493-494.

16. Maiman, T.H., *Optical and Microwave-Optical Experiments in Ruby.* Physical Review Letters, 1960. **4**(11): p. 564.

17. Mocker, H.W. and R.J. Collins, *Mode Competition and Self-locking Effects in a Q-switched Ruby Laser.* Applied Physics Letters, 1965. **7**(10): p. 270-273.

18. DeMaria, A.J., C.M. Ferrar, and J.G.E. Danielson, *MODE LOCKING OF A Nd^{3+}-DOPED GLASS LASER.* Applied Physics Letters, 1966. **8**(1): p. 22-24.

19. Ippen, E.P., C.V. Shank, and A. Dienes, *Passive mode locking of the cw dye laser.* Applied Physics Letters, 1972. **21**(8): p. 348-350.

20. Shank, C.V. and E.P. Ippen, *Subpicosecond kilowatt pulses from a mode-locked cw dye laser.* Applied Physics Letters, 1974. **24**(8): p. 373-375.

21. Fork, R.L., B.I. Greene, and C.V. Shank, *Generation of optical pulses shorter than 0.1 psec by colliding pulse mode locking.* Applied Physics Letters, 1981. **38**(9): p. 671-672.

22. Lautenschlager, P., et al., *Interband critical points of GaAs and their temperature dependence.* Physical Review B, 1987. **35**(17): p. 9174.

23. Cardona, M. and G. Harbeke, *Absorption Spectrum of Germanium and Zinc-Blende-Type Materials at Energies Higher than the Fundamental Absorption Edge.* Journal of Applied Physics, 1963. **34**(4): p. 813-818.

24. Kim, D.-s. and P.Y. Yu, *Hot-electron relaxations and hot phonons in GaAs studied by subpicosecond Raman scattering.* Physical Review B, 1991. **43**(5): p. 4158.

25. Webb, M.D., S.T. Cundiff, and D.G. Steel, *Observation of time-resolved picosecond stimulated photon echoes and free polarization decay in GaAs/AlGaAs multiple quantum wells.* Physical Review Letters, 1991. **66**(7): p. 934.

26. Elsaesser, T., et al., *Initial thermalization of photoexcited carriers in GaAs studied by femtosecond luminescence spectroscopy.* Physical Review Letters, 1991. **66**(13): p. 1757.

27. Chang, Y.M., L. Xu, and H.W.K. Tom, *Observation of Coherent Surface Optical Phonon Oscillations by Time-Resolved Surface Second-Harmonic Generation.* Physical Review Letters, 1997. **78**(24): p. 4649.

28. Gaal, P., et al., *Internal motions of a quasiparticle governing its ultrafast nonlinear response.* Nature, 2007. **450**(7173): p. 1210-1213.

29. Shah, J., et al., *Determination of intervalley scattering rates in GaAs by subpicosecond luminescence spectroscopy.* Physical Review Letters, 1987. **59**(19): p. 2222.

30. Othonos, A., *Probing ultrafast carrier and phonon dynamics in semiconductors.* Journal of Applied Physics, 1998. **83**(4): p. 1789-1830.

31. Rota, L., et al., *Ultrafast thermalization of photoexcited carriers in polar semiconductors.* Physical Review B, 1993. **47**(8): p. 4226.

32. Langot, P., R. Tommasi, and F. Vallée, *Nonequilibrium hole relaxation dynamics in an intrinsic semiconductor.* Physical Review B, 1996. **54**(3): p. 1775.

33. Vallée, F., *Time-resolved investigation of coherent LO-phonon relaxation in III-V semiconductors.* Physical Review B, 1994. **49**(4): p. 2460.

34. Shah, J., *Ultrafast Spectroscopy of Semiconductors and Semiconductor Nanostructures.* First ed. Springer Series in Solid-State Sciences. Vol. 115. 1996, Heidelberg: Springer.

35. Cho, G.C., W. Kütt, and H. Kurz, *Subpicosecond time-resolved coherent-phonon oscillations in GaAs.* Phys. Rev. Lett., 1990. **65**(6): p. 764.

36. Kash, J.A., J.C. Tsang, and J.M. Hvam, *Subpicosecond Time-Resolved Raman Spectroscopy of LO Phonons in GaAs.* Physical Review Letters, 1985. **54**: p. 2151–2154.

37. Oberli, D.Y., et al., *Time-resolved Raman scattering in GaAs quantum wells.* Physical Review Letters, 1987. **59**(6): p. 696.

38. Weiner, A.M., S.D. Silvestri, and E.P. Ippen, *Three-pulse scattering for femtosecond dephasing studies: theory and experiment.* J. Opt. Soc. Am. B, 1985. **2**(4): p. 654-662.

39. Bakker, H.J., et al., *Time-resolved study of dephasing mechanisms of excitons in GaAs/$Al_xGa_{1-x}As$ quantum-well structures.* Physical Review B, 1994. **49**(12): p. 8249.

40. Johnson, M.B., T.C. McGill, and A.T. Hunter, *Picosecond time-resolved photoluminescence using picosecond excitation correlation spectroscopy.* Journal of Applied Physics, 1988. **63**(6): p. 2077-2082.

41. Zhang, X.C., et al., *Generation of femtosecond electromagnetic pulses from semiconductor surfaces.* Applied Physics Letters, 1990. **56**(11): p. 1011-1013.

42. Hu, B.B., et al., *Optically steerable photoconducting antennas.* Applied Physics Letters, 1990. **56**(10): p. 886-888.

43. Kersting, R., et al., *Few-Cycle THz Emission from Cold Plasma Oscillations.* Physical Review Letters, 1997. **79**(16): p. 3038.

44. Leitenstorfer, A., et al., *Femtosecond high-field transport in compound semiconductors.* Physical Review B, 2000. **61**(24): p. 16642.

45. Leitenstorfer, A., et al., *Femtosecond Charge Transport in Polar Semiconductors.* Physical Review Letters, 1999. **82**(25): p. 5140.

46. Kuznetsov, A.V. and C.J. Stanton, *Theory of Coherent Phonon Oscillations in Bulk GaAs*, in *Ultrafast Phenomena in Semiconductors*, K.T.Tsen, Editor. 2001: New York.

47. Bron, W.E., J. Kuhl, and B.K. Rhee, *Picosecond-laser-induced transient dynamics of phonons in GaP and ZnSe.* Physical Review B, 1986. **34**(10): p. 6961.

48. Dekorsy, T., G.C. Cho, and H. Kurz, *Coherent Phonons in Condesed Media*, in *Light Scattering in Solids VIII*, M. Cardona and G. Guentherodt, Editors. 2000, Springer-Verlag: Berlin.

49. Laubereau, A. and W. Kaiser, *Vibrational dynamics of liquids and solids investigated by picosecond light pulses.* Reviews of Modern Physics, 1978. **50**(3): p. 607.

50. Yan, Y.-X., J.E.B. Gamble, and K.A. Nelson, *Impulsive stimulated scattering: General importance in femtosecond laser pulse interactions with matter, and spectroscopic applications.* The Journal of Chemical Physics, 1985. **83**(11): p. 5391-5399.

51. Merlin, R., *Generating coherent THz phonons with light pulses.* Solid State Communications, 1997. **102**(2-3): p. 207-220.

52. Zeiger, H.J., et al., *Theory for displacive excitation of coherent phonons.* Physical Review B, 1992. **45**(2): p. 768.

53. Cheng, T.K., et al., *Mechanism for displacive excitation of coherent phonons in Sb, Bi, Te, and Ti_2O_3.* Applied Physics Letters, 1991. **59**(16): p. 1923-1925.

54. Foerst, M. and T. Dekorsy, *Coherent Phonon in Bulk and Low Dimensional Semiconductors*, in *Coherent Vibrational Dynamics, Practical Spectroscopy*, G.C.a.G.L. S. DeSilvestri, Editor. 2007, CRC: Boca Raton. p. 129-172.

55. Vorlicek, V., et al., *Raman scattering by the coupled plasmon-LO-phonon modes near the $E_0+\Delta_0$ gap of n-type GaAs: Resonance and interference effects.* Physical Review B, 1990. **42**(9): p. 5802.

56. Pfeifer, T., et al., *Generation Mechanisms for Coherent LO Phonons in Surface Space Charge Fields of III-V-Compounds* Applied Physics A, 1992. **55**: p. 482-488.

57. Darling, R.B., *Defect-state occupation, Fermi-level pinning, and illumination effects on free semiconductor surfaces.* Physical Review B, 1991. **43**(5): p. 4071.

58. Sze, S.M. and K.K. Ng, *Physics of Semiconductor Devices.* 3 ed. 2007: Wiley-Interscience.

59. Kuznetsov, A.V. and C.J. Stanton, *Coherent phonon oscillations in GaAs.* Physical Review B, 1995. **51**: p. 7555–7565.

60. Cho, G.C., et al., *Time-resolved observation of coherent phonons by the Franz-Keldysh effect.* Phys. Rev. B, 1996. **53**: p. 6904–6907.

61. Yu, P.Y. and M. Cardona, *Fundamentals of Semiconductors*. 2003, Berlin: Springer.

62. Dekorsy, T., et al., *Emission of Submillimeter Electromagnetic Waves by Coherent Phonons.* Physical Review Letters, 1995. **74**(5): p. 738.

63. Aspnes, D.E. and A.A. Studna, *Schottky-Barrier Electroreflectance: Application to GaAs.* Physical Review B, 1973. **7**(10): p. 4605.

64. Shen, Y.R., *The Principles of Nonlinear Optics*. 2003: Wiley-Interscience.

65. Menéndez, J. and M. Cardona, *Interference effects: A key to understanding forbidden Raman scattering by LO phonons in GaAs.* Physical Review B, 1985. **31**(6): p. 3696.

66. Yariv, A. and P. Yeh, *Photonics*. 2007: Oxford University Press.

67. Aspnes, D.E. and A.A. Studna, *Dielectric functions and optical parameters of Si, Ge, GaP, GaAs, GaSb, InP, InAs, and InSb from 1.5 to 6.0 eV.* Physical Review B, 1983. **27**(2): p. 985.

68. Dekorsy, T., et al., *Subpicosecond carrier transport in GaAs surface-space-charge fields.* Physical Review B, 1993. **47**(7): p. 3842.

69. Ishioka, K., M. Kitajima, and K. Ushida, *Power- and Polarization-Dependences of Coherent Phonons of Tetrahedrally Bonded Semiconductors.* Journal of the Physical Society of Japan, 2006. **75**(8): p. 084704.

70. Hase, M., et al., *Ultrafast decay of coherent plasmon-phonon coupled modes in highly doped GaAs.* Physical Review B, 1999. **60**(24): p. 16526.

71. Rodrigues-Herzog, R., et al., *Ultrafast energy loss of electrons in p-GaAs.* Applied Physics Letters, 1995. **67**(2): p. 264-266.

72. Nintunze, N. and M.A. Osman, *Ultrafast relaxation of highly photoexcited carriers in p-type and intrinsic GaAs.* Physical Review B, 1994. **50**(15): p. 10706.

73. Cho, G.C., et al., *Generation and Relaxation of Coherent Majority Plasmons.* Physical Review Letters, 1996. **77**(19): p. 4062.

74. Chang, Y.M., *Interaction of electron and hole plasma with coherent longitudinal optical phonons in GaAs.* Appl. Phys. Lett., 2002. **80**(14): p. 2487-2489.

75. Sjodin, T., H. Petek, and H.L. Dai, *Ultrafast carrier dynamics in silicon: A two-color transient reflection grating study on a (111) surface.* Phys. Rev. Lett., 1998. **81**: p. 5664-5667.

76. Ridley, B.K., *Quantum Processes in Semiconductor*. 1999, Oxford: Clarendon Press.

77. Kuzmany, H., *Solid-State Spectroscopy*. 1998: Springer.

78. Fukasawa, R. and S. Perkowitz, *Raman-scattering spectra of coupled LO-phonon-hole-plasmon modes in p-type GaAs.* Physical Review B, 1994. **50**(19): p. 14119.

79. Mooradian, A. and A.L. McWhorter, *Polarization and Intensity of Raman Scattering from Plasmons and Phonons in Gallium Arsenide.* Physical Review Letters, 1967. **19**(15): p. 849.

80. Irmer, G., M. Wenzel, and J. Monecke, *Light scattering by a multicomponent plasma coupled with longitudinal-optical phonons: Raman spectra of p-type GaAs:Zn.* Physical Review B, 1997. **56**(15): p. 9524.

81. Bailey, D.W., C.J. Stanton, and K. Hess, *Numerical studies of femtosecond carrier dynamics in GaAs.* Physical Review B, 1990. **42**(6): p. 3423.

82. Wan, K. and J.F. Young, *Interaction of longitudinal-optic phonons with free holes as evidenced in Raman spectra from Be-doped p-type GaAs.* Physical Review B, 1990. **41**(15): p. 10772.

83. Hase, M., et al., *Dynamics of coherent plasmon-phonon coupled modes in GaAs using ultrashort laser pulse.* Journal of Luminescence, 1998. **76&77**: p. 68-71.

84. Irmer, G., M. Wenzel, and J. Monecke, *Light scattering by a multicomponent plasma coupled with longitudinal-optical phonons: Raman spectra of p-type GaAs:Zn.* Phys. Rev. B, 1997. **56**(15): p. 9524.

85. Menéndez, J. and M. Cardona, *Interference between Allowed and Forbidden Raman Scattering by Longitudinal-Optical Phonons in GaAs.* Physical Review Letters, 1983. **51**(14): p. 1297.

86. Yee, K.J., et al., *Coherent Optical Phonon Oscillations in Bulk GaN Excited by Far below the Band Gap Photons.* Physical Review Letters, 2002. **88**(10): p. 105501.

87. Kersting, R., et al., *Coherent plasmons in n-doped GaAs.* Physical Review B, 1998. **58**(8): p. 4553.

88. Kauschke, W., N. Mestres, and M. Cardona, *Resonant Raman scattering by plasmons and LO phonons near the E_1 and $E_1+\Delta_1$ gaps of GaSb.* Phys. Rev. B, 1987. **36**(14): p. 7469.

89. Kuett, W., W. Albrecht, and H. Kurz, *Generation of coherent phonons in Condesned Media.* IEEE J. of Quant. Elect., 1992. **28**(10): p. 2434-2444.

90. Averbukh, I.S. and N.F. Perelman, *Fractional revivals: Universality in the long-term evolution of quantum wave packets beyond the correspondence principle dynamics.* Physics Letters A, 1989. **139**(9): p. 449-453.

91. Yeazell, J.A., M. Mallalieu, and C.R. Stroud, *Observation of the collapse and revival of a Rydberg electronic wave packet.* Physical Review Letters, 1990. **64**(17): p. 2007.

92. Misochko, O.V., et al., *Observation of an Amplitude Collapse and Revival of Chirped Coherent Phonons in Bismuth.* Physical Review Letters, 2004. **92**(19): p. 197401.

93. Diakhate, M., E. Zijlstra, and M. Garcia, *Quantum dynamical study of the amplitude collapse and revival of coherent A1g phonons in bismuth: a classical phenomenon?* Applied Physics A: Materials Science & Processing, 2009. **96**(1): p. 5-10.

94. Aspnes, D.E. and A.A. Studna, *High resolution electroreflectance measurements of GaAs.* Surface Science, 1973. **37**: p. 631-638.

95. Kuball, M., et al., *Electric-field-induced Raman scattering in GaAs: Franz-Keldysh oscillations.* Physical Review B, 1995. **51**(11): p. 7353.

96. Ishioka, K., et al., *Ultrafast electron-phonon decoupling in graphite.* Physical Review B, 2008. **77**(12): p. 121402.

97. Fluegel, B., et al., *Plasmonic all-optical tunable wavelength shifter.* Nat Photon, 2007. **1**(12): p. 701-703.